الجمهورية الجزائرية الديمقراطية الشعبية

République Algérienne Démocratique et Populaire

Ministère de L'Enseignement Supérieur et de la Recherche Scientifique

Université Ferhat ABBAS Sétif 1

UNIVERSITÉ FERHAT ABBAS - SETIF 1

FACULTÉ DE TECHNOLOGIE

THESE

Présentée au Département de D'ELECTROTECHNIQUE

Pour l'obtention du diplôme de

DOCTORAT EN SCIENCES

Option: Commande Electrique

Par

Rafik DEMBRI

THÈME

Etude et implémentation d'une commande non conventionnelle pour une machine asynchrone à double alimentation en vue d'une utilisation dans la production d'énergie éolienne.

Soutenue le 12/02/2025 devant le Jury:

RADJEAI Hammoud	**Professeur**	**Univ. Ferhat Abbas Sétif 1**	**Président**
RAHMANI Lazhar	**Professeur**	**Univ. Ferhat Abbas Sétif 1**	**Directeur de these**
BOUKHETALA Djamel	**Professeur**	**ENP, Alger**	**Examinateur**
BETKA Achour	**Professeur**	**Univ. Biskra**	**Examinateur**
LABAR Hocine	**Professeur**	**Univ. Badji Mokhtar Annaba**	**Examinateur**
KESSAL Abdelhalim	**Professeur**	**Univ. Bordj Bou Arréridj**	**Examinateur**

Study and implementation of a non-conventional control of the doubly-fed induction machine for wind energy production.

By

RAFIK DEMBRI

A dissertation

presented to FERHAT Abbas – Sétif 1 University

in partial fulfillment of the

requirements for the degree of doctor of science

in the Program of electrical control

University of Sétif 1, Algeria, 2025

Acknowledgements

I would like to extend my sincere thanks to my supervisor, Professor. **RAHMANI Lazhar**, for their invaluable guidance, encouragement, and insightful feedback throughout this journey. Their expertise and unwavering support have been instrumental in shaping this research.

My heartfelt appreciation goes to my family especially my parents. To my wife, for her endless love, understanding, and sacrifices; you have been my pillar of strength, always there to encourage me in moments of doubt. To my children, whose smiles and laughter brought joy and light to even the most challenging days, thank you for your patience and love.

I would also like to thank my colleagues and friends who provided moral support, insightful discussions, and sometimes much-needed distractions. Your companionship has made this journey less daunting and more fulfilling.

A special thanks to the faculty members and administrative staff of **University of Sétif 1** for their assistance and encouragement during my time here. I am particularly grateful to **Department of Electrical Engineering** for providing me with the resources and support necessary to carry out my research.

Finally, I want to acknowledge everyone whose work and contributions have inspired and guided me throughout this project. Your dedication to advancing knowledge has been a constant source of motivation.

Thank you all.

Abbreviation

Abbreviation	***Meaning***
ABC	Three-Phase Reference Frame
AC	Alternating Current
αβ	Alpha-Beta Reference Frame
DC	Direct Current
DFIG	Doubly-Fed Induction Generator
DQ	Direct-Quadrature Reference Frame
DSP	Digital Signal Processor
DTC	Direct Torque Control
EKF	Extended Kalman Filter
FLC	Fuzzy Logic Control
FOC	Field-Oriented Control
FO Fuzzy PD+I	Fractional-Order Fuzzy PD+I Controller
FOPD	Fractional-Order Proportional-Derivative
FOPI	Fractional-Order Proportional-Integral
FOPID	Fractional-Order Proportional-Integral-Derivative
GA	Genetic Algorithm
GSC	Grid-Side Converter
HAWT	Horizontal Axis Wind Turbine
IAE	Integral Absolute Error
IGBT	Insulated-Gate Bipolar Transistor
ISE	Integral Squared Error
ITAE	Integral Time Absolute Error
ITSE	Integral Time Squared Error
LMI	Linear Matrix Inequality
LQR	Linear Quadratic Regulator
LQG	Linear Quadratic Gaussian
MPPT	Maximum Power Point Tracking
NN	Neural Network
PI	Proportional-Integral (Controller)
PID	Proportional-Integral-Derivative (Controller)
PLL	Phase-Locked Loop
PMSG	Permanent Magnet Synchronous Generator
PSO	Particle Swarm Optimization
PWM	Pulse Width Modulation
RMS	Root Mean Square
RSC	Rotor-Side Converter
SCIG	Squirrel-Cage Induction Generator
SMC	Sliding Mode Control
SOC	State of Charge
SSO	Social Spider Optimizer
SVM	Space Vector Modulation
THD	Total Harmonic Distortion
VAWT	Vertical Axis Wind Turbine
WRSG	Wound Rotor Synchronous Generator
WTS	Wind Turbine System

Bibliography

List of Figures

List of Tables

General introduction

Wind energy is developing at an increasing pace due to the significant power output of wind turbines and substantial financial incentives from countries aiming to combat climate change. From a financial perspective, integrating wind turbines with other energy systems requires improving their efficiency, which involves reducing operation and maintenance costs and increasing the power fed into the grid. In recent years, this energy sector has seen rapid advancements both technically and economically[1].

Renewable energies are an economically viable solution for providing energy services, especially to isolated rural populations. Currently, many countries are firmly committed to wind energy. Over the past decade, the global wind energy production capacity has experienced rapid growth, estimated at 28% annually[2].

Wind turbines can operate at either fixed or variable speeds, as in the case of the doubly-fed induction generator (DFIG). The DFIG receives mechanical energy and converts it into electrical energy, which is transmitted to the power grid in a variable-speed mode. Due to access to both the stator and the rotor, the DFIG has become an attractive solution, offering multiple degrees of freedom. This has led to extensive research on various aspects of its design, modeling, analysis, and control. Our work focuses on the generator mode, particularly on the modeling and implementation of robust control systems. Although the DFIG offers several advantages in terms of efficiency and high power output, its operation remains complex due to the numerous phenomena and variables involved in the machine's integration system[3].

The DFIG can operate in either motor or generator mode. The difference from a squirrel-cage induction machine lies in the fact that, for the DFIG, it is no longer the rotational speed that determines the motor or generator mode of operation, hence its name as a generalized machine. Indeed, a squirrel-cage machine must rotate below its synchronous speed to operate in motor mode and above this speed to operate in generator mode. However, in the case of the DFIG, it is the control of the rotor voltages that allows the management of the magnetic field inside the machine, thus enabling operation in either super-synchronous or sub-synchronous mode[4].

Integrating the DFIG into the grid requires specific considerations regarding power supply. Generally, the most commonly used topology involves connecting the stator directly to the grid, while the rotor is controlled by power electronic equipment that only converts a fraction (approximately 30%) of the total system power[5], [6]. This power electronic equipment typically consists of two bidirectional converters: the machine-side converter and the grid-side converter. This topology makes the DFIG more advantageous, especially for higher power levels, as it allows for the sharing of magnetizing current between the two windings and the power exchanged with the grid. In terms of control, unlike a squirrel-cage machine, measuring currents at the stator and rotor provides greater flexibility and better accuracy for controlling flux and electromagnetic torque[7].

Like the squirrel-cage induction machine, the DFIG is fundamentally a nonlinear system due to the coupling between flux and electromagnetic torque. Therefore, vector control by flux orientation along a preferred axis ensures decoupling between the two axes of flux and electromagnetic torque, thus decoupling active and reactive powers. However, the models used are approximate and have variable parameters depending on the system's state and operating point. The variation in electrical and mechanical parameters degrades the performance of control laws and can, in some cases, lead to unstable operation[8], [9].

The most sophisticated control techniques for the DFIG are based on stator flux orientation. Considering the two-phase model of the DFIG using a rotating reference frame, aligning the d-axis with the stator flux automatically aligns the components of active and reactive currents along the d and q axes, respectively[10]. The reference rotor currents along the two axes are derived from the imposed reference active and reactive powers. Consequently, power decoupling can be achieved through proportional-integral (PI) type regulators[11].

Similar to the flux orientation strategy for the DFIG, we can use voltage orientation to control the grid-side converter. In this approach, aligning the grid voltage along the two axes, d and q, allows us to decouple active and reactive powers, thus controlling the power factor and voltage regulation of the DC link. However, accurately determining the angle of the flux (or voltage) is essential for this method. Nonetheless, the main challenge lies

in determining the correct phase sequence and simultaneously establishing the accurate angle value (with precision) to perform the trigonometric rotations[12].

To effectively control the DFIG, it is necessary to simultaneously know two angles: the position of the rotating magnetic field (θ_s) and the physical position of the DFIG rotor (θ_r). Typically, the mechanical angle of the rotor can be directly determined using an encoder or indirectly without the need for a speed sensor. However, the electrical angle of the rotating magnetic field can be calculated indirectly from the stator voltage[13].

Indeed, for large machines where the stator resistance value can be neglected, the flux components along the two axes, d and q, become perpendicular to the respective d and q components of voltages. Consequently, the angle of the stator flux can be calculated through the stator voltages of the machine instead of directly calculating the fluxes. Generally, a Phase-Locked Loop (PLL) is used to identify the electrical angle of the rotating field[14].

The general objective of this thesis is to develop and implement a novel control strategy for doubly fed induction generator (DFIG)-based wind turbine systems (WTS) using a fractional-order fuzzy PD+I (FO Fuzzy PD+I) regulator optimized by the social spider optimizer (SSO). This approach marks a significant advancement in DFIG control compared to existing methods that rely on traditional PI regulators. The proposed FO Fuzzy PD+I regulator leverages the combined strengths of fuzzy logic and fractional-order control, resulting in superior performance and robustness in DFIG.

This research represents a significant contribution to the field of DFIG control, offering a more effective and robust solution for wind turbine operation, ultimately leading to improved power quality and grid integration capabilities.

This thesis is divided into five chapters followed by appendices allowing to follow the approach pursued throughout the work.

In the opening chapter, we will provide a comprehensive overview of various methods for wind power production. This will enable us to establish our position regarding the selection of generator type and technology employed in wind turbines. Consequently, we will explore the advantages of the Doubly Fed Induction Generator in comparison to other utilized machines.

In the second chapter, we focus on modeling the mechanical components of the wind turbine. This involves considering the aerodynamic properties of the blades and implementing continuous control over their pitch angle. The aim is to optimize turbine efficiency to extract maximum power from the wind. Through this approach, the turbine maintains peak torque output by dynamically adapting to varying wind conditions . Additionally, we detail the modeling of the speed multiplier connecting the turbine to the generator. Finally, we present an integrated model of the entire mechanical system, laying the groundwork for subsequent wind turbine simulations.

Chapter 3 is dedicated to the study of the converter. Here, the focus is mainly on the converter operating in bidirectional alternating/current/direct (AC/DC/AC) mode.

Chapter 4 deals with the modeling and vector control of the DFIG, specifically focusing on stator flux orientation. This technique is well-known in the literature, particularly for its dependency on system parameters. However, it will serve as a tool for familiarization with DFIG control.

Chapter 5 demonstrates and models a novel control strategy for the DFIG using a fractional-order fuzzy PD+I regulator optimized by the Social Spider Optimizer (SSO) algorithm.

In each chapter, when necessary, the obtained results are presented and analyzed. Additionally, any encountered problems and possible solutions are discussed.

1 State of the Art of wind energy

1.1 Introduction

The world is witnessing a dramatic shift towards renewable energy sources, driven by a growing urgency to address climate change and environmental pollution. This surge is not just rhetoric; global wind energy capacity alone has grown nearly five-fold in the past decade, jumping from around 181 GW (gigawatts) in 2010 to over 837 GW by 2021[2]. Experts predict this trend will continue, with renewables playing a dominant role in sustainable energy systems within the next 30 years.

This transition is fueled by the inherent advantages of renewable energy. Unlike fossil fuels and nuclear power, renewables like solar, wind, and geothermal energy are constantly replenished by natural forces, making them a sustainable long-term solution. They also don't emit greenhouse gases during operation, significantly reducing their contribution to global warming. The International Panel on Climate Change (IPCC) even highlights renewable energy as a key weapon in our fight against climate change[2].

On the other hand, traditional energy sources come with significant drawbacks. The production and consumption of fossil fuels are major contributors to air and water pollution, with the World Health Organization estimating 7 million deaths annually from air pollution alone caused by fossil fuels[17]. Nuclear power, while avoiding greenhouse gas emissions, raises concerns about long-term radioactive waste disposal and the potential for catastrophic accidents[17].

As we move forward, embracing renewable energy offers a compelling path towards a cleaner, healthier, and more sustainable future for generations to come. This introduction sets the stage for a deeper exploration of renewable energy, its benefits, and the challenges of transitioning to a more sustainable energy mix.

1.2 Current situation of wind energy

The wind, bearer of clean and renewable energy in the form of wind energy, asserts itself as a rising force, ready to tackle the challenges of climate change and energy security.

Global wind capacity has experienced exponential growth in recent years, reaching 743 GW in 2022 (figure 1), with an increase of over 11% compared to the previous year[15]. China leads the market with 254 GW of installed capacity, followed by the United States with 114 GW. Europe ranks third with 169 GW of installed capacity, while cumulative wind capacity in Africa reached 6.2 GW, representing a 23% increase from 2021[15]. Wind energy is emerging as a major source of renewable energy, contributing to the reduction of greenhouse gas emissions and the fight against climate change[17]. In 2022, it generated 2,762 TWh of electricity, approximately 6% of global electricity production[2].

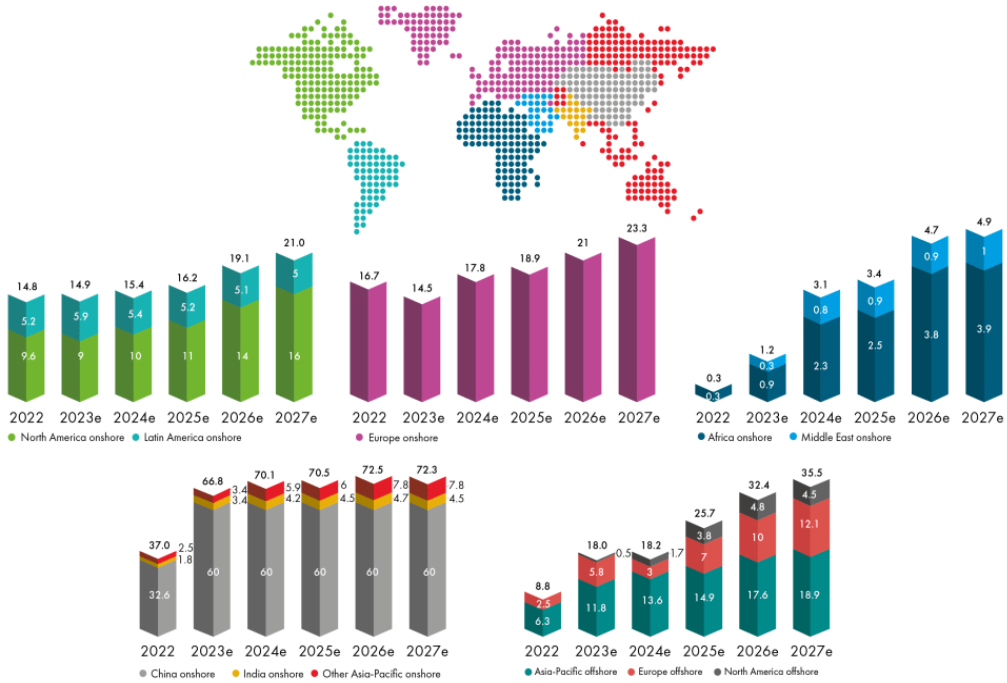

Figure 1-1: Cumulative installed wind power capacity worldwide

Technological innovation is propelling the wind industry to new heights, particularly in offshore wind, with increasingly powerful turbines being installed in deep waters.

In 2022, the global offshore wind power capacity reached a total of 64.3 gigawatts (GW). China contributed 49% of this capacity, followed by the United Kingdom with 22% and Germany with 13%, collectively representing over 75% of the world's offshore wind installations. Despite this rapid expansion, wind energy development continues to face several challenges.[2]

Environmental concerns and production intermittency require special attention. Innovative solutions and better integration into the electrical grid are essential to maximize the benefits of this promising energy source[1].

The potential of wind energy is immense. By addressing challenges and continuing to innovate, it can play a crucial role in transitioning to a sustainable energy future. The wind turbine embodies the breath of a benevolent force, working for the good of the planet and its inhabitants[1].

1.3 Assessment of Wind Energy in Algeria

The potential for wind energy in Algeria varies by geographical location. A wind map of Algeria , measured at 10 meters above ground, is shown in Figure 1-1. The annual average wind speeds range from 2 to 6.5 m/s. It is noted that, except for the coastal region (excluding Bejaia and Oran), the Tassili area, and Beni Abbés, the average wind speed exceeds 3 m/s.

The central region of Algeria typically has wind speeds ranging from 3 to 4 m/s, which increase as one moves southwest. The highest average wind speed is recorded in the Adrar region, at 6.5 m/s. Additionally, there are several microclimates where wind speeds surpass 5 m/s, such as in Tiaret and Oran[2].

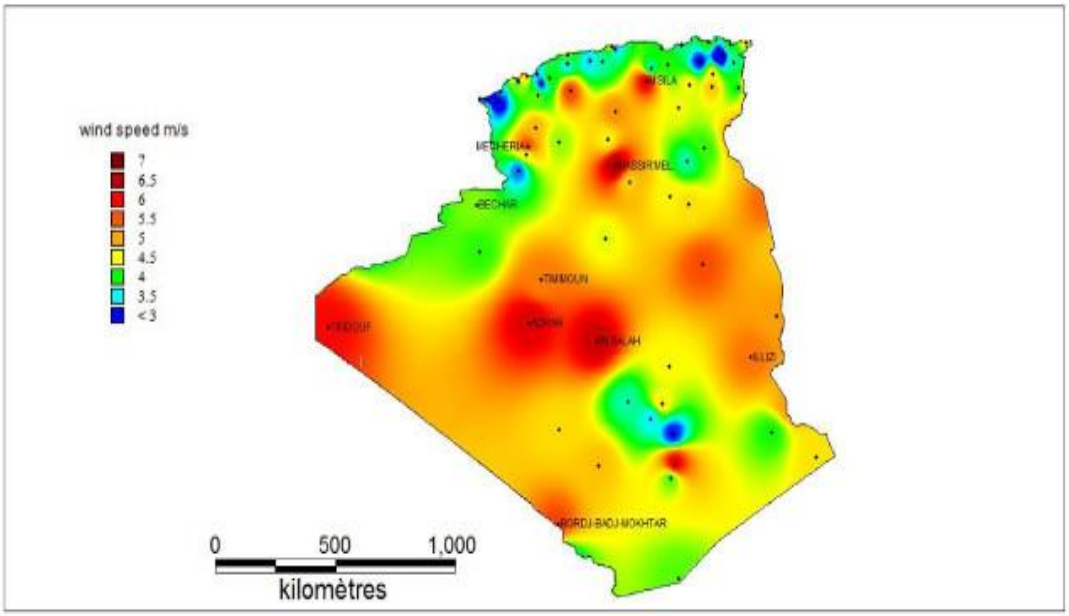

Figure 1-2: A wind map of Algeria

1.4 Wind turbines

1.4.1 Basic Wind Turbine

A wind turbine is a device designed to convert wind energy into mechanical energy. When air moves at a certain speed, it generates kinetic energy, commonly known as wind. The rotor of the wind turbine is exposed to the force of the wind, causing it to rotate and generate power [19].

The wind power conversion system, illustrated in Figure 1-3, primarily consists of :

- The wind turbine and its mechanical components, which convert a portion of wind energy into mechanical energy.
- An electric generator that converts mechanical energy available on the turbine's shaft into electrical energy.
- An electrical load, which can be static or dynamic, or an electrical power distribution network.
- A power electronics interface, typically situated between the generator and the load, which adjusts the electrical energy form supplied by the generator to meet the load's requirements.
- A control and regulation system that ensures optimal energy conversion in both steady-state and dynamic conditions.

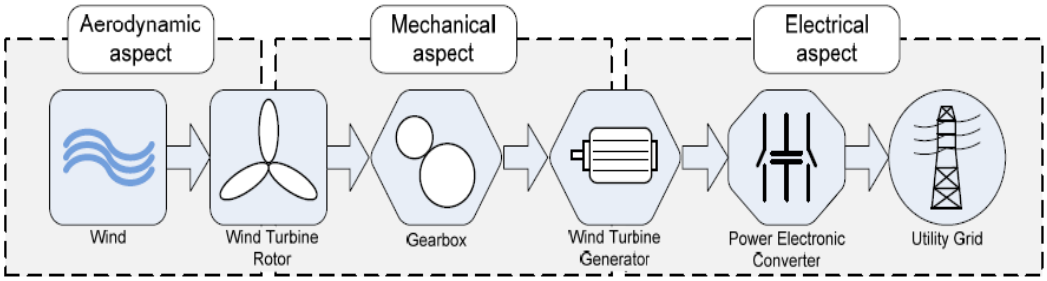

Figure 1-3: Wind energy conversion system

1.4.2 Main components of a wind turbine

There are various configurations of aerogenerators, and these can differ significantly in their design. The primary components (depicted in Figure 1-4) of a wind turbine, as described in [19] , are:

1. Foundations
2. Grid Coupling Cabinet
3. Mast
4. Ladder
5. Orientation System
6. Nacelle
7. Generator
8. Measurement Instruments
9. Brake
10. Gearbox
11. Blade
12. Blade Junction
13. Hub Cover

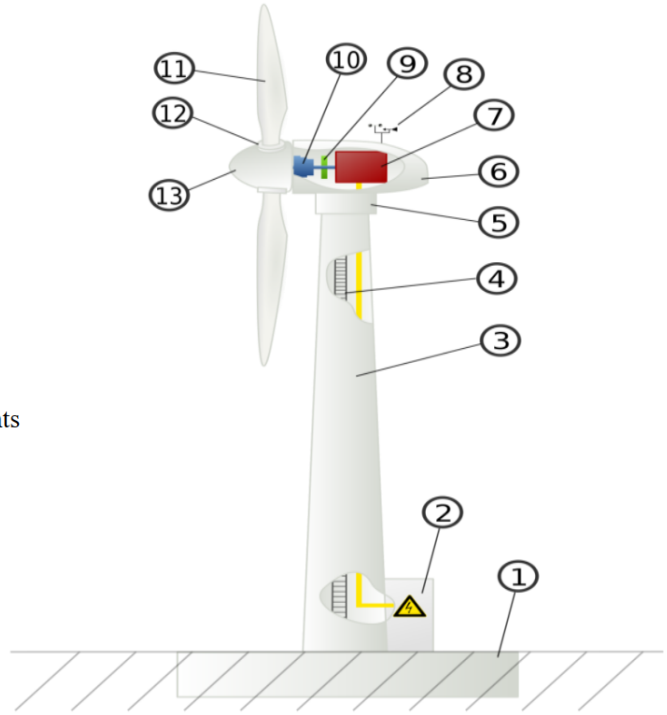

Figure 1-4 :Main Components of a Wind Turbine

Rotor Blades: Large, aerodynamically designed blades that capture the kinetic energy of the wind and convert it into rotational energy.

1. Rotor Hub: The central component to which the rotor blades are attached. It connects the blades to the rotor shaft.
2. Rotor Shaft: The shaft connected to the rotor hub, which transfers the rotational energy from the blades to the generator.
3. Generator: Converts the mechanical energy from the rotor shaft into electrical energy through electromagnetic induction.
4. Nacelle: The housing that contains the generator, gearbox, and other essential components. It sits atop the tower and houses the machinery that converts wind energy into electricity.
5. Gearbox: If present, it increases the rotational speed of the rotor shaft to match the optimal speed for the generator.
6. Tower: Supports the nacelle and rotor assembly, elevating the turbine to capture stronger winds at higher altitudes.

7. Controller: Monitors and controls the turbine's operation, including speed, direction, and pitch of the blades, to optimize energy production and ensure safe operation.

1.4.3 Classification

Wind turbines can be classified according to their size or according to their operating principle.

1.4.3.1 Classification according to size

Wind turbines come in a variety of sizes, and categorizing them by size is a common approach. While a turbine's height doesn't directly determine its power output, the key factor is the rotor's diameter, which creates the "swept area" that captures wind. Ideally, larger turbines will have a tower height (L) roughly equal to the rotor diameter (D) to maximize wind capture, although this isn't a strict rule [1],[19].

Here's a table outlining the standard size classifications and approximate power ranges for each category [1] . It's important to remember that these power estimates are indicative only. To get a more accurate picture, you'd also need to consider the wind speed at which the power is generated.

Table 1: Classification of Wind Turbines by Size [18]

Category	Rotor Diameter [m]	Swept Area [m²]	Power [kW]
Micro	0.5 - 1.25	0.2 - 1.2	0.25
Mini	1.25 - 3	1.2 - 7.1	1.5
Domestic	3 - 10	7 - 79	15
Small Commercial	10 - 20	79 - 314	100
Medium Commercial	20 - 50	314 - 1963	1000
Large Commercial	50 - 100	1963 - 7854	3000

1.4.3.2 Classification according to the principle of operation

Horizontal axis wind turbines (HAWT), as depicted in Figure 1-5, are the most widely recognized type of wind turbines. Their design is often standardized, featuring a mast at the base upon which the nacelle is situated. Inside the nacelle, both the generator and

transmission system are housed. Depending on the wind direction, the rotor can be positioned either upwind or downwind of the nacelle.

Figure 1-5: Example of Horizontal Axis Wind Turbines

The latter configuration has gained popularity due to its automatic wind-facing capabilities. In contrast, when the rotor is positioned upwind, additional mechanisms are required for proper alignment. These mechanisms may include a vertical stabilizing fin to orient the wind turbine against the wind or a motorized system to achieve this alignment. The former is referred to as a passive positioning device, while the latter is termed as an active positioning device (Figure 1-6) [19].

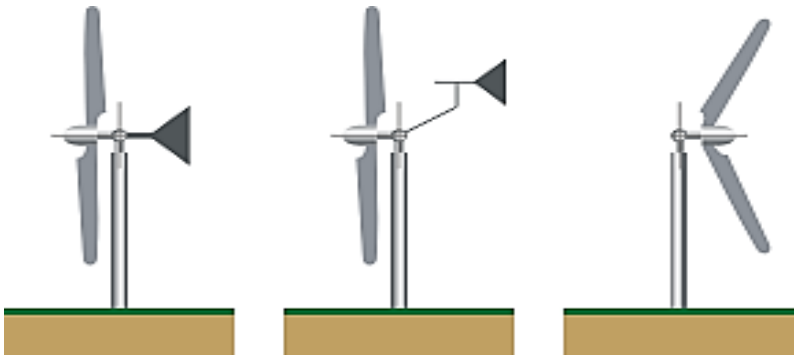

Figure 1-6: Distinction between Horizontal Axis Wind Turbines

The advantage of the rotor placed downstream is that it naturally positions itself facing the wind, that is to say passively. On the other hand, the wind is first disturbed by the nacelle and the pylon before acting on the rotor. On the one hand, the wind regime becomes non-uniform over the surface swept by the rotor. This generates mechanical stresses that vary over time, which causes premature wear of the equipment. On the other hand, the disturbing wind impacts the blades of the wind turbine which tends to generate a lot of noise (noise of aerodynamic origin). For these two reasons, the configuration with the rotor upstream is preferred. Indeed, the wind is less disturbed before meeting the blades of the wind turbine. Finally, we can say that the horizontal axis wind turbine with the rotor upstream has become the standard, at least for high power applications.

There are also vertical axis wind turbines (VAWT) (Figure 1-7) for small to medium power applications. The advantages of this configuration are that the wind turbine is always well positioned about the wind that the coupling device and the generator are at ground level, which facilitates maintenance. In addition, due to the smaller rotor diameters of horizontal axis wind turbines, the absolute speeds are lower which, at least theoretically, should generate less noise.

Classically, there are two main families among vertical axis wind turbines (Figure 1-7). On the one hand, there are wind turbines based on "lift", the best known of which is the "Darrieus" model and, on the other hand, wind turbines based on "drag", the best known of which is the "Darrieus" model. "Savonius". We invite the reader who wants to deepen these concepts to consult specialized sites [19]. Note, however, that by the physical principle of these models, they give little torque at start-up. Therefore, they only start at a certain wind speed, or it is necessary to ensure the start of the wind turbine mechanically.

In the history of wind turbines, there is cyclically a resurgence of interest in vertical axis wind turbines. The new concepts proposed are supposed to exceed the technological limits of the current standard which is the horizontal axis wind turbine with the upstream rotor. Here are some elements of reflection to situate the debate on these VAWTs [19]:

- Concerning new vertical axis wind turbines, it is often a matter of rediscovering old concepts.

- In general, there is a lack of experience feedback on the behavior of new vertical axis wind turbines, particularly about their performance, both technically and from an economic point of view.
- Many experts who have accumulated a long experience in wind power are skeptical.
- Many announcements affect the performance of these new concepts without validating them.

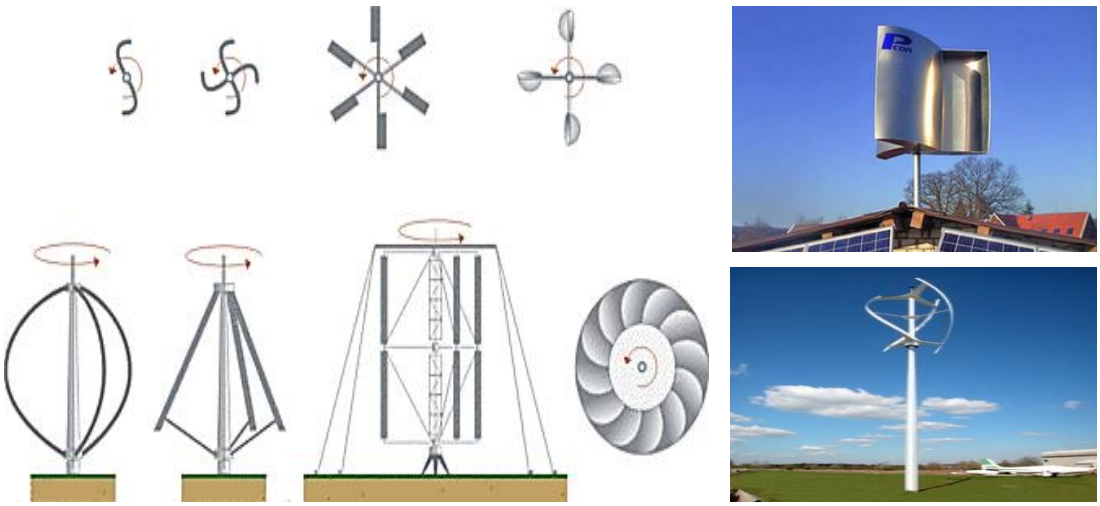

Figure 1-7: Savonius and Darrieus Wind Turbines

1.5 The generator and the dynamics of the rotor

The generator is a key component of a wind turbine, responsible for converting mechanical energy into electrical energy. The turbine blades harness the wind's kinetic energy, converting it into mechanical energy, which is then transmitted to the generator through the transmission system. Once the electrical energy is generated, it is typically fed into the electrical grid.

For horizontal axis wind turbines, the transmission system follows a relatively standard configuration (Figure 1-8). The blades, subject to wind forces, rotate at a certain speed. These blades are attached to a hub, which is connected to the transmission shaft. This shaft is responsible for transmitting mechanical torque to the generator. The generator itself consists of two primary parts: a stator and a rotor.

Typically, a gearbox is placed between the turbine's shaft and the generator. This is necessary because most generators require a much higher rotor speed than that of the wind

turbine's rotor. The gearbox multiplies the rotor speed, enabling effective coupling between the wind turbine and the generator [1].

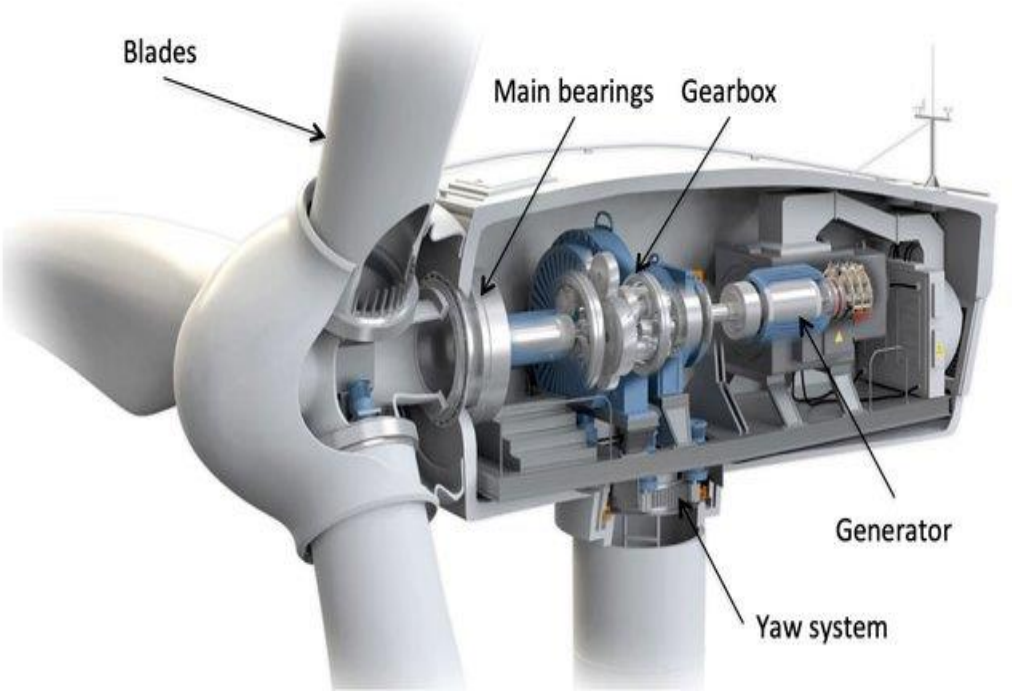

Figure 1-8: The Transmission between the Blades and the Generator

We see that we find, on the one hand, the mechanical torque exerted by the aerodynamic forces on the blades of the wind turbine, and on the other hand, the braking torque exerted by the generator on the rotor. Indeed, if the shaft exerts a certain torque on the generator, then the generator exerts by reaction a braking torque on its rotor. A gearbox is often interposed between the two ends to make the speeds of rotation compatible. The rotor of the wind turbine as well as the rotor of the generator represents the main contributions to the inertia of the transmission chain [1].

1.6 Wind turbine system topologies and generators

Several criteria are considered in determining the topology and type of generator used for wind energy production, such as the type relative to speed, whether it's a fixed or variable-speed turbine, the power rating which can range from small to large-scale turbines, or whether the turbine is grid-connected or standalone [17]. Generally, there are two types of generators used in wind turbines: asynchronous and synchronous.

1.6.1 Wind turbines using asynchronous machines

Advancements in power electronics have made asynchronous generators one of the preferred choices in aerodynamic electricity generation; this type of generator is cost-effective, robust, and requires minimal maintenance. However, the main drawback of this type is the need to use a reactive power recovery device (capacitors).

There are several types of asynchronous generators used in wind turbines, but in practice, two types are most commonly used for economic and energy reasons: squirrel-cage induction generators (SCIG) and Doubly-Fed Induction Generator (DFIG) [19].

1.6.1.1 Doubly-Fed Induction Generator

Figure 1-9 shows the simplified diagram of a wind turbine based on a DFIG, where the stator windings are directly connected to the grid (the amplitude and frequency of the voltage are fixed and imposed by the grid) and the rotor windings are connected to the grid through two back-to-back power converters connected with a DC bus based on capacitors acting as a source of DC voltage.

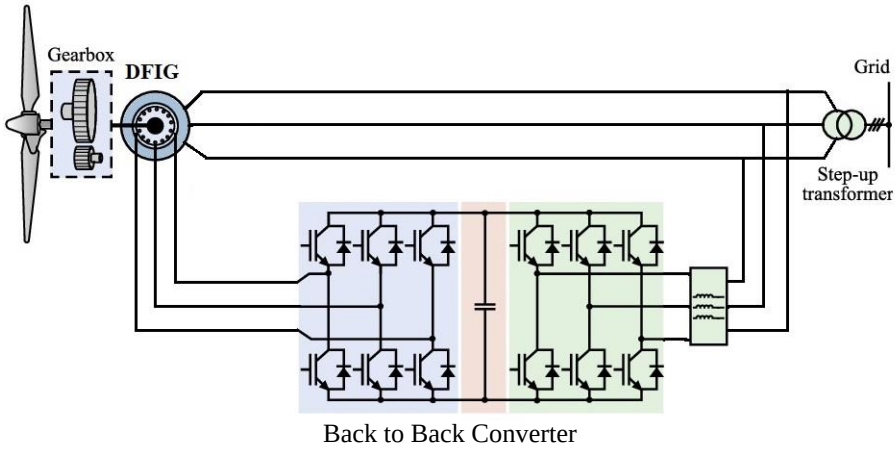

Figure 1-9: Wind turbine based on a DFIG

The principle of this type is based on controlling the flow of slip power; the rotor-side converter control allows us to adjust the electromagnetic torque of the system and recover some of the rotor power to inject it into the grid [19]. On the other hand, the grid-side converter regulates the DC link in order to achieve an output voltage with a frequency equivalent to that of the grid [19].

Compared to other types of generators, DFIG offers the following advantages:

- Reduced inverter cost, as the converters are sized only for a power range between 25 to 30% of the machine's rated power [20];
- Decreased static converter power, allowing for the minimization of filtering and conversion components;
- Robustness and stable response to external disturbances.

One of the disadvantages of DFIG is the use of slip rings which require periodic maintenance [20].

1.6.1.2 Squirrel-Cage Induction Generator (SCIG)

This device is considered the simplest and most commonly used, in which the rotor of the SCIG is mechanically coupled to the wind turbine's drive shaft via a speed multiplier, and where the stator is directly connected to the grid (see Figure 1-10) [21]. The number of pole pairs of the generator is fixed, so it must operate over a very limited speed range (slip less than 2%). Since the frequency is imposed by the grid, if the slip becomes too significant, stator currents of the machine increase and can become destructive. Therefore, to ensure stable operation of the device, the generator must maintain a rotational speed close to synchronism (point g=0).

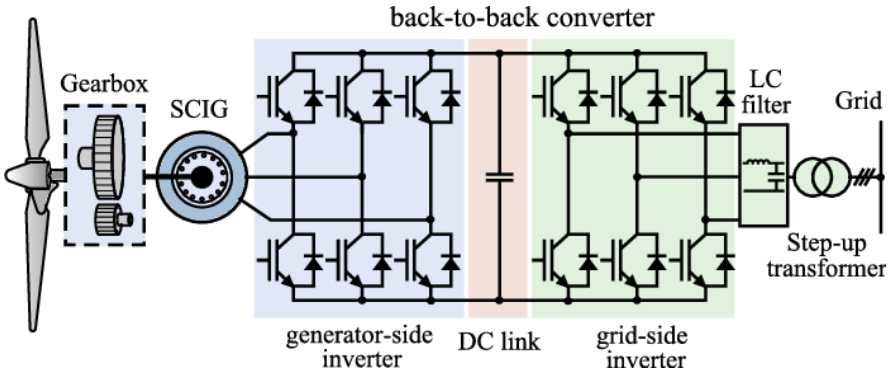

Figure 1-10: Wind turbine based on a SCIG

As SCIG is a fixed-speed generator, for a particular wind speed, the active output power is also fixed. Thus, with increasing wind speed, the output power increases similarly until the rated power is reached. The wind speed at this moment is referred to as the rated wind speed. Beyond this speed, the pitch angle control system will prevent the output power from exceeding the rated value. In other words, when the wind speed is lower than the rated value, the captured power can vary based on the wind speed; and

when the wind speed is higher than the rated value, the system will limit the generated power by controlling the pitch angle (wind speed control) [22].

1.6.2 Wind turbines using synchronous machines

Different topologies are available in this type of wind turbine system, and each topology has its own advantages and disadvantages. However, there are two topologies that are most common and have become very competitive compared to systems using asynchronous machines: the wound rotor synchronous generator (WRSG) and the permanent magnet synchronous generator (PMSG).

1.6.2.1 Wound Rotor Synchronous Generator (WRSG)

In this type, direct connection of the stator windings to the grid is not possible due to the variation in the frequency of the generated voltage, which depends on the rotational speed of the rotor and consequently on the wind speed. Therefore, the stator must be connected to the grid via a separate back-to-back converter separated by a DC bus (see Figure 1-11); the rotor-side converter converts the voltage generated by the generator into DC voltage and also allows speed control. The DC bus acts as a continuous voltage regulator, generally reacting as a voltage source; the rotor-side converter converts the DC voltage back into AC voltage, with an amplitude and frequency similar to those of the grid, and also ensures maximum power recovery and injection into the grid with reactive power compensation[23].

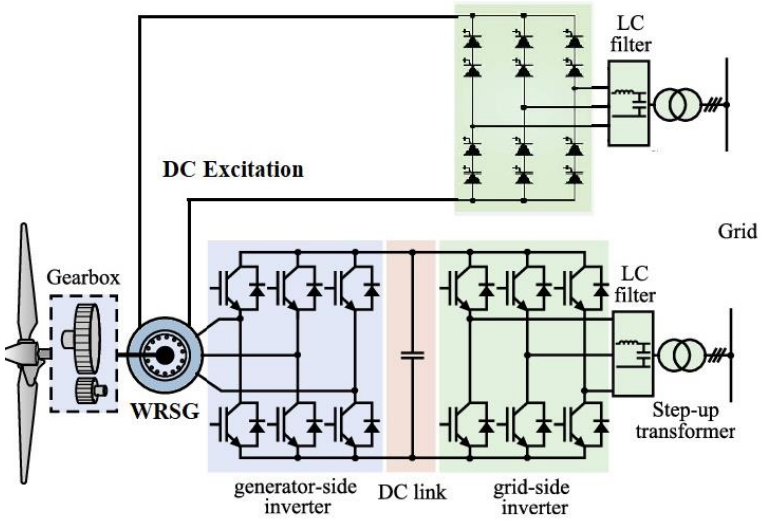

Figure 1-11: Wind turbine based on a WRSG

This type of generator has several advantages compared to other types such as:

- Elimination of the gearbox; direct coupling to the wind turbine.
- Higher efficiency compared to asynchronous generators, because the stator current is used for electromagnetic torque generation.
- Operation over a wide speed range [24].

However, this system based on a WRSG requires regular maintenance of the sliding contacts system, and it requires an external excitation circuit provided by a rectifier connected to the grid.

1.6.2.2 Permanent Magnet Synchronous Generator (PMSG)

The rotor of this type is constructed from a permanent magnet, which offers several advantages over other types of generators, such as low maintenance costs, the possibility of eliminating the gearbox, and consequently eliminating the disturbances, noise, and energy losses caused by the gearbox with the use of a large number of pole pairs [23]. Depending on the conversion system used to inject the produced energy into the grid, two types can be cited [21]:

Unidirectional conversion system: Figure 1-12 shows a wind turbine system based on a PMSG connected to the grid via a unidirectional converter consisting of a diode rectifier controlling the electromagnetic torque, followed by a boost converter increasing the DC voltage and feeding a PWM inverter, the latter ensuring control of the DC voltage and allowing maximum power injection into the grid while ensuring a better power factor is maintained [21][23].

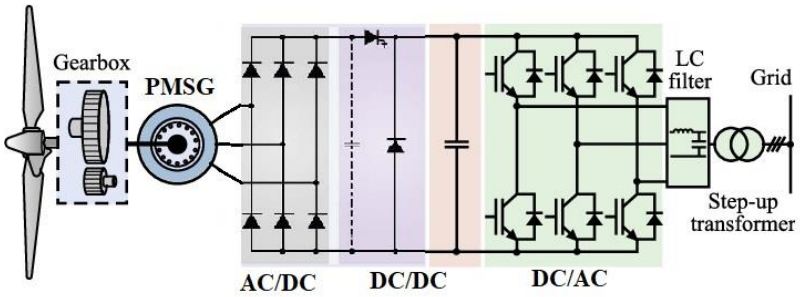

Figure 1-12 Wind turbine system based on a PMSG

The disadvantage of this type is the distortion of the stator current waveform caused by the use of a diode rectifier, resulting in the production of harmonics and torque ripples and increasing energy losses [23].

Bidirectional conversion system: In this type, energy flows in both directions, from the generator to the grid or from the grid to the wind turbine, which acts as a consuming load in this case; the connection of the stator windings to the grid is ensured by a back-to-back converter with a DC bus in the middle, as presented in Figure 1-13, in this configuration, both converters are equipped with IGBTs, which gives an advantage to this configuration over the previous one in terms of optimal control of the PMSG, with minimization of losses in the stator [21].

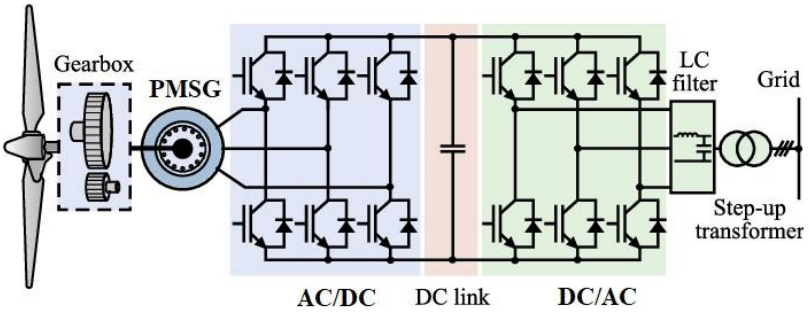

Figure 1-13 Wind turbine system based on a PMSG type 2

1.7 Evaluation of Control Methods for DFIG

Wind turbines equipped with DFIG are currently the most prevalent solution for harnessing wind energy, especially in onshore wind farms [25]. This dominance of the DFIG-based system is reflected in the extensive research and numerous publications dedicated to it over the past few decades. The primary focus of this research is to enhance the efficiency and performance of these wind turbines[26], [27].

Key objectives include[28],[29].:

- **Maximizing Power Extraction:** Wind speeds fluctuate, making it critical for turbines to capture as much power as possible across a wide range of wind speeds. By optimizing control strategies, the turbine can adjust to varying conditions, ensuring it consistently extracts maximum available power.

- **Precise Control of Active and Reactive Power:** Wind turbines need to deliver not just active power (real power) but also reactive power to the grid. Precise control of both is essential for the stability and efficiency of the electrical grid. The active power helps meet demand, while reactive power supports voltage levels in the grid.
- **Reducing Oscillations and Harmonics:** Wind turbines, like other electrical machines, can suffer from torque oscillations and generate harmonic distortions in the current and power they produce. These distortions and oscillations reduce efficiency, stress mechanical components, and can cause power quality issues in the grid. The goal is to minimize these effects.
- **Handling Grid Disturbances:** Modern wind turbines are required to remain operational during grid disturbances, such as voltage dips or frequency fluctuations, to help stabilize the grid. This is crucial for maintaining a reliable energy supply, especially as renewable energy sources like wind power become more integral to the energy mix.

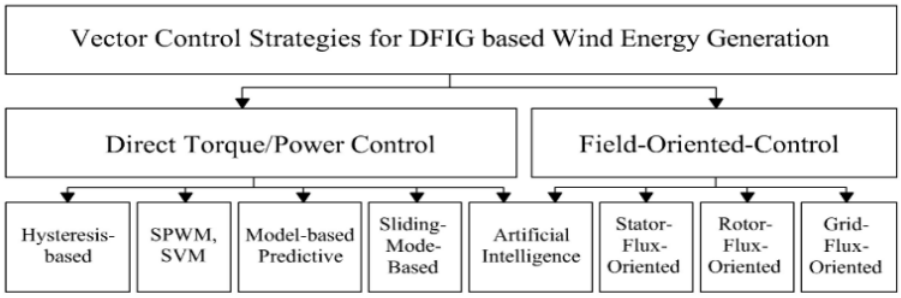

Figure 1-14 Classification of induction machines control methods

Most advanced control methods developed for induction motors since 1974 can be adapted for DFIG [25]. However, controlling a DFIG is inherently more complex than controlling a standard induction motor. Numerous combinations of control strategies exist, each with its own set of advantages and disadvantages [28],[29]. **Error! Reference s ource not found.** illustrates the classification of control strategies in the DFIG market.

1.7.1 Traditional Control Methods

Historically, the most widely used control strategy for DFIG-based turbines is Stator Flux Orientation Control (FOC) [28],[30], managed by proportional-integral (PI)

regulators. This method aligns the control of the machine with the magnetic field generated by the stator, simplifying the control of power output. However, while effective, the performance of PI control is generally moderate. Its primary drawback is its limited robustness when facing grid disturbances or changes in the turbine's internal parameters, which can lead to instability and suboptimal performance.

1.7.2 Advanced Control Strategies

To overcome the limitations of traditional methods, various advanced control techniques have been proposed:

Direct Torque Control (DTC) and Direct Power Control (DPC): Both DTC [31],[32] and DPC [29],[33] offer more direct control of torque and power compared to FOC. They are effective in reducing Total Harmonic Distortion (THD) in the stator current, leading to smoother operation. However, the use of traditional hysteresis comparators in these strategies can introduce torque and flux ripples, causing performance issues.

Sliding Mode Control (SMC) [34]. SMC is a robust nonlinear control method that is particularly effective in systems with uncertainties or disturbances. It forces the system to "slide" along a desired trajectory, maintaining control even under changing conditions. However, the traditional SMC has a drawback known as the "chattering" effect, where the system experiences high-frequency oscillations that can cause mechanical wear and reduce control accuracy [45].

Neural Networks (NN): These use artificial intelligence to model and control the system, adapting to changing conditions more effectively than traditional controllers. Neural networks can learn from data and improve their control actions over time, providing more adaptive and efficient control of the wind turbine[35].

Fuzzy Logic Control (FLC): Fuzzy logic controllers mimic human reasoning to handle uncertainty and imprecision, making them effective in dealing with the complex dynamics of wind turbines. Unlike traditional controllers, which rely on precise models, FLC uses approximate rules to make decisions, offering flexibility in variable wind conditions [36].

Fractional-Order Control: One of the most promising advancements in control methods is the introduction of Fractional-Order Proportional-Integral-Derivative (FOPID) controllers. Unlike conventional PID controllers, FOPID controllers have two additional tuning parameters δ and μ which provide more flexibility. These extra degrees of freedom allow for finer adjustments, improving both the system's response time and robustness. FOPID controllers are particularly effective in handling the nonlinear dynamics of wind turbines, making them a valuable tool for enhancing the overall performance of DFIG-based systems [73].

In summary, various control strategies have been developed and continue to evolve to enhance the performance of DFIG-based wind turbines. These strategies focus on maximizing power extraction, improving power quality, reducing mechanical stress, and enhancing the system's robustness to disturbances. Through the integration of advanced control techniques such as artificial intelligence, sliding mode control, and fractional-order controllers, significant improvements in wind turbine efficiency and grid compatibility can be achieved [72].

1.8 Conclusion

In this chapter, we provided an overview of global wind energy, exploring different types of wind turbines based on their rotation axes and operating speeds, whether fixed or variable. We discussed the advantages and disadvantages of each type and their practical applications. Additionally, we examined the various components of a horizontal-axis wind turbine. The second part of this chapter was devoted to the principle of mechanical and electromagnetic conversion, and to the various types and topologies of generators used in wind systems. We compared control systems based on asynchronous machines, which we found to be the most commonly used in this type.

2 Modeling and Control of a Wind Turbine

2.1 Introduction:

The operation of a wind turbine relies on both mechanical and electrical control systems to ensure optimal energy production and system efficiency. These systems work in tandem to regulate the behavior of the turbine under varying wind conditions, safeguarding against mechanical stress and maximizing power output.

The mechanical control system primarily governs the physical components of the turbine, such as the orientation of the blades and their pitch angle. Adjusting the blade angle relative to the wind direction, a process known as pitch control, allows the turbine to optimize aerodynamic performance. This is crucial, particularly in high wind speeds, to prevent damage and maintain efficiency.

The electrical control system is responsible for managing the generator and associated power electronics. It ensures the conversion of mechanical energy into electrical energy is smooth and controlled, allowing precise regulation of power output. This system must respond dynamically to changing conditions, such as fluctuations in wind speed, electrical load, and the rotational speed of the turbine.

This chapter focuses on the wind turbine's dynamic behavior under various operational conditions. Understanding this behavior is vital for designing control strategies that enhance efficiency and maintain system stability. The first step in this process is developing a mathematical model that accurately describes the turbine's behavior. This model must account for both intrinsic parameters the inherent characteristics of the system and controllable parameters that can be adjusted to influence turbine performance.

2.2 Modeling a wind turbine

On the shaft of the wind turbine, there is the wind turbine rotor and the nacelle contains the gearbox and the electrical generator. Wind turbine rotor consists of several fixed or orientable blades, 80% of manufacturers manufacture three-bladed turbines for reasons of stability, weight, and mechanical fluctuations. The wind turbine, in general, rotates at a rated speed of 25 to 40 (rpm).

The gearbox adapts the speed of the wind turbine to that of the electric generator which rotates at approximately 1500 (rpm).

2.2.1 Wind models

The wind is the very reason for the existence of wind turbines. The kinetic energy contained in the wind is partially transformed into mechanical energy by the turbine and then into electrical energy by the generator. Accurately measuring the wind at the height of the turbines is quite complex. However, wind can be represented as a random variable defined by statistical parameters. Numerous studies have been conducted on wind modeling. One of the principles adopted is to generate the temporal pattern of the wind from white noise, onto which a transfer function is applied, to be determined. The parameters of this transfer function depend on characteristic quantities of the site and the nature of the wind [6].

2.2.2 Fixe Wind Expression at a Fixed Point

The wind speed at a point $S_0(t)$ can be decomposed into a sum of an average component $S(t)$ and a variable component representing the fluctuations $S_t(t)$:

$$S_0(t) = S(t) + S_t(t) \qquad (2\text{-}1)$$

The component representing the turbulence $S_t(t)$ is characterized by the length scale L_v and the standard deviation σ_v of this turbulence. The turbulence length scale is associated with the average size of the eddies. The definition of the turbulent component is done in 2 steps :

1st step: Reconstruction of the turbulence spectrum from filtered white noise.

Von Karman proposed using a non-integer order transfer function [7], [8]. It can be approximated in the following form:

$$\vartheta_s(s) = \frac{K_v(m_1 T_v S+1)}{(1+T_v S)(1+m_2 T_v S)} \qquad (2\text{-}2)$$

With m_1 = 0.4 and m_2 = 0.25.

All parameters necessary for calibration of the spectral density function can be derived from on-site measured data, as detailed in [7].

2nd step: definition of the turbulence standard deviation σ_v , the standard deviation depends on the average speed *S* and a coefficient k_σ which represents the intensity of the turbulence:

$$\sigma_v = k_\sigma S \qquad (2\text{-}3)$$

In [6] [7] [8] gives orders of magnitude of turbulence intensity and length scale for various sites. Thus, from a Gaussian white noise input, it is possible to determine the composition of the turbulence and therefore to generate a *t*ime series of *t*he wind speed at a point $S_0(t)$ as presented in Figure 2-1. The wind is defined by 3 parameters:

- An average speed of S
- A coefficient of variance k_σ (between 0.1 at sea and 0.25 in a turbulent zone)
- a turbulence length scale L_v (between 100 at sea and 500 in a turbulent zone)

For our case study, we have chosen a set of the following parameters (k_σ = 0.13 et L_v = 125).

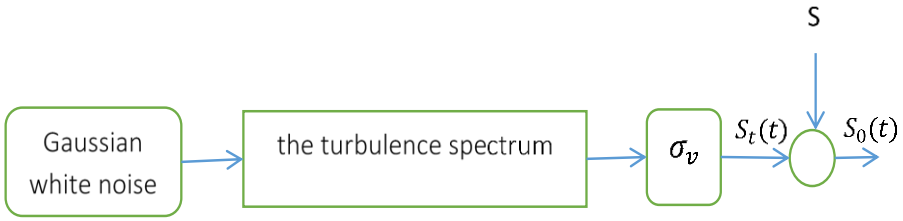

Figure 2-1 Construction of wind speed

2.2.3 Spatial Filter

The wind speed at a point in the area swept by the aero-turbine must make it possible to find the wind torque close to that which would be produced by the real incident wind speed field over the entire area swept by the rotor. It has been experimentally demonstrated that only the low-frequency components of the incident wind are found in the total torque produced by the blades. On the other hand, the aero-turbine filters high-frequency fluctuations [6] [8]. This effect is reconstructed by applying to the instantaneous wind speed a filter whose simplified transfer function is given by:

$$\frac{1}{1+s(\gamma R_t/S)} \qquad (2\text{-}4)$$

- R_t *Wind turbine blade radius*
- γ *Attenuation factor on the rotor* ($\gamma = 1.3$)

Figure 2-2 shows the evolution of the wind speed after the spatial filter.

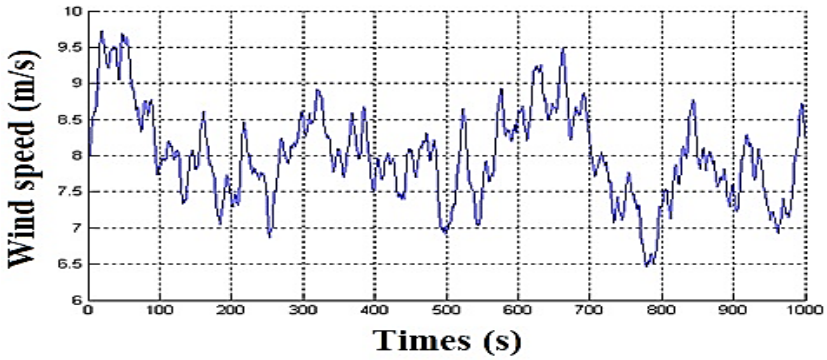

Figure 2-2 Wind Profile

2.3 Aerodynamic Model

The wind rotor functions as an energy conversion system, converting the kinetic energy of moving air masses into mechanical energy accessible on the shaft. This kinetic energy is directly proportional to the mass of air moving at a specific velocity. Energy extraction occurs by decelerating the air passing through the rotor via a mechanism that transforms the forces acting on the blades.

The theory of momentum is employed to analyze the wind turbine's behavior and to establish certain assumptions. These assumptions include the incompressibility of air, the steadiness of fluid motion, and the uniformity of studied variables across a given section of the air stream tube. (Figure 2-3*).*

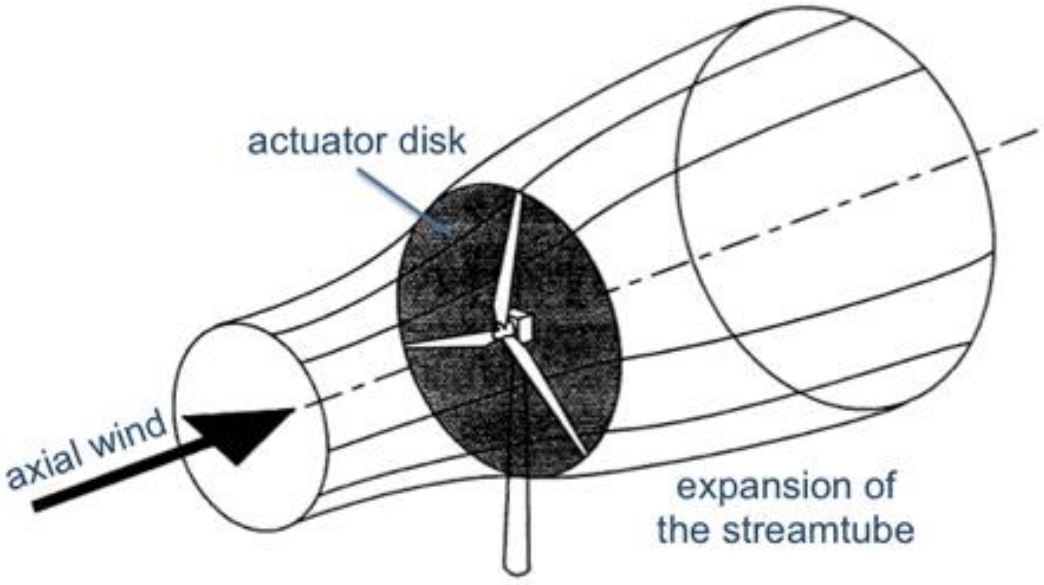

Figure 2-3 Fluid Stream Passing through the Wind Rotor

To harness the kinetic energy of moving air masses, the wind turbine blades are angled obliquely to the wind, characterized by an angle known as the pitch angle, β, inducing rotation akin to a screw.

The wind turbine can only capture this power [48], [49]:

$$P_t = \frac{1}{2}\rho\pi R^2 V_\omega^3 C_p(\lambda, \beta) \quad (2\text{-}5)$$

Where*:*

- R *The radius of the wind turbine*
- ρ *The air density*
- V_w *The wind speed*
- C_p The power coefficient

C_p is a dimensionless parameter that indicates the efficiency of the *w*ind turbine in converting the kinetic energy of the wind into mechanical energy. This coefficient is determined by the *pitch angle* β and the *tip speed ratio* λ , defined as [48],[10]:

$$\lambda = \frac{\Omega_t R}{V_w} \quad (2\text{-}6)$$

Where Ω_t is the angular *s*peed of the rotor. The theoretical *m*aximum value of C_p is given by the *Betz limit* $C_{p-max} = 0.593$ [50],[7].

The rotor torque is obtained from the power received and the speed of rotation of the turbine and it is directly determined by:

$$T_t = \frac{P_t}{\Omega_t} = \frac{1}{2}\rho\pi R^2 V_\omega^3 C_p(\lambda, \beta)\frac{1}{\Omega_t} \quad (2\text{-}7)$$

2.3.1 Modeling of the coefficient of power

As noted in [9] [3], a straightforward method to depict the torque and C_p is through analytical expressions reliant on λ and β. One widely utilized expression, easily adaptable to different turbine configurations, is [6],[7]:

$$C_p(\lambda, \beta) = C_1(C_2 + C_3\beta - C_4\beta^x + C_5)e^{-C_6} \quad (2\text{-}8)$$

The six coefficients defined, c1, c2, c3, c4, c5, c6, depending on the considered turbine:

$c_1 = 0.5$, $c_2 = 116/\lambda_i$, $c_3 = 0.4, c_4 = 0$, $c_5 = 5$, $c_6 = 21/\lambda_i$, $\lambda_i = \left(\frac{1}{\lambda+0.08\beta} - \frac{0.035}{\beta^3+1}\right)^{-1}$

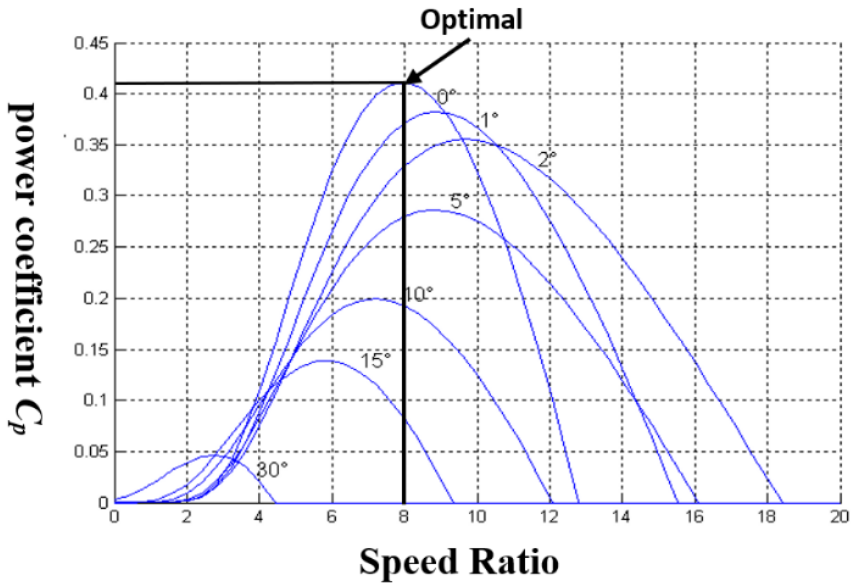

Figure 2-4: Curves of the Cp(λ ,β) Coefficient

In Figure 2-4, several curves $C_p(\lambda, \beta)$ are available but we are interested in the one with the highest peak. This curve is characterized by the optimum point ($\lambda_{opt} = 8.1$, $C_{p-max} = 0.415$, $\beta = 0$ (deg)) which is the point corresponding to the maximum of the power coefficient C_p and therefore to the maximum of the recovered mechanical power. We notice that the increase of β makes it possible to degrade the coefficient C_p and consequently, to cause the reduction of the mechanical power recovered on the axis of the wind turbine.

The block diagram which represents the wind turbine is illustrated on the Figure 2-5.

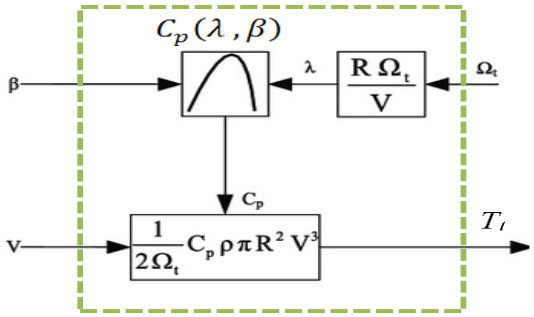

Figure 2-5 Wind Turbine Model

2.4 Mechanical System

The power transmission system comprises the blades attached to the hub, which are then linked to the slow shaft. This slow shaft is connected to the gearbox, responsible for increasing the rotational speed, ultimately connected to the fast shaft driving the generator.

In our simulation model, we simplify the gearbox as rigid, represented by a basic gain, we neglect any elasticity and friction within the multiplier, assuming zero energy losses.

The mechanical torque produced by the wind turbine is divided by the gearbox ratio G to determine the mechanical torque applied to the generator shaft [7].

$$T_{mec} = \frac{T_t}{G} \quad (2\text{-}9)$$

The gearbox adapts the speed of the turbine to that of the generator as follows

$$\Omega_t = \frac{\Omega_m}{G} \quad (2\text{-}10)$$

The generator shaft is modeled by the following equation:

$$J\frac{d\Omega_m}{dt} = T_m - T_{em} - F\Omega_m \quad (2\text{-}11)$$

Where :

- J $Total\ inertia\ of\ rotating\ parts$ $(Kg.m2)$
- F $The\ friction\ coefficients$
- $Tm + Tem$ $Total\ wind\ turbine\ torque.$
- Tem $Electromagnetic\ torque\ of\ the\ generator\ in$ $(N.m)$

The total inertia is the sum of the inertia of the generator and the turbine brought back to the generator side:

$$J = \frac{J_t}{G^2} + J_{gen} \quad (2\text{-}12)$$

The following block diagram represents the model of the wind turbine shaft associated with the turbine model.

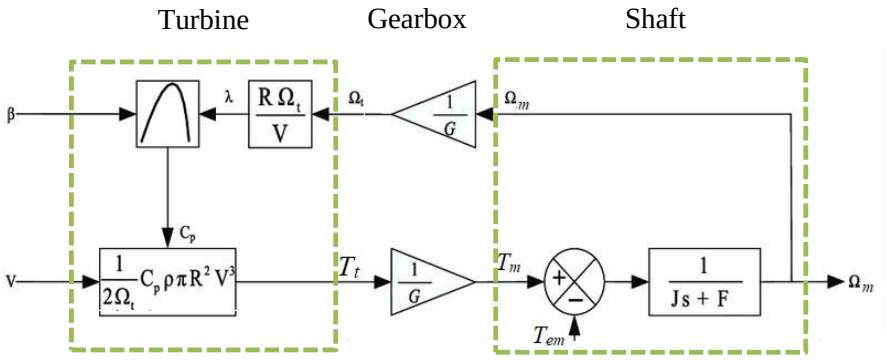

Figure 2-6 Model of the Wind Turbine Shaft

2.5 Wind Turbine Power Management Strategy

The common approach in wind energy systems, as highlighted in studies [51] and [52], involves the use of variable speed wind turbines. This configuration is divided into two operational zones based on wind speed, as shown in Figure 2-7.

The $cut-in\ wind\ speed\ V_{cut-in}$, is the minimum wind speed at which the wind turbine can sustain continuous power generation. When wind speeds are below the *rated speed,* V_{rated}, an MPPT controller is employed to continuously monitor and adjust the turbine to its optimal operating point, maximizing the output power of the wind turbine.

Conversely, when wind speeds exceed V_{rated}, measures are taken to limit the power extracted from the wind turbine to its rated level, ensuring that wind speeds do not surpass the *cut-out wind speed* $V_{cut-out}$, which is the maximum wind speed that the turbine can withstand without causing damage to the blades, generator, or other components. This preventive measure is crucial for protecting these components, and it is achieved by maintaining the generator speed at the rated value through pitch angle control.

The primary objective of power control for a variable speed wind turbine is to optimize the extraction of mechanical power from the turbine across various wind speeds while ensuring that the generator speed and mechanical power remain within their nominal values to prevent potential damage to the turbine and power converter components [53],[54].

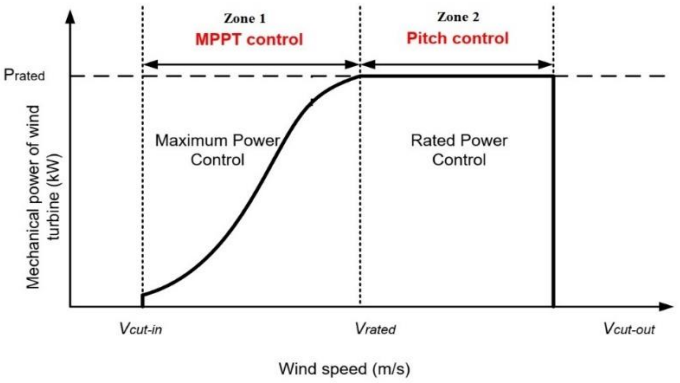

Figure 2-7 Variable speed wind turbine control

This control objective is visualized through a speed reference trajectory depicted in a $P_m - \omega$ plane, covering the entire range of wind speeds as illustrated in Figure 2-8. During wind speeds below the rated threshold, the control system generates an optimal speed reference trajectory to maximize the mechanical power harvested from the wind turbine, achieved through the utilization of a MPPT controller. Conversely, when wind speeds exceed the rated level, the control system generates an optimal speed reference trajectory aimed at constraining the mechanical power output to its rated value, facilitated by pitch angle control mechanisms.

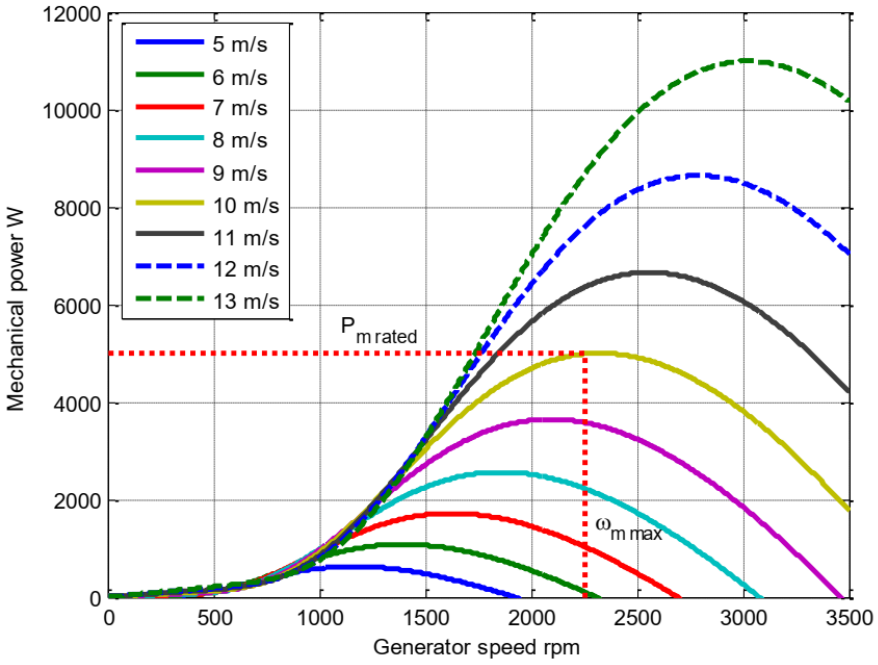

Figure 2-8 Speed reference trajectory in different wind speed

2.5.1 Maximum power point tracking (MPPT) control

Figure 2-9 illustrates the relationship between C_p and λ. We can observe that for a zero pitch angle ($\theta = 0°$), the maximum power coefficient C_{pmax} is achieved at the optimal tip-speed ratio (λ_{opt}).

Equation (2.6) indicates that changes in *w*ind speed also influence the *w*ind turbine's rotational speed. This adjustment helps maintain the optimal tip-speed ratio, ensuring maximum power capture from the *w*ind.

Using equation (2.5), one can compute the maximum mechanical power generated by the *w*ind turbine:

$$P_{m\_max} = \frac{1}{2}\rho\pi R^5 \frac{C_{pmax}}{\lambda_{opt}^3}\omega_m^3 \qquad (2\text{-}13)$$

where

$$k_{opt} = \frac{1}{2}\rho\pi R^5 \frac{C_{pmax}}{\lambda_{opt}^3} \qquad (2\text{-}14)$$

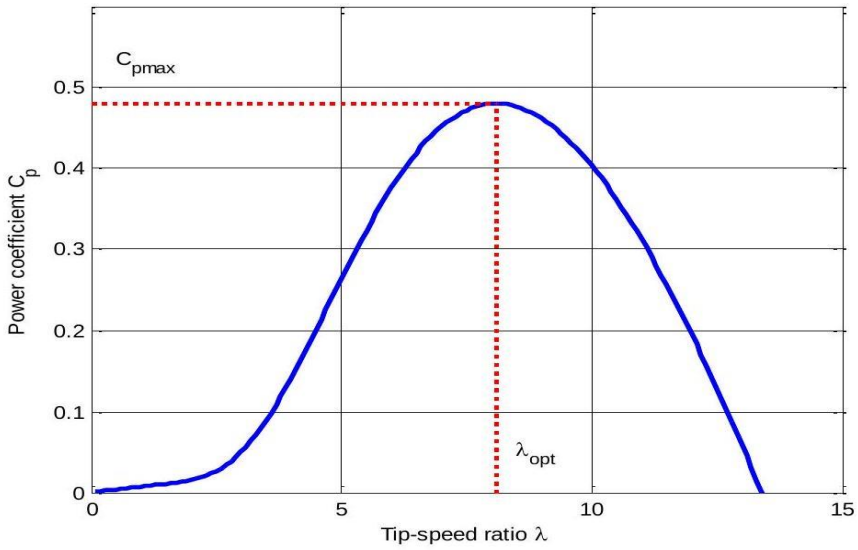

Figure 2-9 C_p-λ characteristics of wind turbine

2.5.2 MPPT Control with Speed Sensor

Implementing this control necessitates the utilization of an anemometer for precise wind speed measurement and relies on the knowledge of the wind turbine's λ_{opt} ⁻ V_w curve. Expressing the optimal speed reference involves the following steps [55]:

$$\omega_{m\_ref} = \frac{\lambda_{opt} V_w}{R} \quad (2\text{-}15)$$

As depicted in Figure 2.10, the block diagram of the MPPT is shown.

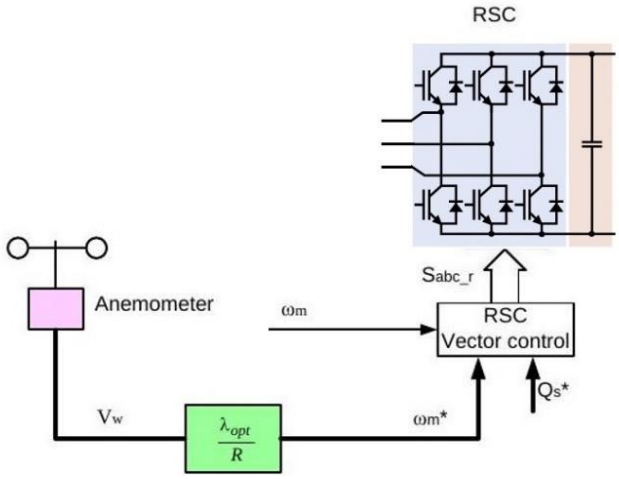

Figure 2-10 MPPT Control with Speed Sensor

The MPPT control technique involves adjusting the generator speed to uphold the Tip-speed ratio at its optimal value, λ_{opt}, which corresponds to the *w*ind turbine's maximum power extraction, as outlined in equation (2.6). This MPPT control implementation requires precise *w*ind speed and generator *s*peed sensors, along with knowledge of the wind turbine's design characteristics at the optimal λ_{opt}. MPPT offers notable benefits, including high efficiency and swift tracking capabilities, as the *s*peed reference for *m*aximizing power output can be directly derived from the wind speed, as indicated in equation (2.13) . However, integrating a wind speed sensor for MPPT adds to the overall cost and may raise concerns regarding reliability [55],[56].

2.5.3 Sensorless MPPT control

obviates the necessity for a wind speed sensor and strives to maximize the mechanical power extracted from the wind turbine by consistently monitoring the optimal power point at $\lambda=\lambda_{opt}$ and $C_p=C_{pmax}$. Consequently, the optimal mechanical power reference can be ascertained utilizing equations (2.13) and (2.14) [57]. The block diagram illustrating the MPPT is depicted in Figure 2.11.

$$P_{m\_ref} = k_{opt}\omega_m^3 \quad (2\text{-}16)$$

and the optimal speed reference can also be expressed as:

$$\omega_{m\_ref} = \sqrt[3]{\frac{P_m}{k_{opt}}} \quad (2\text{-}17)$$

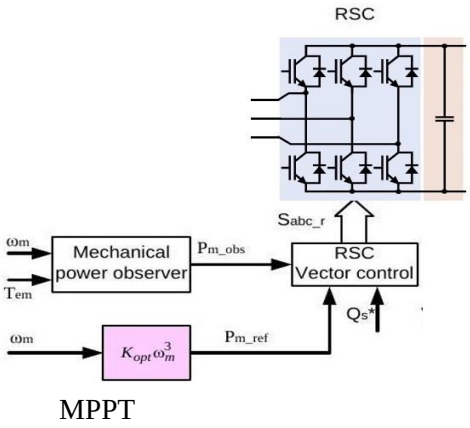

Figure 2-11 Sensorless MPPT control

2.6 Pitch control

The blade orientation system plays a crucial role in regulating the generated power. With this system, the blades are maneuvered by a control device known as the "Pitch control." By adjusting the angle of the blade orientation, we can alter the turbine's performance, specifically the power coefficient, as illustrated in Figure 2-12 Blade orientation. At low wind speeds, the blades face the wind directly, while at higher speeds, they tilt to reduce the power coefficient [54] [7].

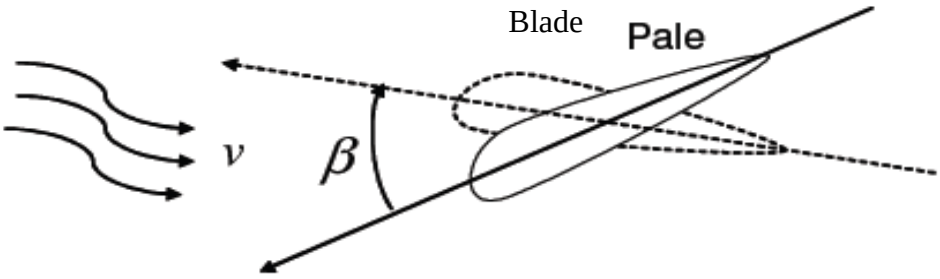

Figure 2-12 Blade orientation

This method involves controlling the electrical power using an open-loop PI regulator, as depicted in the figure below.

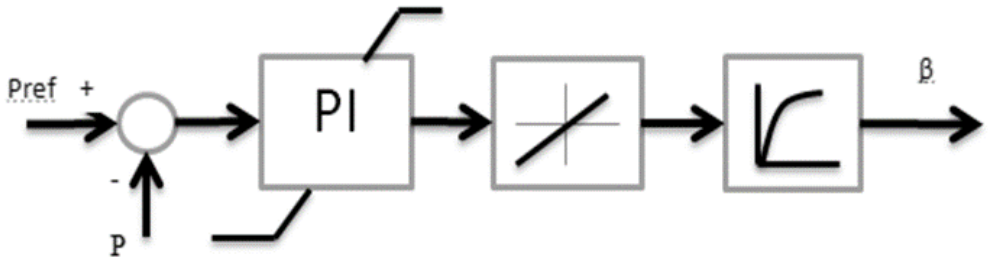

Figure 2-13 Pitch control

2.7 Simulation results

The simulation results corresponding to this control algorithm show that the variations of the power produced are adapted to the variation of the wind speed. (Figure 2-14). To validate the angle regulation system, we applied to the turbine a variable wind profile of around 8.5m/s, (Figure 2-15).

This is the full load zone of the wind turbine, the turbine is driven, under the action of the wind, at a speed that we have limited to this nominal speed (zone 2) and it provides mechanical power that we must keep equal to its rated power.

In Figure 2-16 , in zone 2, the angle of orientation of the blade undergoes a slight increase to limit the power generated.

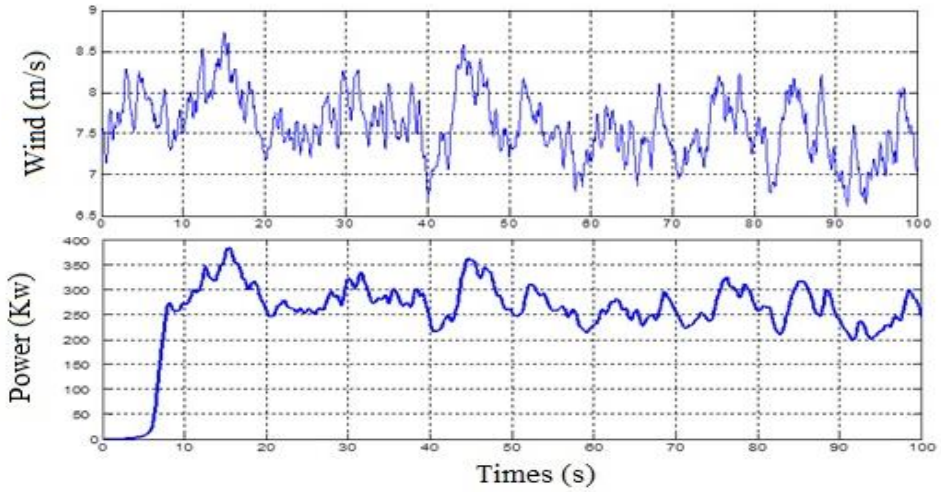

Figure 2-14 Wind profile applied to the wind turbine with the power produced in Zone1

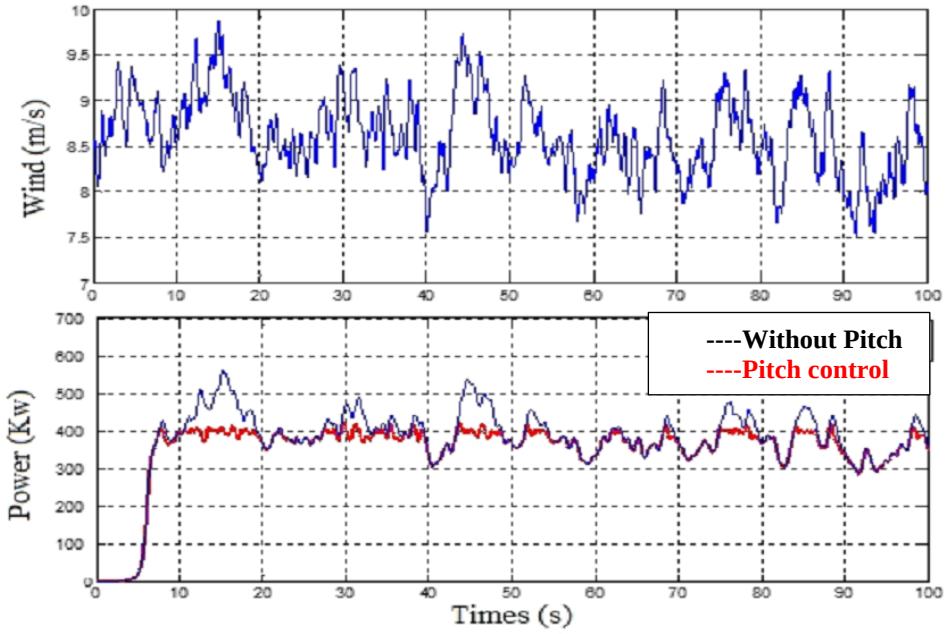

Figure 2-15 Wind Profile Applied to the Wind Turbine with Power Output in Zone2

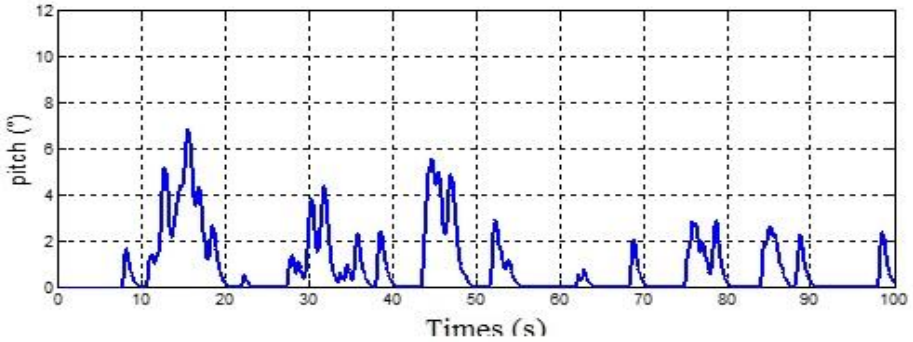

Figure 2-16 Pitch Angle in Zone 2

2.8 Conclusion

In this chapter, we have investigated the behavior of the wind turbine under varying wind speeds, delineating the operating zones of the turbine based on velocity and outlining the method for extracting maximum power within each zone.

The MPPT method is employed in the first operating zone to extract *m*aximum power based on optimal *Cp* and optimal λ.In the second zone, we have described a controller enabling adjustment of the angle to limit power output when wind speeds become excessive.

We conducted simulations of the wind turbine using MATLAB/Simulink. The results demonstrate that the turbine's mechanical speed and electromagnetic torque closely track the reference values, while maintaining an optimal power coefficient (*Cp-optimal* = 0.48) and an optimal tip speed ratio (λ*-optimal = 8.1*).

.

3 Modeling and control of the grid-side system

3.1 Introduction

Given that the machine must operate in either sub-synchronous or super-synchronous speed modes depending on different driving speeds, the configuration of AC/DC/AC converters becomes necessary due to their bidirectional operation capability. The power electronics equipment consists of two identical AC/DC converters connected in cascade via a DC link associated with a capacitor. As presented in the previous chapter, the control of the rotor-side converter of the Doubly-Fed Induction Generator (DFIG) aims to regulate the machine's stator powers. In contrast, the main objective of the grid-side converter is to control the DC link voltage and the power factor on the grid side. Therefore, in this chapter, the converter is considered bidirectional since it functions as both a PWM rectifier and a PWM inverter, depending on the direction of power flow exchanged with the grid.

The model of the three-phase converter, controlled by vector PWM, is established in the *abc* reference frame and then transformed into the synchronous *dq* reference frame to simplify the design of PI controllers. This approach is similar to the control applied to the DFIG to establish the regulation of active and reactive powers exchanged with the grid on the rotor side of the DFIG.

3.2 Modeling of the Back-Back Converter

The electronic conversion chain can be viewed as consisting of two inverters connected via a common DC bus (back-to-back converter AC/DC/AC). To begin, a generic model of an inverter is introduced, and then it is adapted to represent the specific notations used for both inverters in the system. In general, the inverter performs two key functions: converting three-phase alternating currents into direct current (AC to DC), and converting direct voltage into alternating three-phase voltages (DC to AC).

The converter under consideration is bidirectional, meaning it can handle current flow in both directions. It typically consists of three switching cells, each made up of two Insulated Gate Bipolar Transistors (IGBTs) connected to two antiparallel diodes. For the purposes of this analysis, the semiconductors are assumed to be ideal, meaning no losses and instantaneous switching. This leads to the assumption of continuous conduction

mode, where the converter can be considered an ideal switch with no losses [7]. The basic configuration of the back *to* back converter is shown in Figure 3-1.

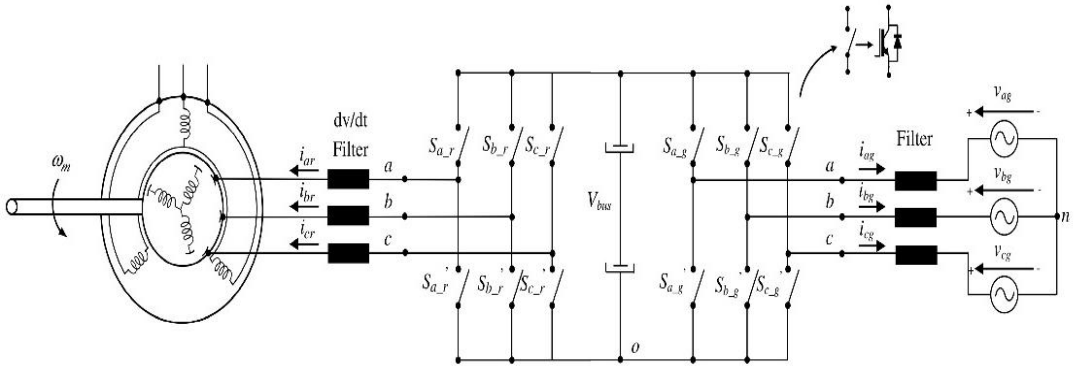

Figure 3-1 The Back-Back Converter

The three-phase converter found in a Rotor-Side (RSC) or Grid-Side (GSC) is depicted using bidirectional switches. These IGBT are presented as switches can be controlled in opening '1' and closing '0', and the voltage U_s is determined by the configuration of these switches. The converter input voltages are:

$$\begin{cases} u_{sab} = (S_a - S_b)V_{bus} \\ u_{sbc} = (S_b - S_c)V_{bus} \\ u_{sca} = (S_c - S_a)V_{bus} \end{cases} \quad (3\text{-}1)$$

With S_i are the state of the switches: $S_i = \begin{cases} 1 & \text{switche ON} \\ 0 & \text{switche OFF} \end{cases}$

From which we can deduce the simple voltages :

$$\begin{cases} u_{sa} = f_a V_{bus} \\ u_{sb} = f_b V_{bus} \\ u_{sc} = f_c V_{bus} \end{cases} \quad (3\text{-}2)$$

With *:*

$$\begin{cases} f_a = S_a - \frac{1}{3}(S_a + S_b + S_c) \\ f_b = S_b - \frac{1}{3}(S_a + S_b + S_c) \\ f_c = S_c - \frac{1}{3}(S_a + S_b + S_c) \end{cases} \quad (3\text{-}3)$$

Table 2 delineates the eight possible output AC voltage configurations corresponding to the allowable switching states of (S_a, S_b, S_c) [7],[12]:

Table2 Different output voltage combination

S_a	S_b	S_c	v_{ao}	v_{bo}	v_{co}	v_{an}	v_{bn}	v_{cn}
0	0	0	0	0	0	0	0	0
0	0	1	0	0	V_{bus}	$-\frac{V_{bus}}{3}$	$-\frac{V_{bus}}{3}$	$2\cdot\frac{V_{bus}}{3}$
0	1	0	0	V_{bus}	0	$-\frac{V_{bus}}{3}$	$2\cdot\frac{V_{bus}}{3}$	$-\frac{V_{bus}}{3}$
0	1	1	0	V_{bus}	V_{bus}	$-2\cdot\frac{V_{bus}}{3}$	$\frac{V_{bus}}{3}$	$\frac{V_{bus}}{3}$
1	0	0	V_{bus}	0	0	$2\cdot\frac{V_{bus}}{3}$	$-\frac{V_{bus}}{3}$	$-\frac{V_{bus}}{3}$
1	0	1	V_{bus}	0	V_{bus}	$\frac{V_{bus}}{3}$	$-2\cdot\frac{V_{bus}}{3}$	$\frac{V_{bus}}{3}$
1	1	0	V_{bus}	V_{bus}	0	$\frac{V_{bus}}{3}$	$\frac{V_{bus}}{3}$	$-2\cdot\frac{V_{bus}}{3}$
1	1	1	V_{bus}	V_{bus}	V_{bus}	0	0	0

3.3 Filter model

In the subsequent stage, attention is directed towards the filter, situated between the grid and the converter. It's important to highlight that the main objective of this filter is to alleviate the current and voltage harmonics produced by the converter's switching actions. The three-phase equivalent circuit of this filter is depicted in Figure 3-2. Moreover, the inductance (L_f) is accompanied by an inherent resistance (R_f), both of which are integrated into the model [12].

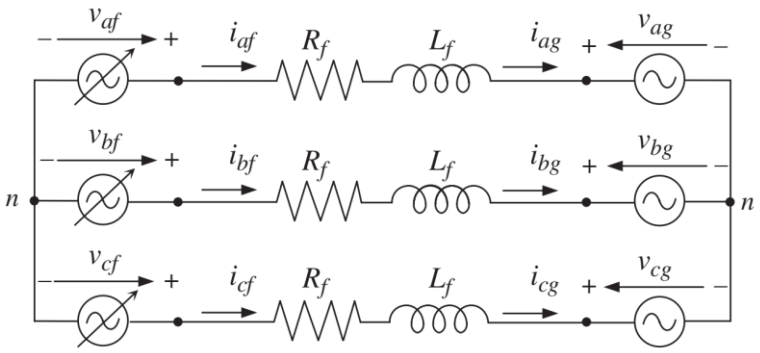

Figure 3-2 The grid system with filter

In this configuration , both the grid-side currents (i_g) and converter output currents (i*f*) are indistinguishable. Hence, the subsequent *m*athematical expressions can be formulated using either of these currents. However, for consistency, the grid-side current (*ig*) is utilized in the mathematical expressions:

$$\begin{cases} v_{af} = R_f \cdot i_{ag} + L_f \cdot \frac{di_{ag}}{dt} + v_{ag} \\ v_{bf} = R_f \cdot i_{bg} + L_f \cdot \frac{di_{bg}}{dt} + v_{bg} \\ v_{cf} = R_f \cdot i_{cg} + L_f \cdot \frac{di_{cg}}{dt} + v_{cg} \end{cases} \quad (3\text{-}4)$$

Were:

- L_f *Inductance of the filter* (H)
- R_f *Resistive part of the filter* (Ω)
- v_{af}, v_{bf}, v_{cf} *Output voltages referred to the neutral point of the load* $n(V)$
- i_{af}, i_{bf}, i_{cf} *Output currents* (A)
- v_{ag}, v_{bg}, v_{cg} *Grid voltages* (V)
- i_{ag}, i_{bg}, i_{cg} *Currents flowing through the grid side of the filter* (A)

To model effectively, it is important to isolate the first derivative of the currents:

$$\begin{cases} \frac{di_{ag}}{dt} = \frac{1}{L_f} \cdot \left(v_{af} - R_f \cdot i_{ag} - v_{ag}\right) \\ \frac{di_{bg}}{dt} = \frac{1}{L_f} \cdot \left(v_{bf} - R_f \cdot i_{bg} - v_{bg}\right) \\ \frac{di_{cg}}{dt} = \frac{1}{L_f} \cdot \left(v_{cf} - R_f \cdot i_{cg} - v_{cg}\right) \end{cases} \quad (3\text{-}5)$$

Therefore, the model of the GSC and the inductive filter, is illustrated in *Figure 3-4*.

3.4 DC bus model

The DC bus of the power converter holds energy within the capacitor. Illustrated in Figure 3-3 is a model representing the DC bus, which includes a resistor R_{bus} in parallel with the capacitor . Typically, R_{bus} has a high resistance value [7].

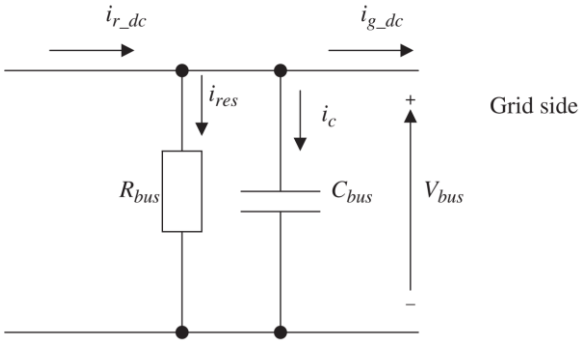

Figure 3-3 DC bus system

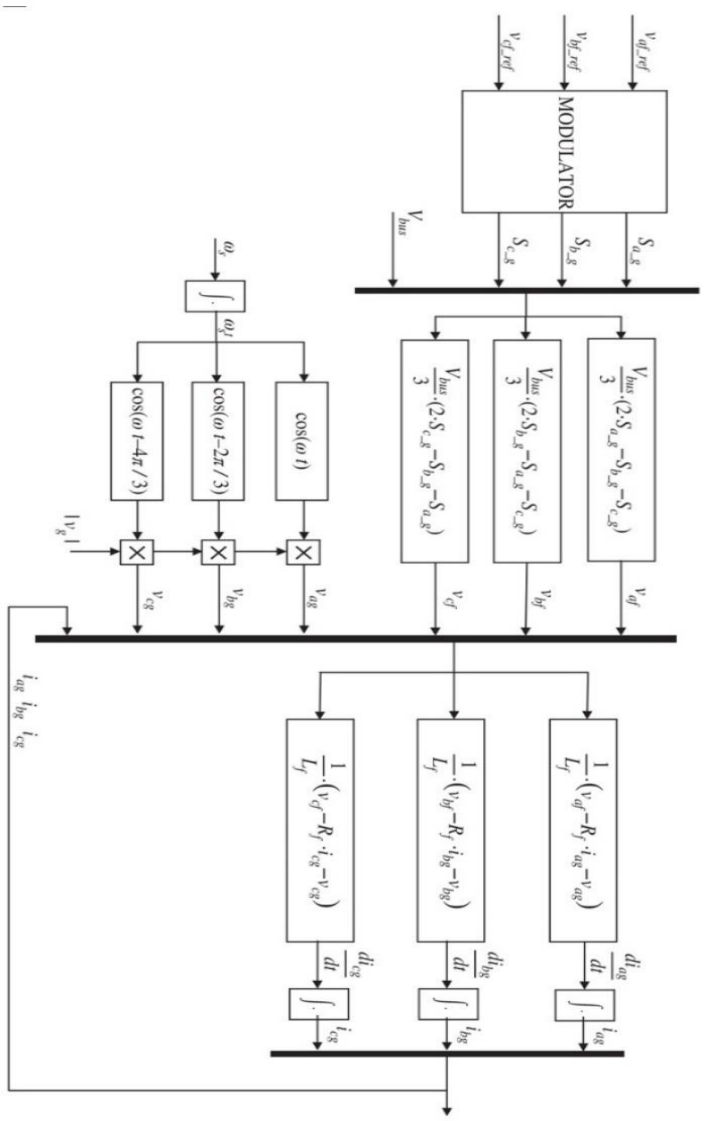

Figure 3-4 the model of the grid-side converter [12]

The time evolution of the DC bus voltage is derived from the integration of the current flowing through the capacitor:

$$V_{bus} = \frac{1}{C_{bus}} \cdot \int \ i_c \cdot dt \qquad (3\text{-}6)$$

The current passing through the capacitor can be determined as:

$$i_c = i_{r\_dc} - i_{g\_dc} - i_{res} \qquad (3\text{-}7)$$

The DC current can also be derived from the output AC currents of the converter through the following relationship::

$$i_{g\_dc} = S_{a\_g} \cdot i_{af} + S_{b\_g} \cdot i_{bf} + S_{c\_g} \cdot i_{cf} \quad (3\text{-}8)$$

Meanwhile, the current passing through the resistance:

$$i_{res} = \frac{V_{bus}}{R_{bus}} \quad (3\text{-}9)$$

Hence, the Figure 3-5 illustrates the model of the DC bus system, incorporating all these equations[12].

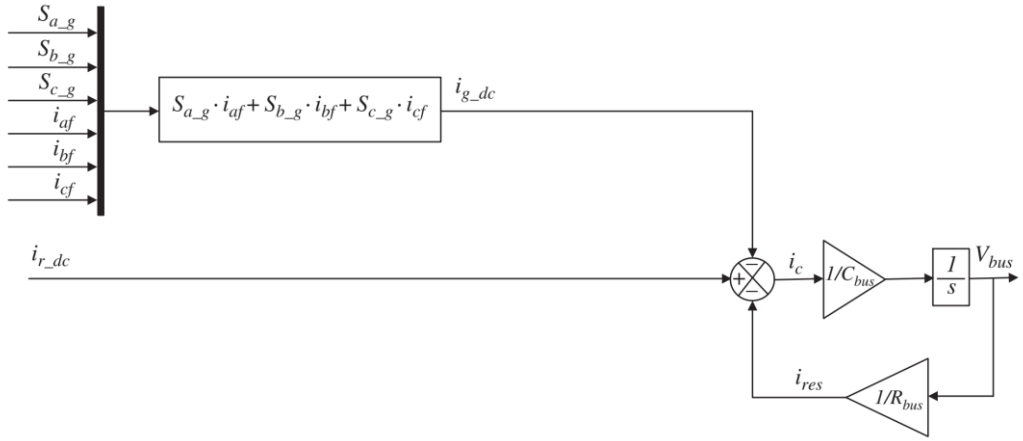

Figure 3-5 DC bus model

3.5 Dynamic model equations

In this section, we derive dynamic mathematical expressions for this filter in both stationary and synchronous reference frames. The voltage equations in the stationary $\alpha\beta$ reference frame are obtained via the Clarke transformation [12]:

$$\begin{cases} v_{\alpha f} = R_f \cdot i_{\alpha g} + L_f \cdot \frac{di_{\alpha g}}{dt} + v_{\alpha g} \\ v_{\beta f} = R_f \cdot i_{\beta g} + L_f \cdot \frac{di_{\beta g}}{dt} + v_{\beta g} \end{cases} \quad (3\text{-}10)$$

The equations in the rotating *d-q* frame are obtained through the Park transformation:

$$\begin{cases} v_{df} = R_f \cdot i_{dg} + L_f \cdot \frac{di_{dg}}{dt} + v_{dg} - \omega_a \cdot L_f \cdot i_{qg} \\ v_{qf} = R_f \cdot i_{qg} + L_f \cdot \frac{di_{qg}}{dt} + v_{qg} + \omega_a \cdot L_f \cdot i_{dg} \end{cases} \quad (3\text{-}11)$$

3.6 Control of grid-side converter

The vector control approach for this converter typically begins with the system modeled in synchronous reference frames (*dq*) [7],[12]. To simplify equation (3-11)

further, the space vector of *t*he grid voltage v_g is usually aligned with the *d-axis*, as illustrated in Figure 3-6. Therefore, the resulting grid voltages are:

$$\begin{cases} v_{dg} = |\vec{v}_g| \\ v_{qg} = 0 \end{cases} \quad (3\text{-}12)$$

The synchronous rotating angular speed of the reference frame equals the angular speed of the grid voltages.

$$\theta = \omega_a \cdot t \Rightarrow \theta = \theta_g = \omega \cdot t \quad (3\text{-}13)$$

Hence, equations (3-11) are reduced to:

$$\begin{cases} v_{df} = R_f \cdot i_{dg} + L_f \cdot \frac{di_{dg}}{dt} + v_{dg} - \omega \cdot L_f \cdot i_{qg} \\ v_{qf} = R_f \cdot i_{qg} + L_f \cdot \frac{di_{qg}}{dt} + \omega \cdot L_f \cdot i_{dg} \end{cases} \quad (3\text{-}14)$$

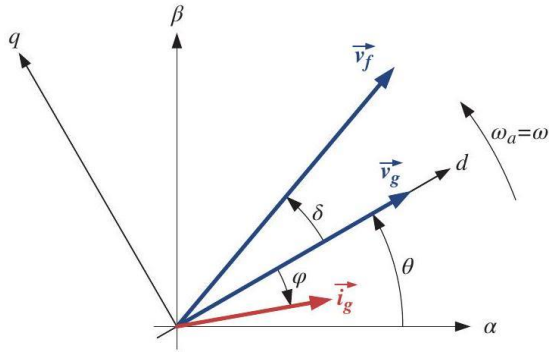

Figure 3-6 Alignment with the d axis of the grid voltage space vector

This alignment of the grid voltage also simplifies the computation of active and reactive power. Therefore, we calculate the active and reactive powers exchanged with the grid:

$$\begin{cases} P_g = \frac{3}{2} Re\{\vec{v}_g \cdot \vec{i}_g^*\} = \frac{3}{2}(v_{dg} \cdot i_{dg} + v_{qg} \cdot i_{qg}) \\ Q_g = \frac{3}{2} Im\{\vec{v}_g \cdot \vec{i}_g^*\} = \frac{3}{2}(v_{qg} \cdot i_{dg} - v_{dg} \cdot i_{qg}) \end{cases} \quad (3\text{-}15)$$

Taking into account equations (3-12) and (3-13), the power calculation can be simplified as follows:

$$\begin{cases} P_g = \frac{3}{2} \cdot v_{dg} \cdot i_{dg} = \frac{3}{2} \cdot |\vec{v}_g| \cdot i_{dg} \\ Q_g = -\frac{3}{2} \cdot v_{dg} \cdot i_{qg} = -\frac{3}{2} \cdot |\vec{v}_g| \cdot i_{qg} \end{cases} \quad (3\text{-}16)$$

3.6.1 Vector control strategy

The vector control strategy in the GSC primarily regulates the DC bus voltage (V_{bus}) and manages the exchange of reactive power with the grid (Q_g), as shown in Figure 3-7. Typically, the reference value for reactive power is set to zero VAR, facilitating current exchange with a unity power factor at the grid voltage terminals. However, in certain applications, operating with non-zero reactive power values may be required [12].

Figure 3-8 illustrates a vector control block diagram. It generates pulses for the controlled switches S_{a_g}, S_{b_g}, and S_{c_g} from the V_{bus} and Q_g references. Furthermore, the PI regulator associated with the DC bus voltage reference generates the active power reference value $(P_g{}^*)$, which is subsequently converted into the d-component of the grid current reference $(i_{dg}{}^*)$.

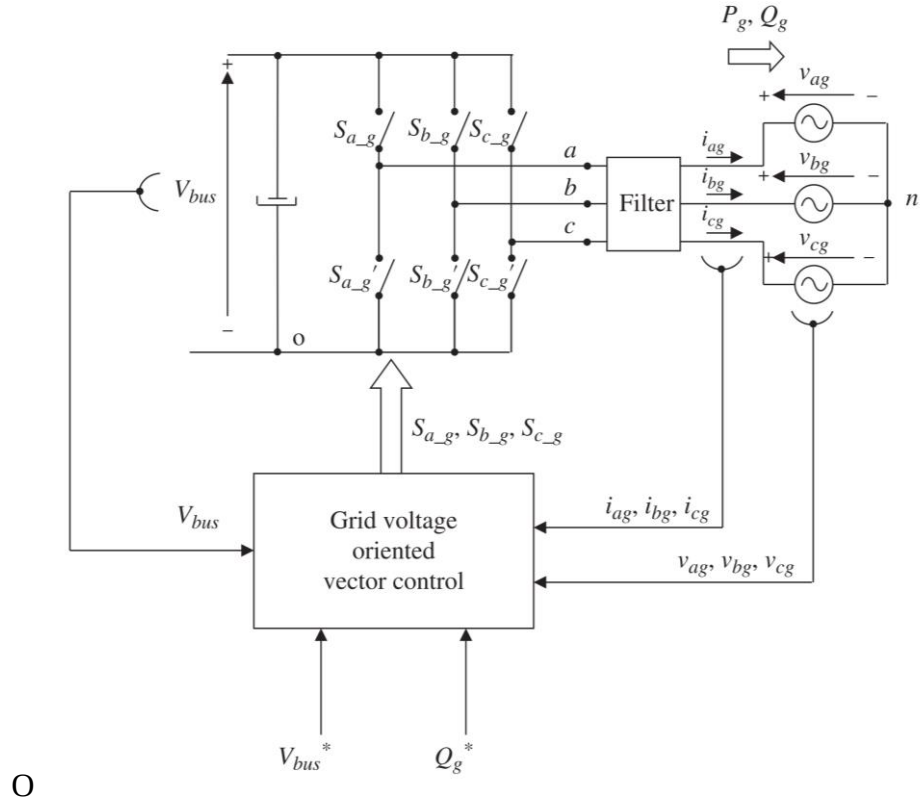

O

Figure 3-7 GSC control

Alternatively, the grid current reference $(i_{qg}{}^{*})$ is generated from the reactive power reference value $(Q_g{}^{*})$. The constant terms required for transforming from powers to dq current reference components can be straightforwardly deduced from equation (3-16):

$$\begin{cases} K_{Pg} = \frac{1}{\frac{3}{2}\cdot v_{dg}} \\ K_{Qg} = \frac{1}{-\frac{3}{2}\cdot v_{dg}} \end{cases} \quad (3\text{-}17)$$

Following this, the current reference undergoes processing by their respective PI regulators. It's important to highlight that the cancellation of coupling terms also occurs at the output of the current PI regulators. The terms utilized for this cancellation can be deduced from equation (3-14) .

$$\begin{cases} e_{df} = -\omega \cdot L_f \cdot i_{qg} + v_{dg} \\ e_{qf} = \omega \cdot L_f \cdot i_{dg} \end{cases} \quad (3\text{-}18)$$

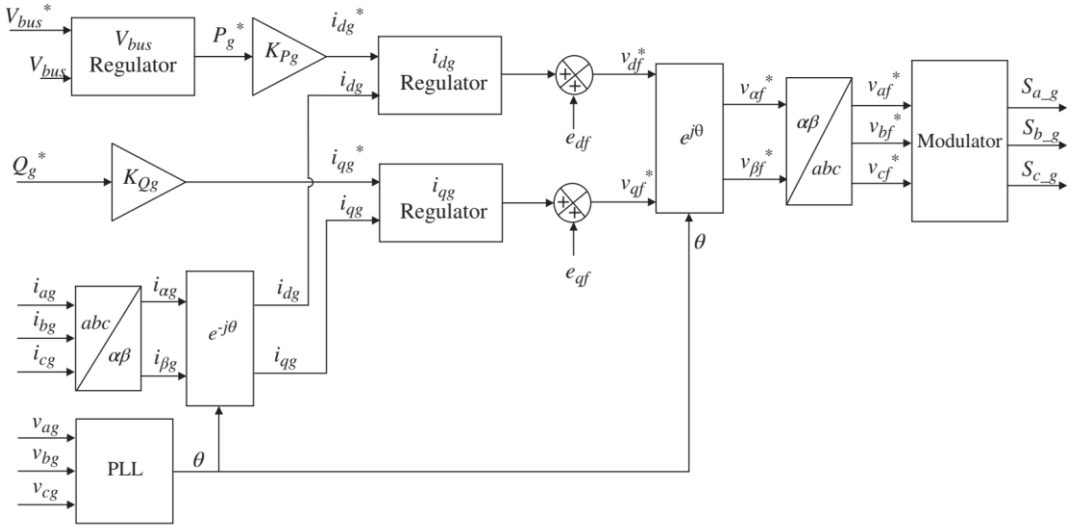

Figure 3-8 Vector Control block diagram

Ultimately, the modulator transforms these voltage references into commands for the IGBTs of the converter. A modulation strategy commonly used is sinusoidal PWM, for example. For voltage and current coordinate transformations, θ represents the angle of the grid voltage, Typically, this angle is estimated using a phase-locked loop (PLL).

3.6.2 Optimization of the Current Regulators

Eliminating the coupling terms as achieved in voltage expression (3-14) , we derive the current-voltage equations of the electrical model in open loop.

$$\begin{cases} v_{df} = R_f \cdot i_{dg} + L_f \cdot \frac{di_{dg}}{dt} \\ v_{qf} = R_f \cdot i_{qg} + L_f \cdot \frac{di_{qg}}{dt} \end{cases} \quad (3\text{-}19)$$

The following transfer functions are derived from applying the Laplace transformation:

$$\frac{i_{dg}(s)}{v_{df}(s)} = \frac{1}{L_f s + R_f} \quad (3\text{-}20)$$

$$\frac{i_{qg}(s)}{v_{qf}(s)} = \frac{1}{L_f s + R_f} \quad (3\text{-}21)$$

Hence, this concept can be depicted in block diagrams, as shown in Figure 3-9. In this approach, an idealized control strategy is assumed, neglecting factors such as converter delays, measurement delays, converter nonlinearities, harmonic presence, etc. It's important to note that the current control loops utilize an idealized PI regulator[7],[12].

As a result, the current closed loops can be ideally characterized by the following transfer functions:

$$\begin{cases} \frac{i_{ds}(s)}{i_{ds}{}^*(s)} = \frac{sk_p + k_i}{s^2(L_f) + s(R_f + k_p) + k_i} \\ \frac{i_{qs}(s)}{i_{qs}{}^*(s)} = \frac{sk_p + k_i}{s^2(L_f) + s(R_f + k_p) + k_i} \end{cases} \quad (3\text{-}22)$$

With these expressions for the closed-loop currents, it becomes feasible to adjust the gains of PI regulators. By equating the denominators of these derived transfer functions to the standard second-order denominator of classic control theories, we can obtain the desired values.

$$s^2(L_f) + s(R_f + k_p) + k_i = s^2 + 2\xi\omega_n s + \omega_n^2 \quad (3\text{-}23)$$

Consequently, the values for k_p and k_i are:

$$\begin{cases} k_i = L_f \omega_n^2 \\ k_p = L_f 2\xi\omega_n - R_f \end{cases} \quad (3\text{-}24)$$

And ω_n and ξ values can be chosen by any of the *pole placement methods.*

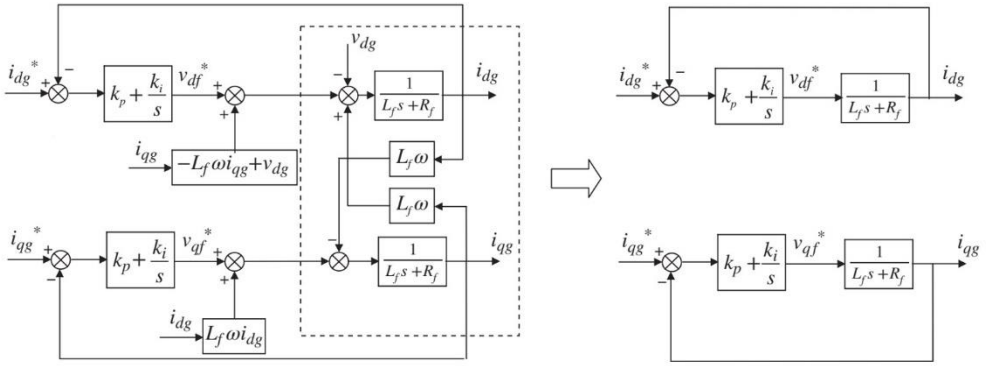

Figure 3-9 Current loops structure

3.7 Pulse Generation of the Controlled Switches

The commands for the controlled semiconductors of the two-level converter can be generated using various modulation techniques, collectively known as "Modulation." This section outlines some of the most commonly used modulation techniques [13]-[15]:

1. Sinusoidal pulse width modulation (PWM) technique
2. Space vector modulation (SVM) technique

3.7.1 Sinusoidal Pulse Width Modulation (PWM)

This modulation method is commonly employed in voltage sourced converters. It entails comparing a triangular signal with the reference signal, which represents the desired output voltage of the converter. Triangular-sinusoidal modulation combines a low-frequency sinusoidal modulating wave, known as the reference voltage, with a high-frequency triangular carrier wave. This technique, also called Sinusoidal Pulse Width Modulation (PWM) *[15]*, determines the switching of power circuit switches based on the comparison of these two signals. Subsequently, the output voltage is generated according to the following law:

$$S_j = 1 \text{ if } v_j^* > v_{tri} \text{ with } j = a, b, c \qquad (3\text{-}25)$$

Where v_a^*, v_b^*, v_c^* reference voltages for each phase, v_{tri} = triangular signal.

To establish the connections between the amplitudes and frequencies of the signals, the following indices are needed[15]:

1.***Frequency Modulation Index*** $(\boldsymbol{m_f})$***:*** The relationship between the frequency of the triangular signal and the reference signal can be described as:

$$m_f = \frac{f_{tri}}{f_{ref}} \tag{3-26}$$

Typically, to attain a high-quality output voltage, a large value for mf is desirable. However, since the frequency of the triangular signal (f_{tri}) determines the switching frequency of the converter's switches, it's crucial not to set this frequency too high to avoid excessive switching losses in the semiconductors. Therefore, when choosing a value for m_f, it's essential to strike a balance between voltage quality and power losses in the converter.

2.**Amplitude Modulation Index** ***($\boldsymbol{m_a}$):*** This index relates the amplitude of the sinusoidal reference wave ($|\boldsymbol{v}^*|$) to the peak-to-peak amplitude ***($\boldsymbol{v_{tri}}$)*** of the triangular signal. It is calculated as:

$$m_a = \frac{|v^*|}{|v_{tri}|} \tag{3-27}$$

The output voltages obtained through this PWM method are illustrated in Figure 3-10, accompanied by the schematic block diagram for implementation shown in Figure 3-11. It's important to highlight that the maximum achievable fundamental voltage without over-modulation $(m_a \leq 1)$ is $V_{bus}/2$. As previously observed, the output voltages v_{ao}, v_{bo}, and v_{co} are constrained to only two distinct voltage levels V_{bus} and 0.

3.7.2 Space Vector Modulation (SVM)

SVM relies on representing a single- or three-phase circuit in a stationary rectangular coordinate system using space vector theory[15]. The reference $\underline{U_{\text{ref}}} = U_\alpha + jU_\beta$ is characterized by both its magnitude and angle.

$$U_{ref} = \sqrt{u_{\alpha,ref}^2 + u_{\beta,ref}^2},\ \varphi_m = arctan\ \frac{u_{\alpha,ref}}{u_{\beta,ref}} \tag{3-28}$$

In a stationary rectangular coordinate system, $u_{\alpha,\text{ ref}}$ and $u_{\beta,\text{ ref}}$ represent the α and β components of U_{ref}. For determining the duration of the converter's switching states, the modulation index plays a crucial role, as it's directly linked to the SV length relative to the DC-link voltage. Typically, *M* is defined as:

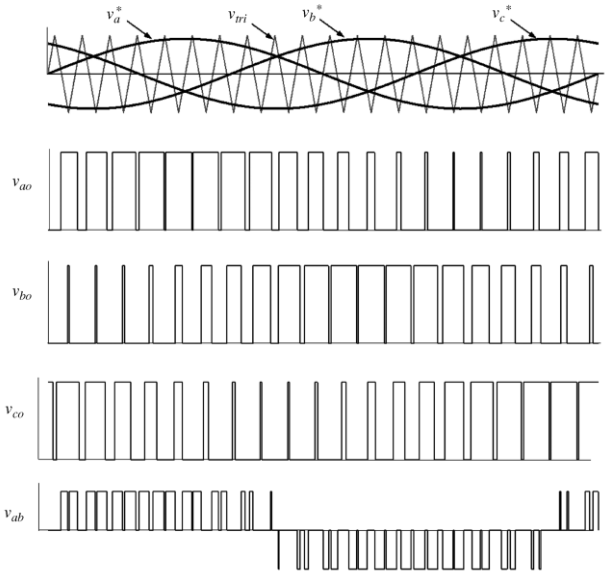

Figure 3-10 Output voltages of converter with sinusoidal PWM [7]

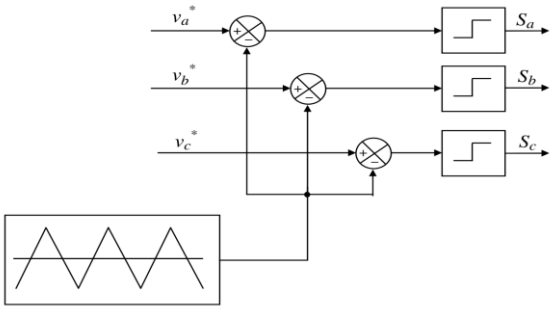

Figure 3-11 block diagram of the sinusoidal PWM [7]

$$M = \frac{\pi U_{ref}}{2U_{DC}}(n-1) \qquad (3\text{-}29)$$

The parameter n represents the number of converter output phase voltage levels. In the linear operational range, the permissible length of vector U_{ref} for each φ_{m} angle is determined by $U_{\mathrm{ref}} = \frac{U_{\mathrm{DC}}}{\sqrt{3}}$. Hence, the linear modulation range of an *n*-level converter is constrained to:

$$M = 0.907(n-1) \qquad (3\text{-}30)$$

which is the maximal converter linear range of operation [13],[14].

In SVM, due to the symmetry of the three-phase system, the Clarke transformation can be employed to convert coordinates from the natural abc system to a stationary $\alpha\beta$ system. Figure 3-12(a) depicts the SV αβ voltage plane, showcasing the potential output voltage

vectors of a three-phase two-level converter. Each voltage vector is denoted by three digits representing the switching states in legs a, b, and c, respectively. The converter offers eight switching states, comprising six active (100, 110, 010, 011, 001, and 101) and two zero states (000 and 111). These active vectors partition the plane into six sectors, where the reference vector U_{ref} is derived by appropriately activating two adjacent vectors. Vector U_{ref} (as shown in Figure 3-12(b)) can be realized using different ON/OFF switch sequences of V_1 and V_2, whereas zero vectors V_0 and V_7 diminish the modulation index. The reference vector U_{ref}, utilized in solving equations that describe the durations $T1$, T_2, T_0, and T_7, is sampled at a fixed sampling frequency $f_S = 1/T_S$. The digital implementation is elucidated using a basic trigonometric relationship for the first sector and is recalculated for the following sectors (from 2 to 6).

$$T_1 = \frac{2\sqrt{3}}{\pi} M T_S sin\left(\frac{\pi}{3} - \varphi_m\right),\ T_2 = \frac{2\sqrt{3}}{\pi} M T_S sin\ \varphi_m \qquad (3\text{-}31)$$

After calculating T_1 and T_2, the remaining sampling time is allocated for zero vectors V_0 and V_7 under the condition $T_1+T_2 < T_S$. Equation (3-31) remains the same for all variants of SVM. The only distinction lies in the placement of zero vectors V_0 (000) and V_7 (111). This results in different equations defining T_0 and T_7 for each method, but the total duration of the zero vectors must satisfy the following conditions:

$$T_S - T_1 - T_2 = T_0 + T_7 \qquad (3\text{-}32)$$

The most popular SVM method is Symmetrical Space Vector Pulse Width Modulation (SVPWM), in which:

$$T_0 = T_7 = \frac{T_S - T_1 - T_2}{2} \qquad (3\text{-}33)$$

Figure 3-13 illustrates the gate pulses and the relationship between the ON time (T_{ON}) and the duration of vectors V_1, V_2, V_0, and V_7. For the first sector, the commutation delay can be calculated as:

$$\begin{cases} T_{a,ON} = \frac{T_0}{2} \\ T_{b,ON} = \frac{T_0}{2} \\ T_{c,On} = \frac{T_0}{2} + T_1 + T_2 \end{cases} \qquad (3\text{-}34)$$

In classical SVM, times T_1, T_2, and T_0 are computed for a single sector. The commutation delay for other sectors can be calculated using a matrix :

$$\begin{bmatrix} T_{a,\mathrm{ON}} \\ T_{b,\mathrm{ON}} \\ T_{c,\mathrm{ON}} \end{bmatrix} = \left[\begin{array}{c|c|c|c|c|c} \text{Sector 1} & \text{Sector 2} & \text{Sector 3} & \text{Sector 4} & \text{Sector 5} & \text{Sector 6} \\ 1\ 0\ 0 & 1\ 0\ 1 & 1\ 1\ 1 & 1\ 1\ 1 & 1\ 1\ 0 & 1\ 0\ 0 \\ 1\ 1\ 0 & 1\ 1\ 0 & 1\ 0\ 0 & 1\ 0\ 1 & 1\ 1\ 1 & 1\ 1\ 1 \\ 1\ 1\ 1 & 1\ 1\ 1 & 1\ 1\ 0 & 1\ 0\ 0 & 1\ 0\ 0 & 1\ 0\ 1 \end{array}\right] \begin{bmatrix} 0.5T_0 \\ T_1 \\ T_2 \end{bmatrix} \quad (3\text{-}35)$$

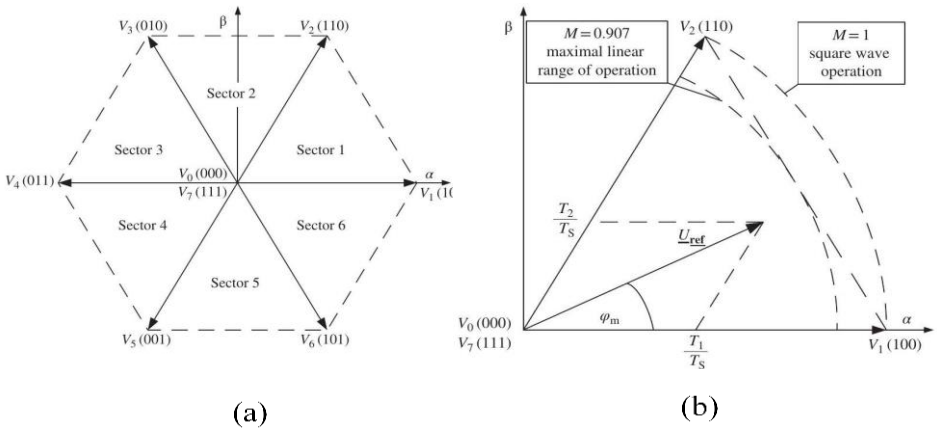

Figure 3-12 Space vector representation of three-phase two-level converter

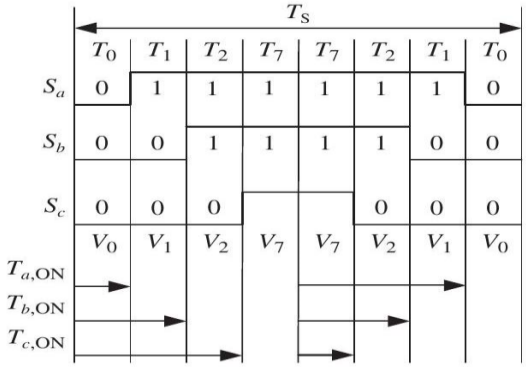

Figure 3-13 Vector placement in sampling time for three-phase SVM

. To conclude, the simplified block diagram of Figure 3-14 illustrates the implementation schema of the SVM.

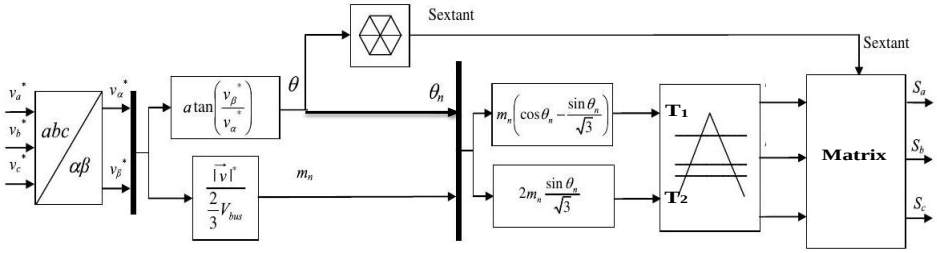

Figure 3-14 Simplified block diagram of the SVM schema

3.8 Simulation results

A rotor-side converter was simulated in MATLAB/Simulink, where the three legs of the inverter are composed of IGBT/Diode electronic switches. These legs are powered by a DC source with V_{dc} = 1200V. The opening and closing of the switches are controlled by a SVM strategy, which generates control signals enabling the inverter to produce a modulated voltage.

The figure shows the signal generated by the vector control and the pulse generated by comparing this signal with a triangular waveform at a switching frequency of f=5000 Hz. The phase voltages are depicted in Figure 3-16, where we observe the phase-to-phase voltage V_{ab}=1200 V

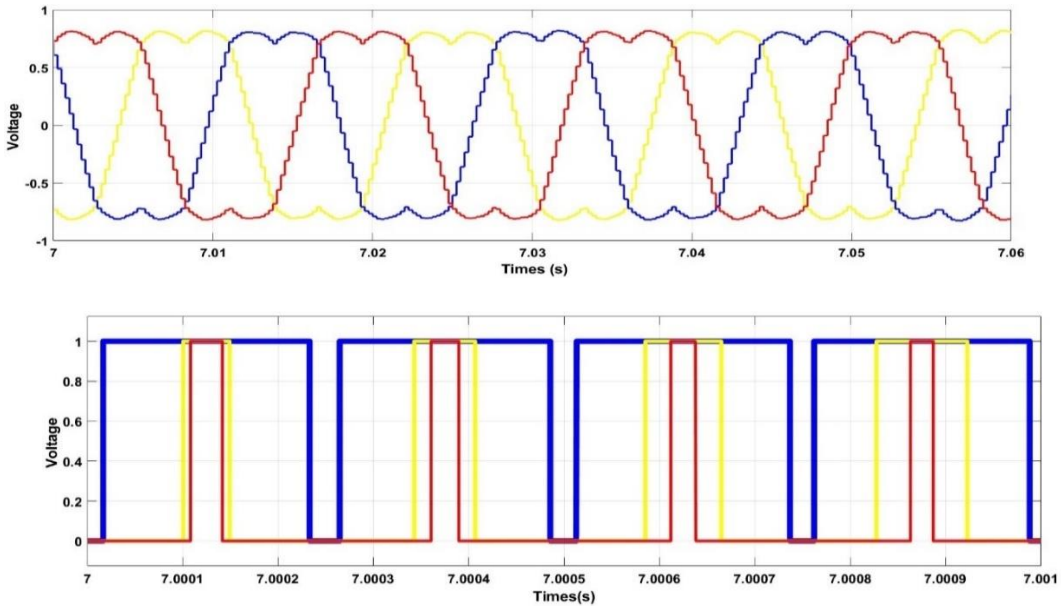

Figure 3-15 signals generated by the SVM

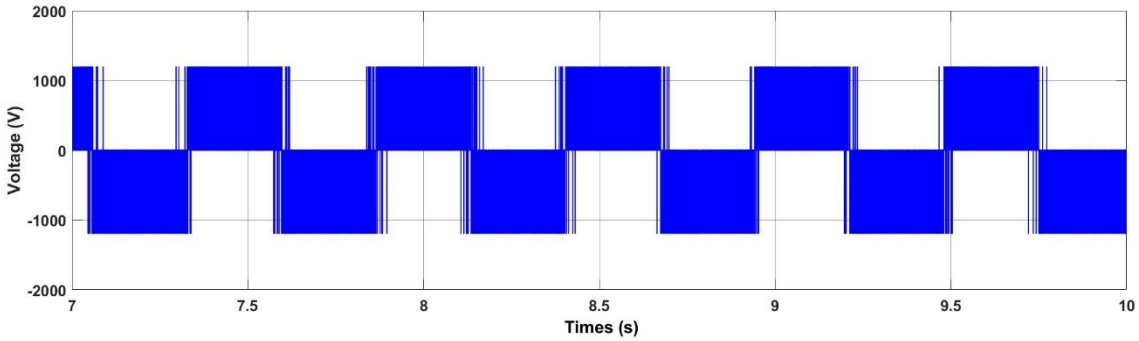

Figure 3-16 The phase voltage

To test the performance of the proposed regulation on the grid-side converter, we applied a step change to the reference of the DC link voltage, from 900V to 1200V at time t = 5s. Figure 3-17 illustrates the excellent tracking of the DC voltage to its reference with negligible delay and overshoot. Similarly, we observe the same behavior for the direct voltage component *dq* in Figure 3-18

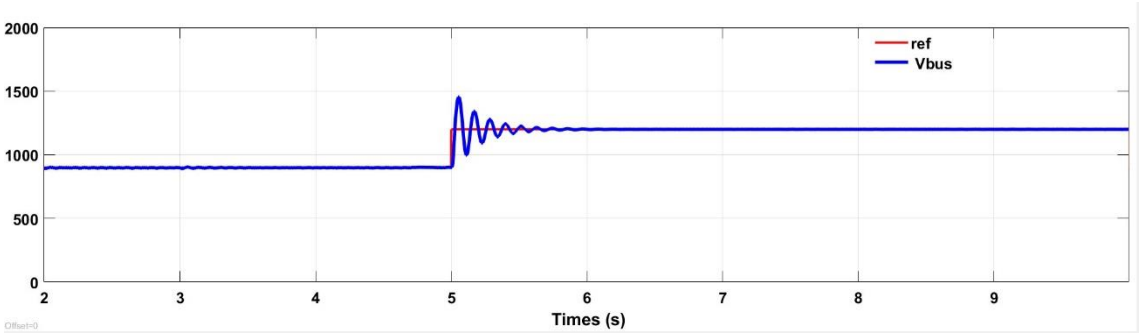

Figure 3-17 DC link voltage

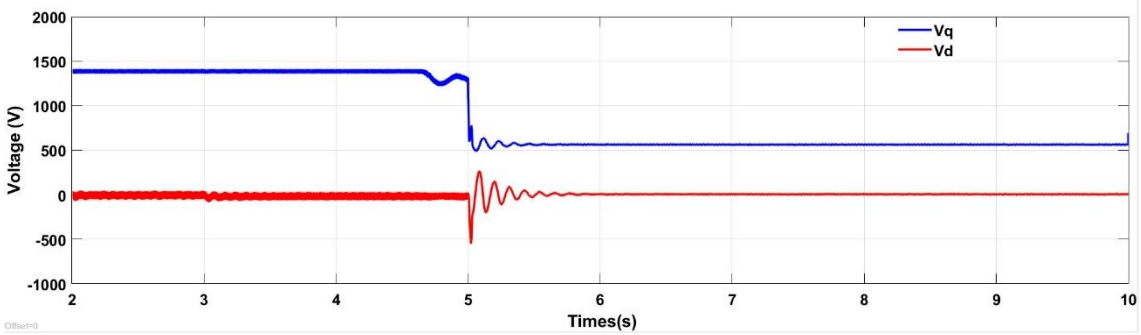

Figure 3-18 Direct voltage component

3.9 Conclusion

This chapter was dedicated to the study of power electronics converters and the most commonly used control strategies in this field. First, we presented the basic topology, operating principles, and modeling. Following this, we discussed the control of the grid-side converter, which was based on grid voltage orientation. Using the Park transformation, voltages and currents became continuous quantities in the dq reference frame. Therefore, PI controllers were employed to regulate the DC link voltage and the power factor on the grid side of the converter.

At a fixed switching frequency, several simulation tests were conducted on both converters using MATLAB software. The results demonstrate good dynamic performance in response to step changes for the DC link.

4 DFIG and Independent Power Control

4.1 Introduction

Among the various variable-speed wind turbine technologies, DFIG has garnered significant interest over the past two decades. This machine offers the advantage of high energy transfer capacity while reducing the size of power converters to one-third of the nominal power of the wind system. While the DFIG's stator is directly connected to the grid, the rotor is connected via two back-to-back PWM converters with a DC link capacitor. The frequency of the voltage injected into the rotor is adjusted according to the turbine's speed variation to maintain a constant frequency at the stator terminals.

In this chapter, we aim to develop a mathematical model that accurately represents the real behavior of the DFIG. We will start by defining the mathematical model of the machine, expressing the electrical, magnetic, and mechanical equations governing its operation. Subsequently, using the Park transformation, we will derive a DFIG model in the commonly used *dq* reference frame. Next, we will discuss vector control, which is chosen as the entry point since it is a well-established method in the literature. As the most prevalent method, the stator flux orientation of the DFIG is used to decouple the active and reactive powers exchanged with the grid. We will then model the remaining control-related elements such as the Transformation Block and Position Calculation Block.

Finally, the overall system's performance will be evaluated under various conditions through a series of simulations conducted using MATLAB/SIMULINK.

4.2 Doubly-Fed Induction Generator

The DFIG, commonly employed as a variable speed generator in connection with the power grid, consists of a stator comprising three sets of coils arranged uniformly in identical slots and phased 120 degrees apart. Similarly, the rotor features identical slots with windings also phased at 120-degree intervals. However, the rotor windings are connected to copper collector rings. These windings generate a sinusoidal distribution of magnetic flux across the air gap and are represented by vectors, along with currents and magnetomotive forces (MMFs)[58]. Figure 4-1 illustrates the fundamental configuration of the DFIG.

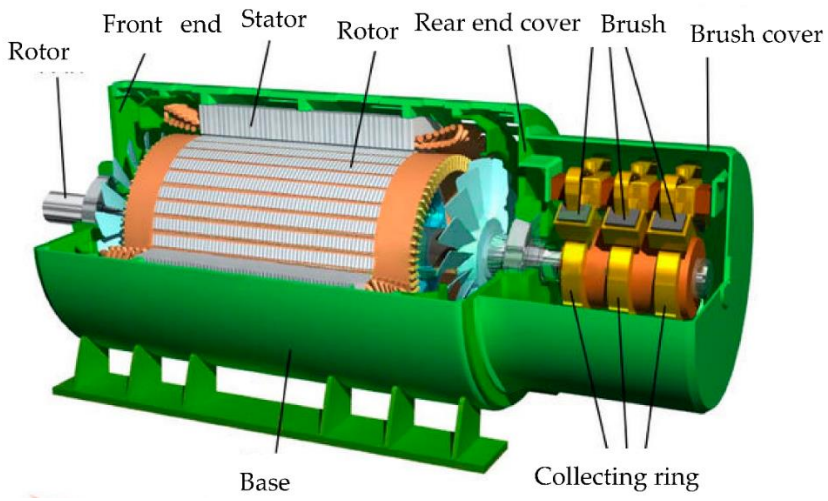

Figure 4-1 Structure of the DFIG

The DFIG's core functionality can be summarized as follows [7]:

- Three-phase AC power from a source with frequency *fs* energizes the stator windings. This energization creates a rotating stator magnetic field, spinning at a synchronous speed of $2\pi f_s/p$, where p signifies the number of pole pairs.
- Three-phase voltages, whose frequency and magnitude are variable and contingent on the rotor's mechanical speed, feed the rotor windings through slip rings. This action generates a rotor magnetic field within the air gap, rotating spatially at the same speed as the stator flux.
- A phase shift exists between the stator and rotor magnetic fields, facilitating the generation of electromagnetic torque through their interaction.
- The synchronous speed, ns, is determined by the number of poles (*P*) of the DFIG and the frequency (f_s) of the voltage supplied from the grid. This relationship is expressed as $n_s=P2\pi f_s$.
- The slip (*s*), which represents the difference between the synchronous speed *ns* and the actual rotor speed *n*, is typically expressed as a percentage of the synchronous speed and can be calculated as: $s=(n_s-n)\backslash n$
- The frequency of voltage and current in the rotor is determined by the slip. $F_r=sf_s$[7]

- The DFIG can operate in both sub-synchronous and super-synchronous speed modes thanks to the back-to-back power converter configuration. These converters allow for flexible control of the rotor current, enabling the DFIG to function at speeds both below and above the synchronous speed as shown in Figure 4-2.

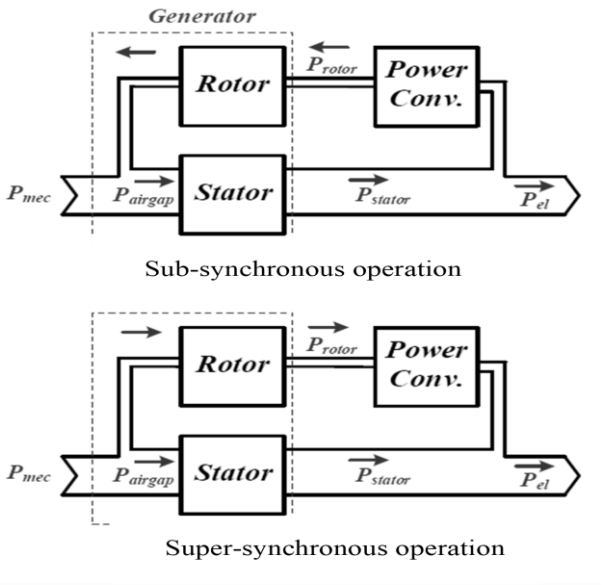

Figure 4-2 the operation of the DFIG

1. **Sub-Synchronous Speed Operation:** When the rotor operates at a speed below the synchronous speed:

- The DFIG draws power from the grid via the rotor-side converter (RSC) to compensate for the mechanical energy shortfall.
- The stator supplies active power to the grid while the rotor consumes power to maintain the required torque and rotor speed.
- The rotor current frequency is lower than the grid frequency, allowing the rotor to be controlled for optimal torque and speed.

2. **Super-Synchronous Speed Operation:** When the rotor operates above synchronous speed:

- The rotor generates excess mechanical power, which is transferred to the grid through the grid-side converter (GSC).

- The stator continues to supply power to the grid, while the rotor also contributes surplus power, increasing the total power output.
- The rotor current frequency is higher than the grid frequency, and the RSC adjusts the rotor voltage and current to ensure efficient power delivery.

4.3 DFIG Dynamic Model

To comprehend and analyze the behavior of a DFIG within a wind energy conversion system, a dynamic model is indispensable. This model delineates the mathematical correlations among the diverse electrical and mechanical parameters inherent in the DFIG's functionality. It serves to elucidate the connections between active power, reactive power, voltages, and currents under varying operational scenarios.

4.3.1 Basic Machine Configuration

A schematic diagram depicting the fundamental configuration of a three-phase DFIG is presented in Figure 3.2. Additionally, reference [7] provides a set of equations derived using Kirchhoff's voltage laws to analyze the electrical behavior of the stator and rotor windings within the DFIG.

$$\begin{cases} v_{sa} = r_s i_{sa} + \frac{d\psi_{sa}}{dt} \\ v_{sb} = r_s i_{sb} + \frac{d\psi_{sb}}{dt} \\ v_{sc} = r_s i_{sc} + \frac{d\psi_{sc}}{dt} \end{cases} \quad (4\text{-}1)$$

$$\begin{cases} v_{sa} = r_s i_{sa} + \frac{d\psi_{sa}}{dt} \\ v_{sb} = r_s i_{sb} + \frac{d\psi_{sb}}{dt} \\ v_{sc} = r_s i_{sc} + \frac{d\psi_{sc}}{dt} \end{cases} \quad (4\text{-}2)$$

Where

- $v_{sa}, v_{sb}\ v_{sc}$ *The stator voltages*
- $v_{ra}, v_{rb}\ v_{rc}$ *The rotor voltages*
- i_{sa}, i_{sb}, i_{sc} *The stator currents*
- i_{ra}, i_{rb}, i_{rc} *The rotor currents*
- $\psi_{sa}, \psi_{sb}, \psi_{sc}$ *The stator flux linkages*
- $\psi_{ra}, \psi_{rb}\ \psi_{rc}$ *The rotor flux linkages*

The stator equations are formulated in the stationary reference frame, whereas the rotor equations are expressed in the rotating reference frame synchronized with the rotor.

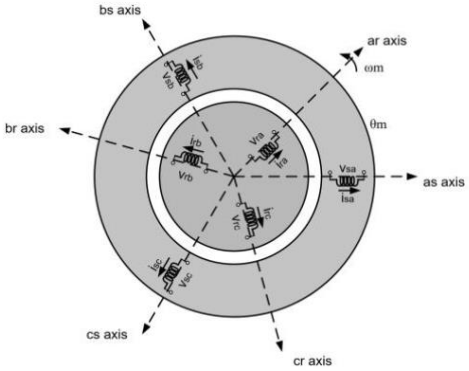

Figure 4-3 DFIG Three-Phase Winding Circuit [58]

4.3.2 Definition and Projection of Space Vectors

The space vector representation of three-phase quantities in a DFIG, such as voltages, currents and flux linkages, is essential for analysis and control. It allows us to describe these quantities in a compact and efficient manner [7],[58]. For instance, the space vector of a generic quantity $\vec{x}_s$ is defined based on its three phase instantaneous magnitudes x_{sa}, x_{sb} and x_{sc} .

$$\vec{x}_s = \frac{2}{3}\left(x_{sa} + x_{sb}e^{j(2\pi/3)} + x_{sc}e^{-j(2\pi/3)}\right) \quad (4\text{-}3)$$

The space vector is visualized on the complex plane by adding together the three individual components, each positioned along an axis at 120-degree angles from one another. This process is illustrated in Figure 4-4, showing how the space vector is derived as the sum of these individual components.

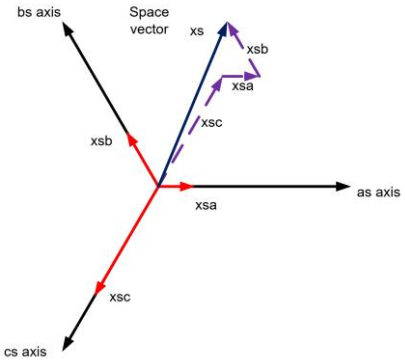

Figure 4-4 Stator Current Space Vector and Its Projection

Hence, the DFIG dynamic model represented by equation (4.1) and (4.2) can be reorganized using the space vector representation:

$$\vec{v}_s^s = r_s\vec{i}_s^s + \frac{d\vec{\psi}_s^s}{dt} \quad (4\text{-}4)$$

$$\vec{v}_r^r = r_r\vec{i}_r^r + \frac{d\vec{\psi}_r^r}{dt} \quad (4\text{-}5)$$

The total flux linkages in both the stator and rotor are influenced by their respective current space vectors according to the provided equations.

$$\vec{\psi}_s^s = L_s\vec{i}_s^s + L_m\vec{i}_r^s \quad (4\text{-}6)$$

$$\vec{\psi}_r^r = L_m\vec{i}_s^r + L_r\vec{i}_r^r \quad (4\text{-}7)$$

The superscripts s and r signify the space vectors pertaining to the stator or rotor reference frame. L_s represents the stator inductance; L_r denotes the rotor inductance, and L_m stands for mutual inductance.

The space vector offers the advantage of being transformable into two-phase quantities along any arbitrary complex plane. x_d is the direct axe and x_q, represent the quadrature axe, can be expressed as:

$$\begin{cases} x_d = |\vec{x}_s|cos\ \theta \\ x_q = j|\vec{x}_s|sin\ \theta \end{cases} \quad (4\text{-}8)$$

θ represents the angle between the direct axis and the space vector.

4.3.3 DFIG Model within an Arbitrary Reference Frame

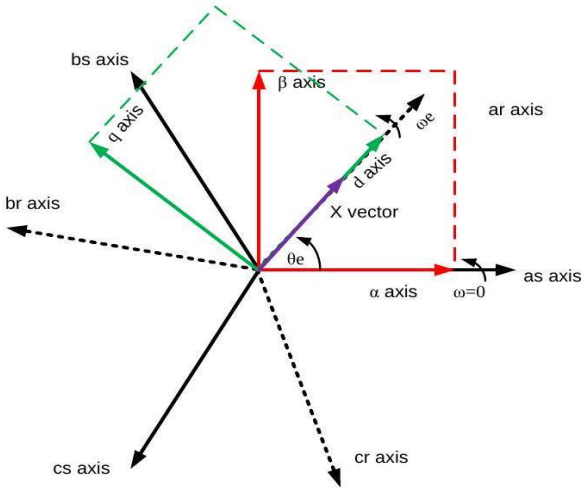

Figure 4-5 abc, αβ and dq reference frame

As equations (4.6) and (4.7) are referenced to different frames, aligning them to the same reference frame aids in simplifying the model. Two commonly used reference frames for modeling DFIG are the *s*tationary and *r*otating frames.

In the *s*tationary reference frame, denoted as the $\alpha\beta$ frame, the angular speed (ω) is zero. Here, the α-axis aligns with the magnetic axis of phase a of the stator winding.

Conversely, the *r*otating reference frame, known as the dq frame, is characterized by an *a*ngular position θ_e relative to the $\alpha - axis$ is and an angular speed (ω_e). In this frame, the $d - axis$ aligns with a chosen *s*pace vector, often determined by the control technique employed. Common choices include the phase a of the *r*otor winding, the *s*tator flux linkage *s*pace vector, and the rotor flux linkage space vector, as depicted in Figure 4-5.

Essentially, the quantities of the stator winding's three phases are converted into two-phase quantities represented in the stator reference frame, which is depicted on the $\alpha\beta$ complex plane. Similarly, the three-phase quantities of the rotor winding are transformed into two-phase quantities situated in the rotor reference frame, depicted on the DQ complex plane. This frame rotates at a *s*peed of $p\omega_m$, where ω_m represents the mechanical rotor speed, and p denotes the number of pole pairs of the DFIG. Consequently, the dynamic model of the two-phase DFIG can be expressed in terms of space vector components as:

$$\begin{cases} v_{s\alpha} = r_s i_{s\alpha} + \frac{d\psi_{s\alpha}}{dt} \\ v_{s\beta} = r_s i_{s\beta} + \frac{d\psi_{s\beta}}{dt} \end{cases} \quad (4\text{-}9)$$

$$\begin{cases} v_{rD} = r_s i_{rD} + \frac{d\psi_{rD}}{dt} \\ v_{rQ} = r_s i_{rQ} + \frac{d\psi_{rQ}}{dt} \end{cases} \quad (4\text{-}10)$$

4.3.4 DFIG αβ model

To characterize the DFIG model in the stationary reference frame ($\alpha\beta$), we convert the space vector components from the rotor frame (DQ) to the stator frame by employing the rotational conversion factor.$e^{j\theta m}$, given by:

$$\begin{bmatrix} x_{r\alpha} \\ x_{r\beta} \end{bmatrix} = \begin{bmatrix} cos\ \theta_m & -sin\ \theta_m \\ sin\ \theta_m & cos\ \theta_m \end{bmatrix} \begin{bmatrix} x_{rD} \\ x_{rQ} \end{bmatrix} \quad (4\text{-}11)$$

where θ_m can be calculated from:

$$\theta_m = \int p\omega_m dt \quad (4\text{-}12)$$

Hence, the dynamic model of the DFIG in the $\alpha\beta$ plane is described by next equations and can be illustrated via the equivalent circuit depicted in Figure 4-6[7].

$$\begin{cases} v_{s\alpha} = r_s i_{s\alpha} + \frac{d\psi_{s\alpha}}{dt} \\ v_{s\beta} = r_s i_{s\beta} + \frac{d\psi_{s\beta}}{dt} \end{cases} \quad (4\text{-}13)$$

$$\begin{cases} v_{r\alpha} = r_s i_{r\alpha} + \frac{d\psi_{r\alpha}}{dt} + p\omega_m \psi_{r\beta} \\ v_{r\beta} = r_s i_{r\beta} + \frac{d\psi_{r\beta}}{dt} - p\omega_m \psi_{r\alpha} \end{cases} \quad (4\text{-}14)$$

$$\begin{cases} \psi_{s\alpha} = L_s i_{s\alpha} + L_m i_{r\alpha} \\ \psi_{s\beta} = L_s i_{s\beta} + L_m i_{r\beta} \end{cases} \quad (4\text{-}15)$$

$$\begin{cases} \psi_{r\alpha} = L_m i_{s\alpha} + L_r i_{r\alpha} \\ \psi_{r\beta} = L_m i_{s\beta} + L_r i_{r\beta} \end{cases} \quad (4\text{-}16)$$

Using the circuit depicted in Figure 4-6, the active and reactive powers of the stator and rotor are determined as follows [7]:

$$P_s = \frac{3}{2}\left(v_{s\alpha} i_{s\alpha} + v_{s\beta} i_{s\beta}\right) \quad (4\text{-}17)$$

$$P_r = \frac{3}{2}\left(v_{r\alpha} i_{r\alpha} + v_{r\beta} i_{r\beta}\right) \quad (4\text{-}18)$$

$$Q_s = \frac{3}{2}\left(v_{s\beta} i_{s\alpha} - v_{s\alpha} i_{s\beta}\right) \quad (4\text{-}19)$$

$$Q_r = \frac{3}{2}\left(v_{r\beta} i_{r\alpha} - v_{r\alpha} i_{r\beta}\right) \quad (4\text{-}20)$$

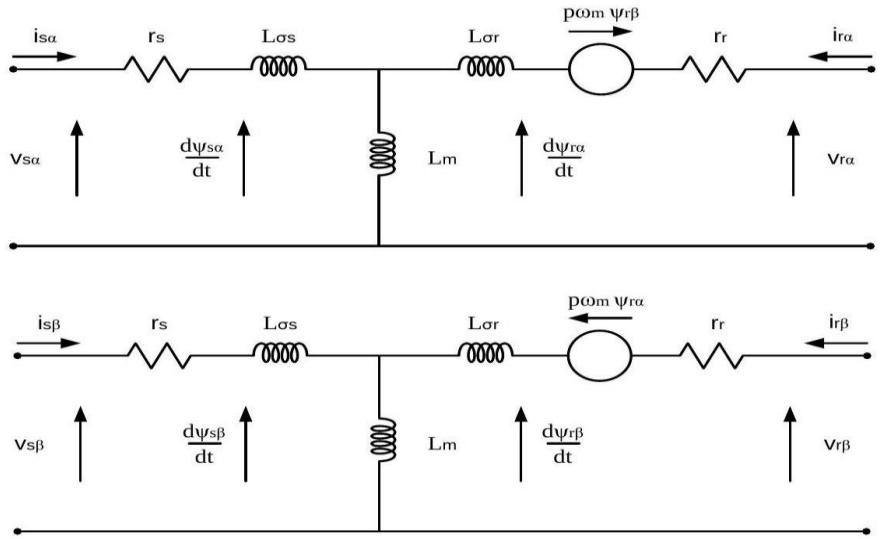

Figure 4-6 Schematic of DFIG αβ model [58]

The electromagnetic torque of the DFIG is defined in terms of the rotor flux linkages and rotor currents as follows [7]:

$$T_{em} = \frac{3}{2}p\left(\psi_{r\beta} i_{r\alpha} - \psi_{r\alpha} i_{r\beta}\right) \quad (4\text{-}21)$$

Upon substituting equations (4.13) and (4.14) into equations (4.15) and (4.16), the dynamic equations of the DFIG in the $\alpha\beta$ frame are as follows [7]:

$$\begin{cases} \frac{d\psi_{s\alpha}}{dt} = -\frac{r_s\psi_{s\alpha}}{\sigma L_s} + \frac{r_s L_m \psi_{r\alpha}}{\sigma L_s L_r} + v_{s\alpha} \\ \frac{d\psi_{s\beta}}{dt} = -\frac{r_s\psi_{s\beta}}{\sigma L_s} + \frac{r_s L_m \psi_{r\beta}}{\sigma L_s L_r} + v_{s\beta} \\ \frac{d\psi_{r\alpha}}{dt} = \frac{r_r L_m \psi_{s\alpha}}{\sigma L_s L_r} - \frac{r_r\psi_{r\alpha}}{\sigma L_r} - p\omega_m\psi_{r\beta} + v_{r\alpha} \\ \frac{d\psi_{r\beta}}{dt} = \frac{r_r L_m \psi_{s\beta}}{\sigma L_s L_r} + p\omega_m\psi_{r\alpha} - \frac{r_r\psi_{r\beta}}{\sigma L_r} + v_{r\beta} \\ \frac{d\omega_m}{dt} = \frac{T_{em}}{J} - \frac{T_m}{J} \end{cases} \quad (4\text{-}22)$$

Where $\sigma = 1 - L_m{}^2/L_s L_r$ i is a coefficient leakage flux, T_m denotes the mechanical torque and J is the moment of inertia of the rotor.

4.3.5 DFIG dq model

To express the DFIG model in the rotating reference frame (dq), we transform the space vector components from the stator frame (αβ) to components in the arbitrary rotating reference frame using the conversion factor $e^{j\theta s}$ as outlined [7]:

$$\begin{bmatrix} x_{sd} \\ x_{sq} \end{bmatrix} = \begin{bmatrix} cos\ \theta_s & sin\ \theta_s \\ -sin\ \theta_s & cos\ \theta_s \end{bmatrix} \begin{bmatrix} x_{s\alpha} \\ x_{s\beta} \end{bmatrix} \quad (4\text{-}23)$$

θ_s denotes the angular position between the direct axis of the stationary frame and the rotating frame. Subsequently, the components of the space vector in the rotor frame (DQ) are converted into vectors in the arbitrary rotating reference frame using the conversion factor.

$$\begin{bmatrix} x_{rd} \\ x_{rq} \end{bmatrix} = \begin{bmatrix} cos\ (\theta_s - \theta_m) & sin\ (\theta_s - \theta_m) \\ -sin\ (\theta_s - \theta_m) & cos\ (\theta_s - \theta_m) \end{bmatrix} \begin{bmatrix} x_{rD} \\ x_{rQ} \end{bmatrix} \quad (4\text{-}24)$$

The dynamic model of the DFIG in the arbitrary rotating frame (dq) is given by [7]:

$$\begin{cases} v_{sd} = r_s i_{sd} + \frac{d\psi_{sd}}{dt} - \omega_s\psi_{sq} \\ v_{sq} = r_s i_{sq} + \frac{d\psi_{sq}}{dt} + \omega_s\psi_{sd} \end{cases} \quad (4\text{-}25)$$

$$\begin{cases} v_{rd} = r_s i_{rd} + \frac{d\psi_{rd}}{dt} - (\omega_s - p\omega_m)\psi_{rq} \\ v_{rq} = r_s i_{rq} + \frac{d\psi_{rq}}{dt} + (\omega_s - p\omega_m)\psi_{rd} \end{cases} \quad (4\text{-}26)$$

$$\begin{cases} \psi_{sd} = L_s i_{sd} + L_m i_{rd} \\ \psi_{sq} = L_s i_{sq} + L_m i_{rq} \end{cases} \quad (4\text{-}27)$$

$$\begin{cases}\psi_{rd} = L_m i_{sd} + L_r i_{rd} \\ \psi_{rq} = L_m i_{sq} + L_r i_{rq}\end{cases} \quad (4\text{-}28)$$

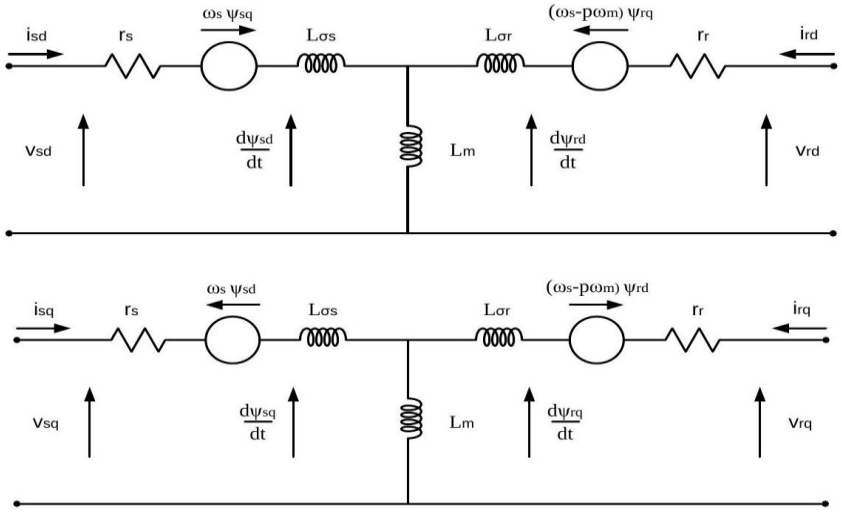

Figure 4-7 Schematic of DFIG dq model [58]

The dq model of the DFIG can be represented by the equivalent circuit shown in Figure 4-7. From this circuit , the active and the reactive powers of the stator and rotor can be calculated as follows [7]:

$$P_s = \frac{3}{2}\left(v_{sd} i_{sd} + v_{sq} i_{sq}\right) \quad (4\text{-}29)$$

$$P_r = \frac{3}{2}\left(v_{rd} i_{rd} + v_{rq} i_{rq}\right) \quad (4\text{-}30)$$

$$Q_s = \frac{3}{2}\left(v_{sq} i_{sd} - v_{sd} i_{sq}\right) \quad (4\text{-}31)$$

$$Q_r = \frac{3}{2}\left(v_{rq} i_{rd} - v_{rd} i_{rq}\right) \quad (4\text{-}32)$$

The electromagnetic torque of the DFIG can be expressed as :

$$T_{em} = \frac{3}{2} p \frac{L_m}{L_s}\left(\psi_{sq} i_{rd} - \psi_{sd} i_{rq}\right) \quad (4\text{-}33)$$

The state-space dynamic equations of the DFIG in dq frame and the rotor dynamics can be written as [7]:

$$\begin{cases}\frac{d\psi_{sd}}{dt} = -\frac{r_s \psi_{sd}}{\sigma L_s} + \omega_s \psi_{sq} + \frac{r_s L_m \psi_{rd}}{\sigma L_s L_r} + v_{sd} \\ \frac{d\psi_{sq}}{dt} = -\omega_s \psi_{sd} - \frac{r_s \psi_{sq}}{\sigma L_s} + \frac{r_s L_m \psi_{rq}}{\sigma L_s L_r} + v_{sq} \\ \frac{d\psi_{rd}}{dt} = \frac{r_r L_m \psi_{sd}}{\sigma L_s L_r} - \frac{r_r \psi_{rd}}{\sigma L_r} + (\omega_s - p\omega_m)\psi_{rq} + v_{rd} \\ \frac{d\psi_{rq}}{dt} = \frac{r_r L_m \psi_{sq}}{\sigma L_s L_r} - (\omega_s - p\omega_m)\psi_{rd} - \frac{r_r \psi q}{\sigma L_r} + v_{rq} \\ \frac{d\omega_m}{dt} = \frac{T_{em}}{J} - \frac{T_m}{J}\end{cases} \quad (4\text{-}34)$$

4.3.6 DFIG Model Simulation

The $\alpha\beta$ model discussed earlier takes inputs such as stator voltages $(v_{s\alpha}, v_{s\beta})$, rotor voltages $(v_{r\alpha}, v_{r\beta})$, and mechanical torque T_m. Outputs include stator flux linkages ,$(\psi_{s\alpha}$, $\psi_{s\beta})$ and rotor flux linkages $(\psi_{r\alpha}$, $\psi_{r\beta})$, and mechanical speed ω_m . The electromagnetic torque in equation (4.21) can be rearranged in terms of stator and rotor flux linkages as described in [7].

$$T_{em} = \frac{3}{2}\frac{L_m}{\sigma L_s L_r} p\left(\psi_{r\alpha}\psi_{s\beta} - \psi_{r\beta}\psi_{s\alpha}\right) \qquad (4\text{-}35)$$

The stator and rotor currents can be rearranged from (4.15) and (4.16) as [7]:

$$\begin{cases} i_{s\alpha} = \dfrac{\psi_{s\alpha}}{\sigma L_s} + \dfrac{L_m \psi_{r\alpha}}{\sigma L_s L_r} \\ i_{s\beta} = \dfrac{\psi_{s\beta}}{\sigma L_s} + \dfrac{L_m \psi_{r\beta}}{\sigma L_s L_r} \\ i_{r\alpha} = \dfrac{\psi_{r\alpha}}{\sigma L_r} + \dfrac{L_m \psi_{s\alpha}}{\sigma L_s L_r} \\ i_{r\beta} = \dfrac{\psi_{r\beta}}{\sigma L_r} + \dfrac{L_m \psi_{s\beta}}{\sigma L_s L_r} \end{cases} \qquad (4\text{-}36)$$

Figure 4-8 illustrates the αβ DFIG model adapted to be compatible with the real three-phase system.

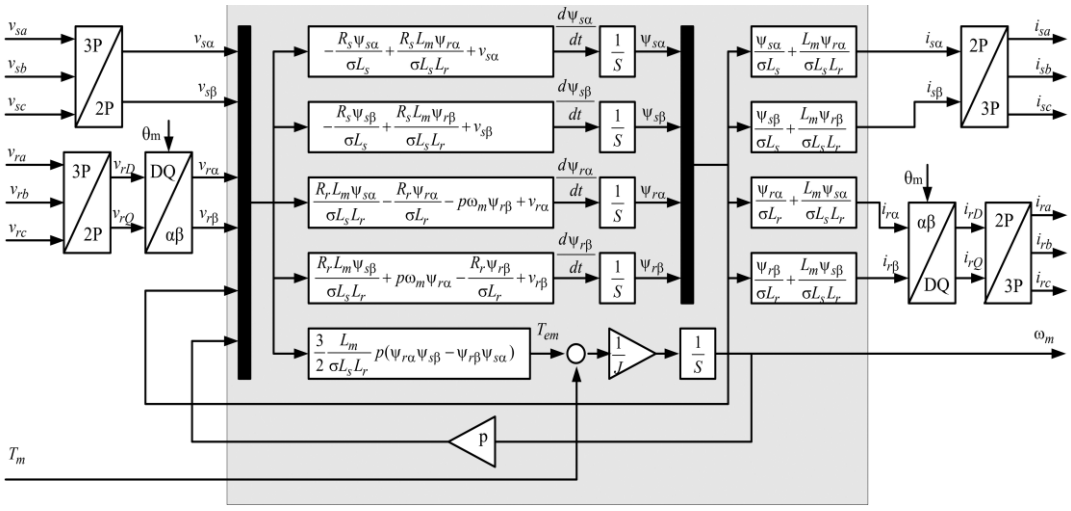

Figure 4-8 DFIG model simulation block diagram [58]

4.4 Control of rotor-side converter

The utilization of the DFIG offers a distinct advantage: the capability to operate at variable speeds, aligning with the optimal power characteristics of the wind turbine. This characteristic elucidates that for each wind speed encountered, there exists an ideal

rotation speed corresponding to the maximum value of the power coefficient. This optimal rotation speed ensures that the wind turbine achieves its highest possible efficiency.

Achieving this optimal rotation speed necessitates the presence of a specific mechanical resisting torque within the turbine, which is facilitated by an active power delivered by the DFIG. Essentially, the DFIG serves as a mechanism to provide the requisite power reference for controlling the turbine's operation [12].

In essence, the DFIG's ability to supply the necessary power to enable the turbine to rotate at its optimal speed ensures that the wind energy conversion system operates efficiently across varying wind speeds. By aligning the turbine's rotation with the optimal power characteristic, the DFIG plays a crucial role in enhancing the overall performance and energy output of wind turbines.

In our endeavor, we have strategically aligned the stator flux along the d-axis to facilitate the application of vector control techniques. This deliberate selection of reference axis enables us to ensure that the generated active power is directly linked to the q-component of the rotor current, i_{qr}, while concurrently associating the reactive power with the d-component of the rotor current, i_{dr}. Consequently, by adopting this approach, we can effectively regulate these stator powers independently of each other.

By aligning the stator flux vector with the d-axis and disregarding the per phase stator resistance, the expression for the d-component of the stator flux can be formulated as follows [12],[59]:

$$\begin{cases} \psi_{ds} = |\psi_s| \\ \psi_{qs} = 0 \end{cases} \quad (4\text{-}37)$$

The electromagnetic torque in equation is written as:

$$T_{em} = -\frac{3}{2} p \frac{L_m}{L_s} \psi_{ds} i_{qr} \quad (4\text{-}38)$$

And the equation 4.27 of the stator fluxes according to equation 4.37 becomes:

$$\begin{cases} \varphi_{ds} = L_s . I_{ds} + L_m . I_{dr} \\ 0 = L_s . I_{qs} + L_m . I_{qr} \end{cases} \quad (4\text{-}39)$$

The stator voltage in equation becomes:

$$\begin{cases} v_{ds} \approx 0 \\ v_{qs} \approx \omega_s \psi_{sd} = V_g \end{cases} \quad (4\text{-}40)$$

Using the equation (4-39) we can establish the link between the stator and rotor currents:

$$\begin{cases} i_{ds} = \frac{\psi_{ds}}{L_s} - \frac{L_m}{L_s} i_{dr} \\ i_{qs} = -\frac{L_m}{L_s} i_{qr} \end{cases} \quad (4\text{-}41)$$

Finally, active power and reactive power in equations 4-29 and 4-31 are written as follows:

$$\begin{cases} P_s = -\frac{3}{2}\frac{L_m}{L_s} V_g i_{qr} \\ Q_s = \frac{3}{2}\frac{V_g^2}{\omega_s L_s} - \frac{3}{2}\omega_s V_g \frac{L_m}{L_s} i_{dr} \end{cases} \quad (4\text{-}42)$$

The equations above unequivocally demonstrate the decoupling of active and reactive powers, enabling the control of active power through the direct current and reactive power through the quadrature current. Reference currents are derived from the desired powers. Subsequently, control loops are employed to ensure that the actual currents closely adhere to these references.

Achieving precise control over power flow within the stator is paramount, even when faced with variations in machine parameters or slight deviations in the reference frame alignment. Typically, a dual-loop control system is implemented for this purpose, as illustrated in Figure 4-9, where the *u* factor is defined by the stator and rotor turns ratio : $u=N_s/N_r$.

In the first loop, the regulation of reactive power is managed. Here, a proportional-integral (PI) regulator generates the reference current for the d-axis rotor, referred to as i_{dr}. This reference current is derived from the disparity between the commanded reactive power and the actual reactive power output.

Conversely, the second loop is dedicated to regulating active power. Within this loop, another PI regulator generates the reference current for the q-axis rotor, i_{qr}. It operates by comparing the commanded active power with the actual active power output.

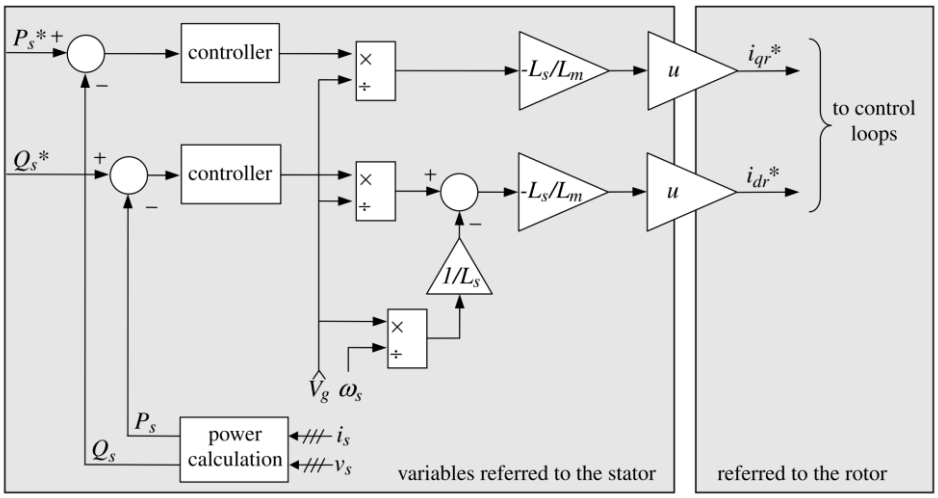

Figure 4-9 External power loops [7]

To ensure accurate control of the machine, it's crucial to establish the connection between rotor currents and voltages applied to DFIG. This involves substituting the stator currents in the flux equation with the expression (4-28), resulting in:

$$\begin{cases} \varphi_{dr} = \left(L_r - \frac{L_m^2}{L_s}\right).I_{dr} + \frac{L_m}{L_s}\varphi_{ds} \\ \varphi_{qr} = \left(L_r - \frac{L_m^2}{L_s}\right).I_{qr} \end{cases} \quad (4\text{-}43)$$

The initial components of the aforementioned equations provide the flux directly associated with the rotor current. This relationship between the fluxes and the currents is quantified by the transient inductance of the rotor, denoted as σ. It is determined by combining the rotor leakage inductance in series with the parallel magnetizing inductance and the stator leakage inductance:

$$\sigma = 1 - \frac{L_m^2}{L_s L_r} \quad (4\text{-}44)$$

Here, σ represents the leakage coefficient.

Substituting the expression of the rotor fluxes into the rotor voltages expression yields:

$$\begin{cases} v_{dr} = R_r i_{dr} + \sigma L_r \frac{di_{dr}}{dt} - \omega_r \sigma L_r i_{qr} \\ v_{qr} = R_r i_{qr} + \sigma L_r \frac{di_{qr}}{dt} + \omega_r \sigma L_r i_{dr} + \omega_r \frac{L_m}{L_s}\psi_{ds} \end{cases} \quad (4\text{-}45)$$

Based on the preceding equations, we can establish the connections between the applied rotor voltages and the stator powers. With this information, we can now construct the block diagram of the DFIG, as depicted in Figure 4-10.

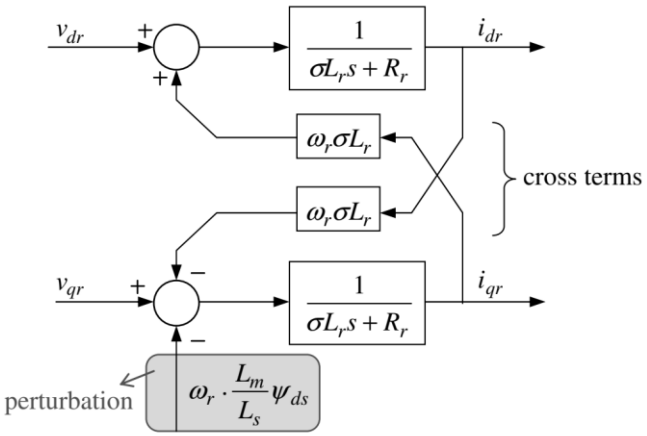

Figure 4-10 The block diagram of the DFIG

From a control perspective, the term $\omega_r . \frac{L_m}{L_s} \psi_{ds}$ can be considered a disturbance as it relies on the stator flux, which is an external variable independent of the control loop. Since this term remains constant, it can be readily compensated for by the controller. Additionally, the cross-terms remain constant during steady-state operation and do not interfere with the functionality of the control loops. Typically, these terms are estimated and accounted for by the control system to mitigate their adverse effects during transient phases. This process is illustrated in Figure 4-11[7, 12, 15,58].

It's worth noting that compensating for the cross terms significantly simplifies the control loop. Both axes become identical, and their plant is reduced to a first-order transfer function. Consequently, the d and q axes can be controlled independently. This simplification leads to a global command structure, as depicted in the figure. Such a structure results in a streamlined regulation system. The integral-proportional regulator employed for current and power control is straightforward to implement and offers satisfactory performance for generator applications.

Furthermore, the symmetry achieved in the system after compensation enables the regulators to be calculated for only one axis. The regulators for the other two axes will mirror the first one, simplifying the design process significantly.

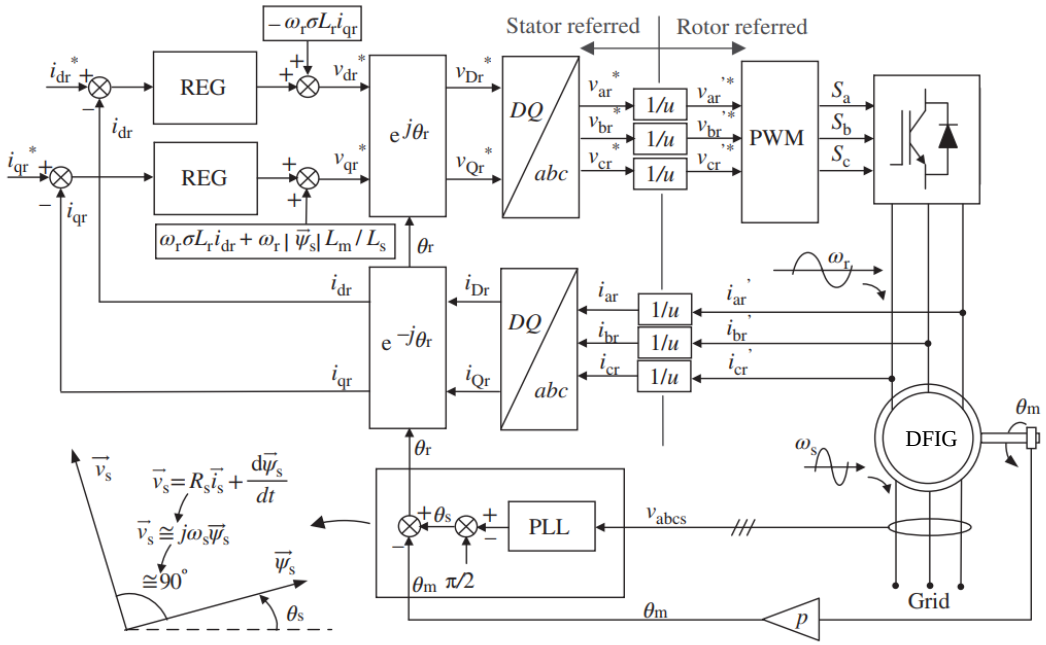

Figure 4-11 The block control of the rotor side converter

4.5 Design of the PI Controller for the RSC

This subsection details the process of selecting the suitable gains for PI controllers utilized in the RSC of DFIG.

4.5.1 The inner current control loop

Utilizing equation (4-45), the closed-loop current control can be depicted through the block diagrams illustrated in Figure 4-12.

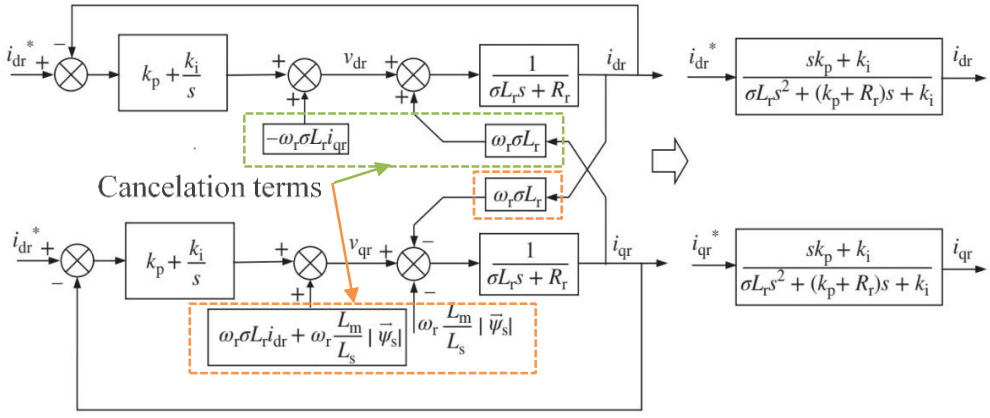

Figure 4-12 The inner current control loop of RSC

By applying Laplace transforms to the quantities depicted in the figure, the closed-loop transfer function of the two inner current control loops can be represented as [12]:

$$\frac{I_{dr}(s)}{I_{dr-ref}(s)} = \frac{I_{qr}(s)}{I_{qr-ref}(s)} = \frac{\frac{K_p s}{\sigma L_r} + \frac{K_i}{\sigma L_r}}{s^2 + \frac{(K_p + r_r)s}{\sigma L_r} + \frac{K_i}{\sigma L_r}} \quad (4\text{-}46)$$

In equation (4.46), K_p denotes the proportional gain, while K_i signifies the integral gain of the PI controllers. This transfer function can be simplified to resemble a standard second-order system by assuming $K_p \ll K_i$, as follows [60]:

$$\frac{I_{rd}(s)}{I_{rd-ref}(s)} = \frac{I_{rq}(s)}{I_{rq-ref}(s)} = \frac{\frac{K_i}{\sigma L_r}}{s^2 + \frac{(K_p + r_r)s}{\sigma L_r} + \frac{K_i}{\sigma L_r}} = \frac{\omega_n^2}{s^2 + 2\zeta\omega_n s + \omega_n^2} \quad (4\text{-}47)$$

In this context, ζrepresents the damping ratio, and ω_n stands for the natural frequency of the transfer function. Typically, the performance of the closed-loop control for the second-order system is assessed through its transient response, primarily focusing on determining the percent overshoot (%OS) and the settling time (ts). These metrics can be computed using the following formulas [61],[62]:

$$\%OS = 100 \cdot exp\left\{\frac{-\zeta\pi}{\sqrt{1-\zeta^2}}\right\} \quad (4\text{-}48)$$

$$t_s = \frac{4}{\zeta\omega_n} \quad (4\text{-}49)$$

For a second-order system, ensuring that the percent overshoot is less than 25% relies solely on the damping ratio, as indicated in equation (4-48). Typically, an optimal damping ratio for a standard second-order system is targeted at 0.707, resulting in a percent overshoot of less than 5% alongside an appropriate settling time [94]. Furthermore, settling time refers to the duration taken for the transient response to reach and maintain within 2% of the steady-state value, as determined by ζ and ωn in equation (4-48) [60].

The value of ωn significantly influences the settling time, with higher ωn leading to a faster response. However, increasing ωn also escalates the gains of the PI controller, thereby diminishing the stability of the closed-loop system. To achieve specified performance from the system, one approach is to design the gains of the PI controller for the current control loop using the pole placement method:

$$\begin{cases} K_p = 2\zeta\omega_n(\sigma L_r) - r_r \\ K_i = \omega_n^2(\sigma L_r) \end{cases} \quad (4\text{-}50)$$

Within this thesis, a damping ratio of ζ=1 is chosen for current control to achieve critical damping, thereby ensuring that the percent overshoot remains below 5%. This is facilitated by the system having two real-number poles. The optimal value of ω_n is determined from equation (4.49), which is dependent on the settling time ts and the damping ratio ζ.

Once ωn is derived based on the desired dynamic performance of the current control loops, the optimal gains of the Proportional-Integral (PI) controller are adjusted using equation (4.50) to meet the desired percent overshoot and settling time criteria. This iterative process ensures that the control system achieves the specified performance objectives.

4.5.2 Outer control loop

As mentioned earlier, the design of the outer loop hinges on the assumption that the current control loops can accurately follow the constant commands issued by the outer loops. However, in practical scenarios, the reactive power control loop and generator speed control loop operate at significantly slower rates compared to the current control loops, typically around four times slower. Consequently, during the execution of outer control loops, the actual currents of the inner control loop are instantaneously assumed to be equal to their respective references, denoted as $i_{rd\_ref} = i_{rd}$ and $i_{rq\_ref} = i_{rq}$. The closed-loop control of reactive power and generator speed is illustrated in the block diagram presented in Figure 4-13[60],[63].

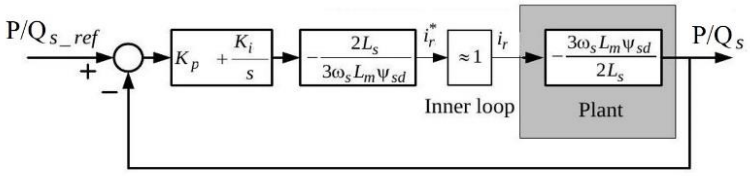

Figure 4-13 Stator active power and reactive power loops of RSC

By performing the Laplace transform on the quantities depicted in Figure 4-13, the transfer function of the stator active and reactive power can be expressed as:

$$\frac{P_s(s)}{P_{s\_ref}(s)} = \frac{Q_s(s)}{Q_{s\_ref}(s)} = \frac{\frac{K_p s}{K_i}+1}{\left(\frac{1}{K_i}+\frac{K_p}{K_i}\right)s+1} \quad (4\text{-}51)$$

It's important to note that the transfer function of the power in equation (4.51) can be approximated to a standard first-order system by assuming $Kp \ll Ki$, resulting in:

$$\frac{P_s(s)}{P_{s\_ref}(s)} = \frac{Q_s(s)}{Q_{s\_ref}(s)} = \frac{1}{\left(\frac{1}{K_i}+\frac{K_p}{K_i}\right)s+1} \approx \frac{1}{\tau s+1} \quad (4\text{-}52)$$

Hence, the time constant of the stator power control is solely determined by Ki. Consequently, the design of Ki for the stator active and reactive power control loop can be approached as follows:

$$K_i = \frac{1}{\tau - K_p/K_i} \quad (4\text{-}53)$$

The gains of the PI controller are adjusted using a similar approach as the inner current control loop, albeit with a settling time for the power control loop that should be at least four times larger than that of the inner control loop [60].

4.6 Overview Diagram of the Overall Wind Turbine System

In earlier sections, we have thoroughly explored the various components that constitute a classical vector control system for a DFIG. These components include:

- **Reference Generation:** This involves the calculation of reference currents, which are derived from the desired values of the stator's active and reactive power. The accuracy of these reference currents is crucial for the optimal performance of the control system, as they serve as the target values that the system aims to achieve.
- **Current Control Loops:** These loops are responsible for ensuring that the actual current values in the system closely follow the reference currents. The control loops continuously adjust the currents to minimize any deviations, thus maintaining the desired performance of the DFIG.
- **Reference Frame Transformations:** These transformations are essential for converting physical quantities into a mathematical framework that is more convenient for control purposes. Typically, this involves converting the currents

and voltages into a rotating reference frame, simplifying the control of the AC quantities in the system.

Figure 4-14 provides a detailed schematic block diagram that illustrates how these components are interconnected within the control system. In this strategy, the reference frame is aligned with the grid voltage vector rather than the stator flux vector. This design choice mitigates potential stability issues discussed in earlier sections. By aligning the reference frame with the grid voltage, the control system can avoid the complexities and instabilities associated with flux-oriented control.

In this control architecture, the RSC and GSC are modeled as two controllable voltage sources. These voltage sources are represented in a reference frame where the stator voltage space vector is aligned with the q-axis. Importantly, the reference frames for the DFIG model, RSC control, and GSC control are all synchronized with the stator voltage. The voltages for the RSC and GSC are generated through the control blocks discussed earlier. When implementing this in Matlab/Simulink, feedback control blocks can be constructed, and the converter controls can be integrated with the DFIG model within the same dq reference frame. However, one critical dynamic relationship that must be considered is the DC-link capacitor dynamics, which governs the interaction between the RSC and GSC. This relationship is vital for accurately modeling the overall system dynamics. The overall dynamic model block diagram, including this relationship, is shown in Figure 4-14.

It is important to keep in mind that our goal is to study the overall operation of the entire system in order to optimize electrical production. Reactive power production at the request of the grid operator, allowing control of the voltage at the connection point to avoid exceeding voltage tolerances, is part of this goal.

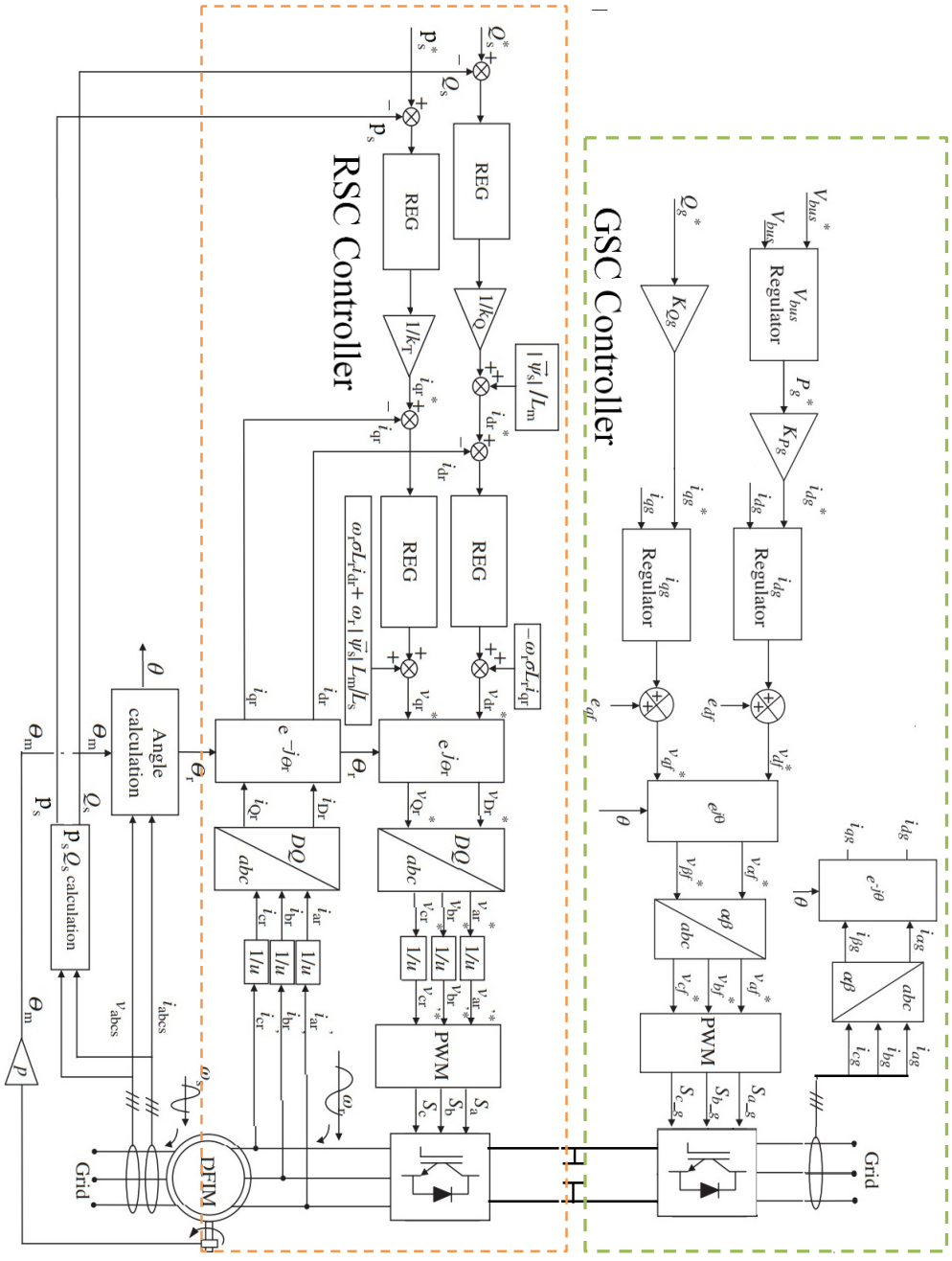

Figure 4-14 Structural Diagram of the Overall Wind Turbine System

4.7 Simulation Results of the Complete System

To comprehensively evaluate the performance and regulatory mechanisms outlined in this chapter, a thorough series of simulations is conducted within the MATLAB/Simulink framework. Leveraging the block diagrams provided in Figure 4-14, we aim to scrutinize

the efficacy of the control system applied to the DFIG . It's noteworthy that the parameters governing these diagrams are explicitly detailed in table 6 in next chapiter .

The simulation model from this block diagram (Figure 4-14) delineates two primary segments: the power module comprising the machine and the converter, and the control module. The latter necessitates validation across three pivotal domains: data acquisition, regulation, and the synthesis of Pulse Width Modulation (PWM) signals derived from the calculated control voltages.

In a bid to assess the efficacy of the control strategy, a dynamic wind speed reference is imposed, enabling us to observe the system's response vis-à-vis grid and converter voltage and current dynamics. This wind profile, as depicted in Figure 4-15, exhibits a variation where the wind speed transitions from 8 m/s at t=2s, to 12 m/s at t=5 s, and reverts to a velocity of 10 m/s at t=10 s.

Figure 4-16 shows that the actual rotor speed follows the reference quite well. Figure 4-17 and Figure 4-18 provide insights into the behavior of active and reactive power post application of reference inputs. Remarkably, they exhibit a commendable conformity and mutual independence. Furthermore, the variations in active power mirror those in torque (Figure 4-19), while reactive power Q is regulated to a zero reference to uphold unity power factor, thereby showcasing the decoupling between these two power domains.

The dynamics of rotor current components along the q and d axes are elucidated in Figure 4-20. Notably, the rotor current (id/iq) impeccably tracks its reference, while the evolution of these components, in tandem with power dynamics, underscores the independence between d and q axis currents, indicative of a robust decoupling mechanism.

Figure 4-21 and Figure 4-22 offer insights into the evolution of machine stator and rotor currents, respectively. Notably, the stator current's variation predominantly mirrors mechanical torque variations, while rotor current frequency primarily aligns with mechanical rotational speed fluctuations.

Figure 4-23 delineates the trajectory of DC bus voltage, affirming its stability around the prescribed value of 1200 V. Transient voltage spikes observed during wind speed variations are acceptable, swiftly returning to the reference value.

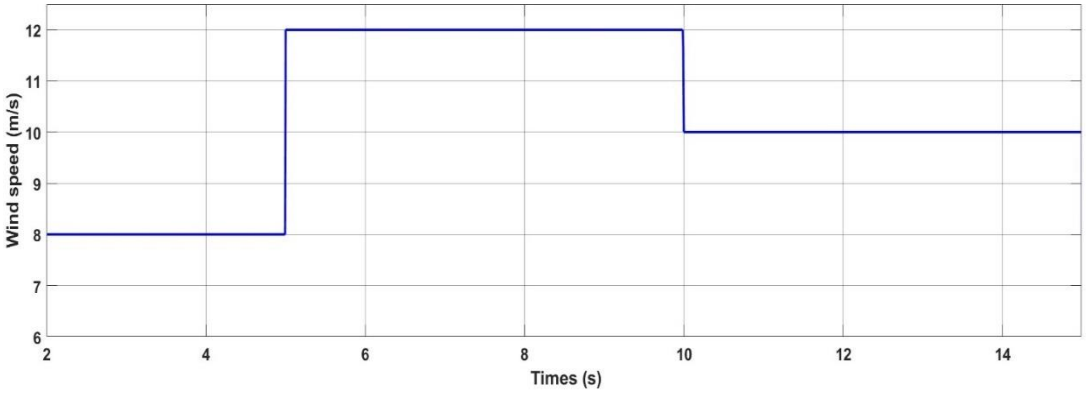

Figure 4-15 Wind profile

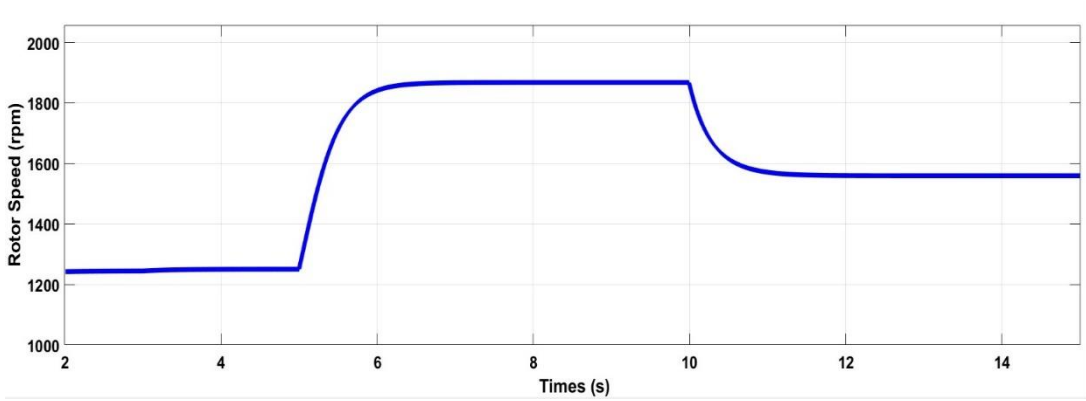

Figure 4-16 Rotor speed

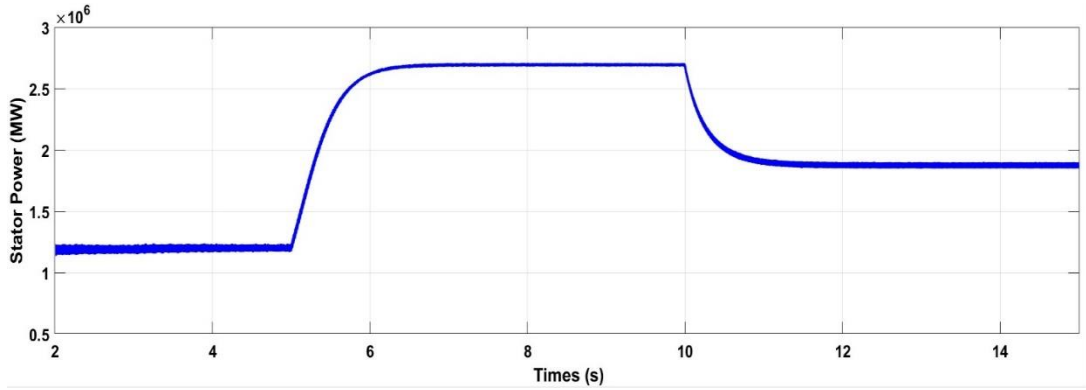

Figure 4-17 Stator power

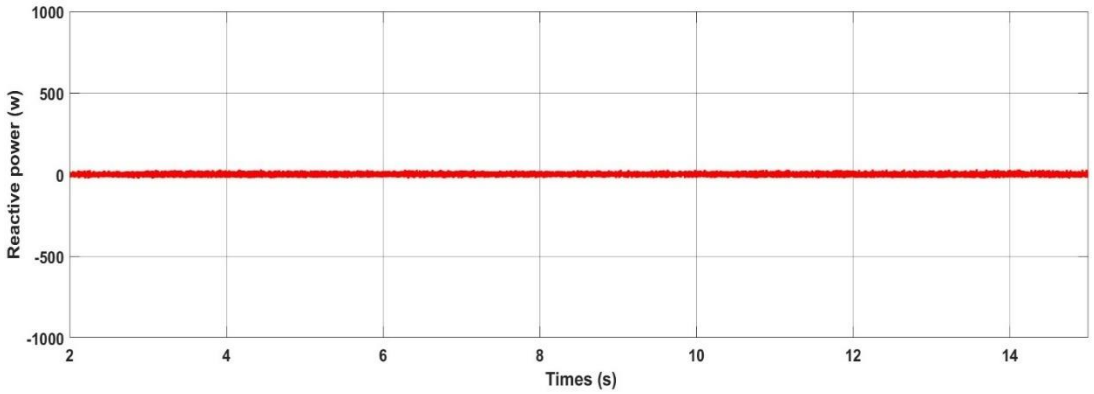

Figure 4-18 Reactive power

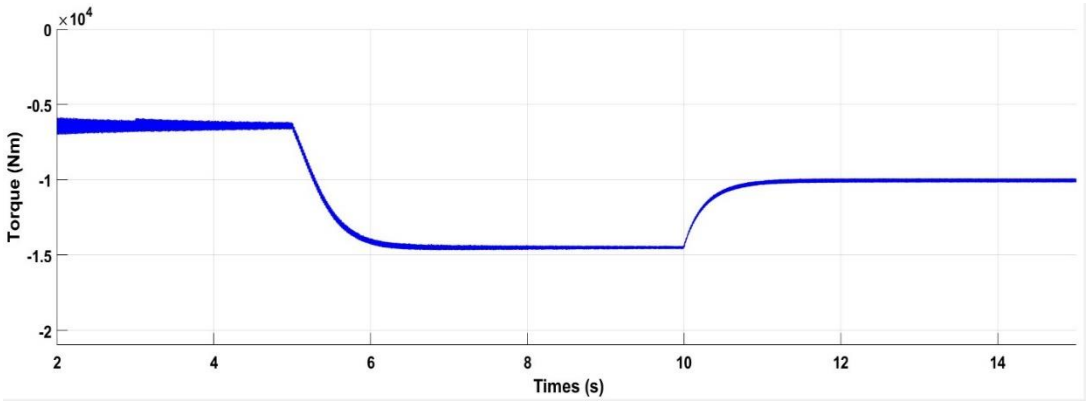

Figure 4-19 Torque

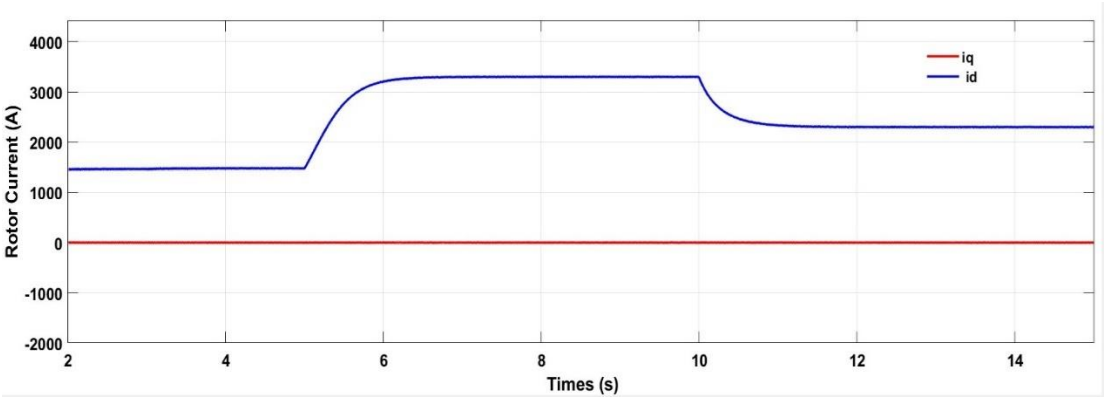

Figure 4-20 Rotor current component (dq)

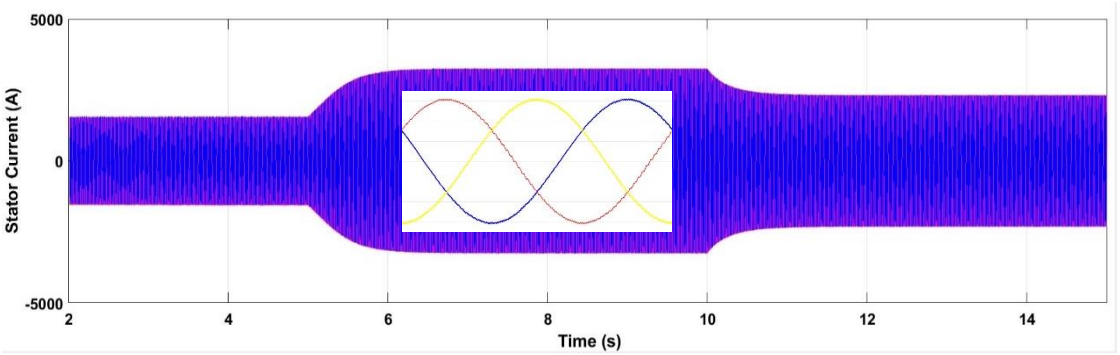

Figure 4-21 Stator current

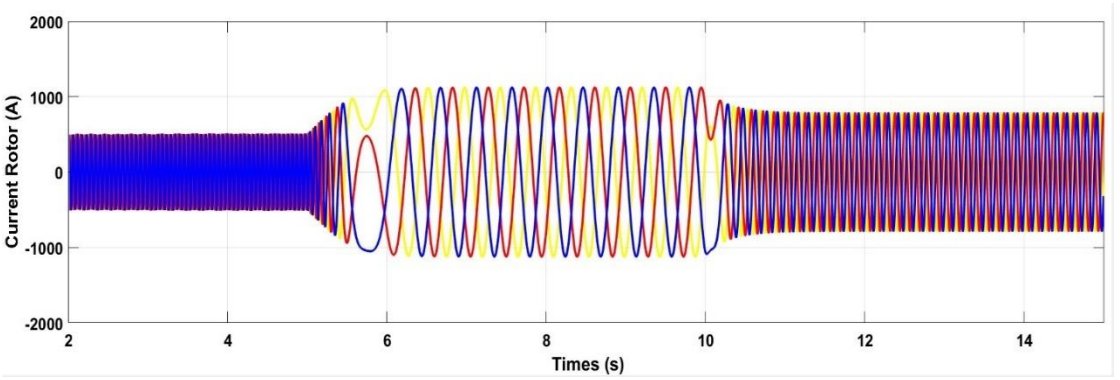

Figure 4-22 Rotor current

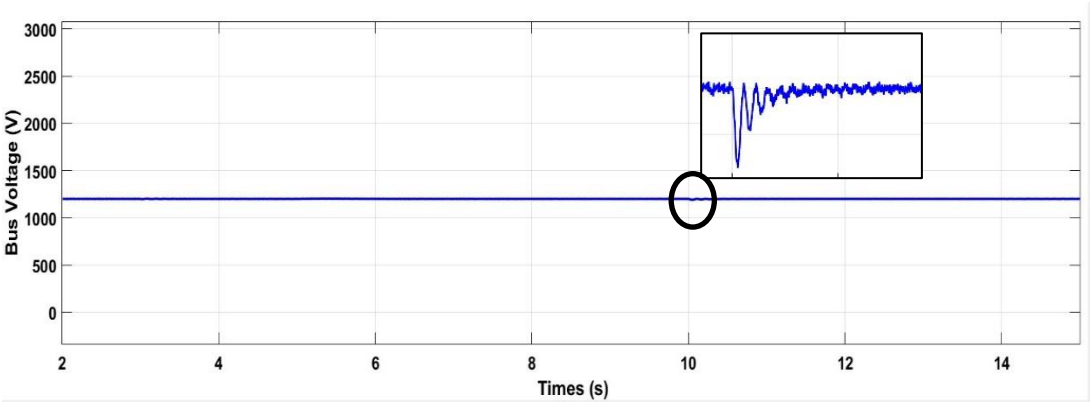

Figure 4-23 DC-bus voltage

4.8 Conclusion

The modeling and simulation of the overall system were developed in this chapter, where we presented the remaining components of the system, along with a detailed study of vector control using stator flux orientation. This control method has been applied to

DFIGs for several years and remains the most widely used. It not only simplifies the machine model but also decouples the regulation of active and reactive power.

The simulation results for the DFIG allowed us to determine and analyze its dynamic behavior under different operating conditions. Using PI controllers, the stator flux orientation technique enables the decoupling of power so that the direct component of the rotor current controls reactive power, and the quadrature component controls active power. The regulation of stator powers is achieved by adjusting the amplitude and frequency of the voltages imposed by the rotor-side power converter.

We have mastered rotor power control by considering the control of the grid-side converter to meet the requirements of the grid operator and to provide greater flexibility to the DFIG.

5 Fractional Order Fuzzy PID Controller for DFIG

5.1 Introduction

The fusion of computational intelligence with control theory has given rise to the transformative field of intelligent control, representing a significant shift in automatic control systems. Inspired by biological systems, these intelligent control systems possess remarkable abilities to learn, adapt, and refine control strategies based on environmental cues. Utilizing linguistic descriptions reminiscent of human expertise, they demonstrate a deep understanding of their operational context. Furthermore, these systems are highly adjustable, enabling designers to optimize their performance according to predefined criteria. This convergence not only enhances control precision but also unlocks new possibilities for applications across a wide range of domains.

At its core, the integration of Fuzzy systems and Swarm and Evolutionary optimization techniques has inaugurated a new era in industrial automation and control. These intelligent control systems excel in modeling and managing nonlinear and time-varying systems, offering capabilities for fault detection and tolerance.

In recent years, fractional order control systems have garnered increasing attention within the control community. Governed by fractional order derivatives and integrals, these systems represent infinite order linear operators, extending beyond the confines of traditional integer order concepts in control and refining existing methodologies. Consequently, both fractional calculus and control systems have been harnessed to augment the performance of established control theories.

It's worth noting that hybrid intelligent control techniques have faced criticism for their perceived lack of mathematical rigor, particularly concerning guaranteed stability and insight when compared to linear control systems. However, the integration of computational intelligence with fractional systems presents an opportunity to address these concerns and achieve performance enhancements in control systems.

In this chapter, the traditional integer-order fuzzy Proportional-Integral-Derivative (PID) controller has been extended to incorporate fractional order derivatives and integrals. This enhanced controller operates based on the closed-loop error and its fractional derivative as inputs, with a fractional integrator in its output. Additionally,

various fractional variants of the integer-order fuzzy logic controller are briefly introduced.

The fractional order differ-integrations within the proposed fuzzy logic controller (FLC) are considered as design variables, alongside the input-output scaling factors (SF), and optimized using a Genetic Algorithm (GA). The optimization process aims to minimize several integral error indices, along with the control signal serving as the objective function.

Our first study, titled "Enhanced Control of Doubly Fed Induction Generator Based Wind Turbine System Using Fractional-Order Fuzzy PD+I Regulator," was published in the Journal Européen des Systèmes Automatisés (Volume 57, Issue 1, Pages 211-223, February 2024)

iieta.org

In Our paper [96], we introduced an innovative control strategy employing a fractional-order fuzzy PD+I (FO Fuzzy PD+I) regulator, optimized using the Social Spider Optimizer (SSO) algorithm. This approach marked a significant advancement in DFIG control compared to existing methods that rely on traditional PI regulators. The proposed FO Fuzzy PD+I regulator leverages the combined strengths of fuzzy logic and fractional-order control, resulting in superior performance and robustness in DFIG current control.

5.1.1 Introduction to fuzzy logic

Fuzzy logic, stemming from set theory and pioneered by Lotfi Zadeh in the 1960s [63], serves to handle uncertain and imprecise knowledge, providing a practical albeit approximate method to describe the behavior of complex or ambiguously defined systems. Unlike traditional Boolean logic, which deals in strict true-or-false terms, fuzzy logic operates with gradual instructions. It seeks to integrate human reasoning and knowledge into decision-making processes. Consequently, it offers an effective approach to modeling the behavior of intricate systems that defy precise modeling. This leads to the development of controllers capable of making intelligent control decisions. Within this thesis, we introduce Type I fuzzy logic as a tool for crafting intelligent controllers.

Given the extensive mathematical groundwork laid out in the literature, we've opted for an intuitive portrayal of fuzzy logic. For instance, accurately expressing concepts like "weak current" proves challenging. Thus, we establish thresholds to assign qualitative labels to variables based on their relation to these thresholds. This allows for the identification of qualitative classes or sets such as "weak," "moderate," or "strong" for the variable representing current. We then determine the degree of membership, represented by μ, of the current variable within these sets. In Boolean logic, the degree of membership μ for the current variable is limited to only two values: 0 and 1.

- Weak Current: "weak" = 1, "moderate" = 0, "strong" = 0.
- Moderate Current: "weak" = 0, "moderate" = 1, "strong" = 0.
- Strong Current: "weak" = 0, "moderate" = 0, "strong" = 1.

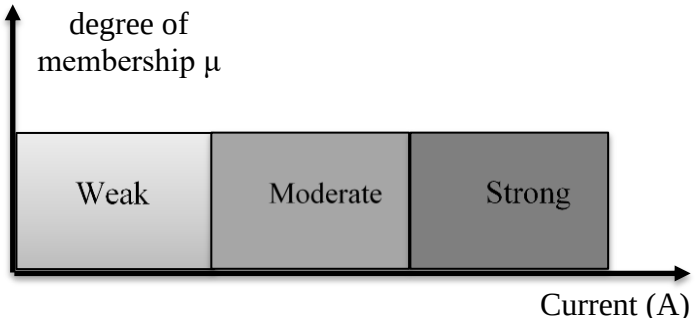

Figure 5-1 Schema defining a universe of discourse in Boolean logic

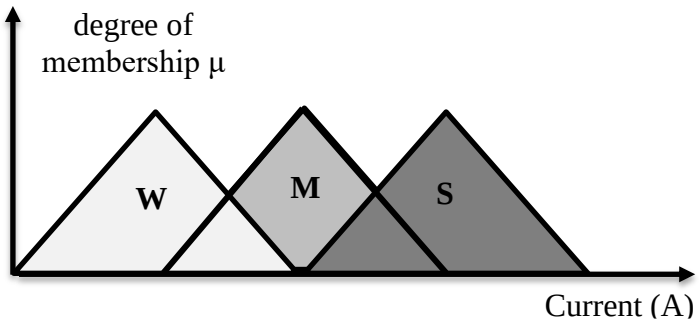

Figure 5-2 Schema defining a universe of discourse in fuzzy logic

In fuzzy logic, the degree of membership takes intermediate values when a variable belongs to two adjacent sets with different degrees or levels. This helps avoid abrupt

transitions between different classes, unlike in Boolean logic (see Figure 5-1). Indeed, it would be illogical to consider a current of 20 A as strong while a current of 19.8 A is not. The example we've just seen clearly illustrates that Boolean logic can be overly restrictive in certain cases, highlighting the need to turn to a more adaptable and flexible alternative, which could be an extension of the former. Enter fuzzy logic. When it comes to controlling any given process, fuzzy logic provides a foundational approach compared to classical control theory. In conventional control theory, processes are typically modeled using a set of differential equations or, at the very least, analytical relationships. However, this modeling approach can be challenging or even impossible in cases where the processes to be controlled are complex and/or nonlinear. Consequently, the complexity of controlling these systems significantly increases. The solution lies in adopting a control approach that focuses on how to control rather than on the system itself. This is known as the "black box" approach. Here, one can rely on a human expert who controls a device through rules that naturally integrate imprecisions and uncertainties [64]. This is the essence of fuzzy logic, which enables overcoming the challenges associated with modeling the systems to be controlled and the various uncertainties inherent in their operation.

In recent years, numerous applications employing fuzzy logic have emerged, including the control of industrial systems for which either mathematical models are lacking or are highly nonlinear [65].

Fuzzy logic-based control has been selected for governing various components of wind energy systems, known for their highly nonlinear nature. FLC have been favored due to their numerous advantages, such as simple control mechanisms, low cost, and the ability to design without exact knowledge of the mathematical model of the process. Typically, stabilizing electrical grids is achieved through methods designed on a nonlinear approach. Although electrical grid models are linearized around a nominal operating point, providing optimal performance around that point, electrical grids are generally nonlinear, and their operational conditions can vary widely. Thus, conventional stabilization approaches may not deliver optimal performance across the entire operational range. Moreover, the architectures of electrical grids are becoming increasingly complex, with the emergence of new paradigms such as smart grids,

rendering the classical approach obsolete [30]. To address these challenges, numerous adaptive controllers employing self-adjusting techniques for their parameters have been proposed. However, these controllers tend to be computationally intensive, requiring longer processing times [66].

Fuzzy logic incorporates an alternative approach that enables modeling complex systems using a higher level of expertise derived from accumulated knowledge and experience. It allows for expressing knowledge through subjective concepts like "very large," "too small," "moderate," etc., which are mapped under well-defined rules. A FLC employs fuzzy logic as a design approach that can be applied to develop both linear and/or nonlinear systems for integrated control [67]. The general foundations of fuzzy logic can be defined as follows[68]:

- Linguistic variables: These are variables that are described using linguistic terms or labels rather than precise numerical values.
- Determination of linguistic variables: This involves defining and identifying the linguistic terms or labels that will be used to describe the variables in the system.
- Fuzzy operators: These are operators used to perform operations on fuzzy sets, such as AND, OR, NOT, etc., which differ from their Boolean counterparts due to their handling of uncertainty.
- Determination of membership functions: Membership functions define the degree of membership of an element in a fuzzy set, mapping input values to membership degrees in the range [0, 1].
- Strategic allocation of the universe of discourse: This involves strategically dividing the range of possible input values into appropriate linguistic terms or labels to ensure effective representation and reasoning.
- Fuzzy reasoning: Fuzzy reasoning involves making decisions or drawing conclusions based on fuzzy logic principles, considering uncertain or imprecise information represented by linguistic variables and fuzzy sets.

5.1.2 Design of the fuzzy controller

Fuzzy logic is based on several key actions: first, the fuzzification of the input variables of the fuzzy controller, followed by the deduction of appropriate control decisions based on rule bases and inference system, Finally, the output of the FLC involves decision-making through the defuzzification of fuzzy values. Thus, the primary design processes of the FLC presented in Figure 5-3

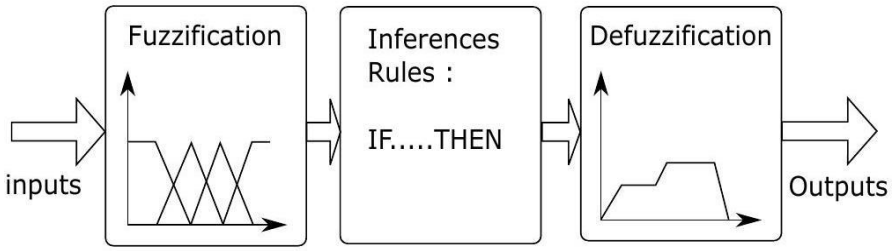

Figure 5-3 Block diagram of fuzzy control

5.1.2.1 Fuzzification Phase

The fuzzification phase involves defining membership functions for the different linguistic variables. Indeed, it is necessary to convert the input physical quantities, after normalization, into linguistic variables, which are semantic rules defined by an expert operator. This allows for a better classification of these physical quantities over the fuzzy sets defining this variable. This action enables a more precise determination of the degree of membership of the input variable based on the actual value, relative to each fuzzy set. Typically, the FLC receives, as input variables, the error between the output of the process to be controlled and the reference signal, as well as the rate of change of this error [61], [66]. The control law of a controller can be represented by the following figure:

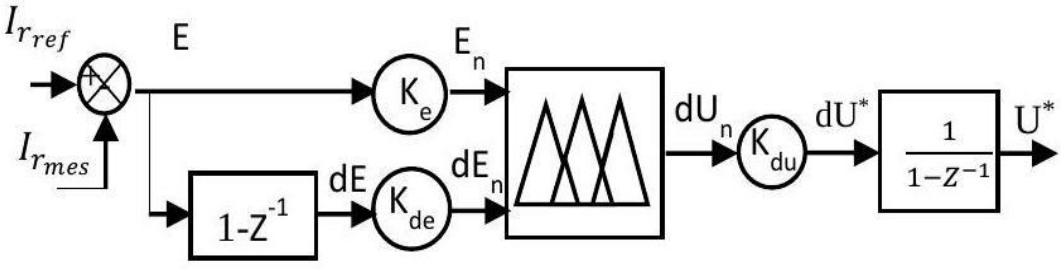

Figure 5-4 Schematic diagram of a fuzzy controller

There are no clear rules for choosing the number of fuzzy sets, the type of membership functions, and the partitioning of the universe of discourse for each variable [69]. Often, using more than seven fuzzy sets does not improve the performance of a fuzzy controller in terms of dynamics [69].

5.1.2.2 Inference Phase

Fuzzy inference is a fuzzy relation defined between two subsets. It involves "if... then" rules that are established based on expert human knowledge. The intersection of multiple preceding rules is calculated using a t-norm operator, while the union of several rules is calculated using a t-conorm operator [70]. The definition of the relation can theoretically involve any fuzzy operator. The establishment of the inference table is based on a qualitative analysis of the system's operation. Generally, fuzzy inferences defined by Mamdani and Sugeno are the most commonly used:

- Max-Min Inference Method (Mamdani method)
- Max-Product Inference Method
- Sum-Product Inference Method

5.1.2.3 Defuzzification Phase

Defuzzification, the final step in the design of a fuzzy controller, involves converting the inference result, which is a membership function, into a physical output quantity. There are several methods for defuzzifying fuzzy controllers [69],[70]:

- Defuzzification by centroid
- Defuzzification by maximum center
- Defuzzification by maximum value

Thus, with the centroid method being the most commonly used in the literature, the output value of the fuzzy controller at time k can be expressed as follows [69]:

$$y_k = \frac{\int x\mu_R(x)dx}{\int \mu_R(x)dx} \qquad 5\text{-}1)$$

Where x is the fuzzy variable, and $\mu_R(x)$ is the degree of membership of x in the fuzzy set R.

5.1.3 Fuzzy logic for rotor currents controller

Figure 5-5 depicts the block diagram illustrating the integration of fuzzy controllers within the inner loop of the vector control block of DFIG, replacing conventional PI controllers. Notably, both active and reactive powers are autonomously regulated, each employing its dedicated fuzzy controller.

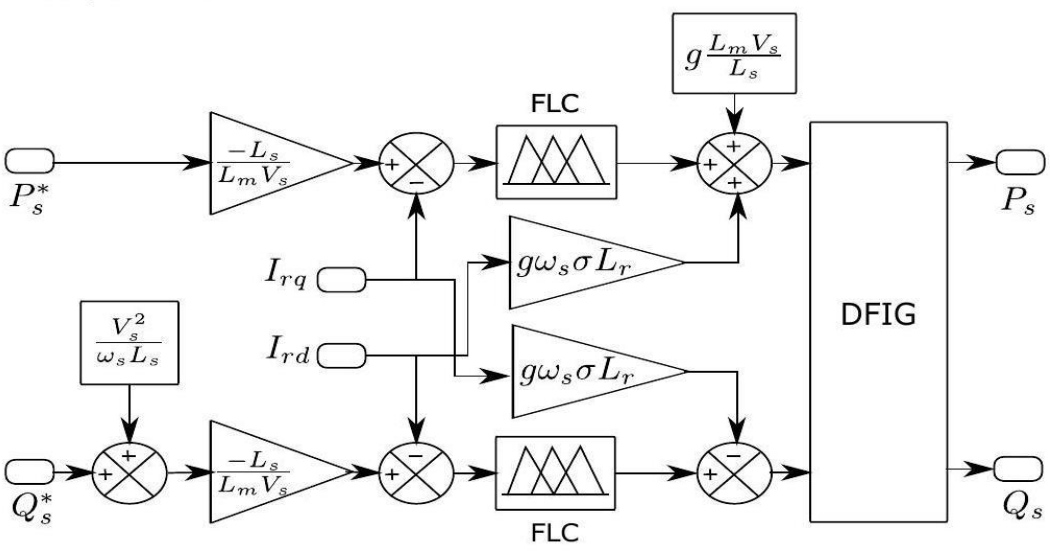

Figure 5-5 Fuzzy control of DFIG

The simplified block diagram of the control strategy, (FLC), is presented in Figure 5-6, this control scheme employs the error $e(t)$ between the rotor current reference and the actual rotor current, alongside the rate of change of this error, *de(t)*, as input variables. The controller's output is the rotor voltage. Essentially, the controller monitors the error signal and its derivative within the direct and quadrature rotor current components control loops. Based on this analysis, the controller adjusts the output signal U to align the rotor current with its reference value.

Normalization of both the error signal and its derivative is achieved using respective scaling factors K_e and K_{de}. The control output signal, U, is calculated by multiplying the rate of change of u with respect to time, du/dt, by the output scale factor K_{du}. This outcome is then integrated to generate the control command signal.

It's worth noting that the membership function utilized for this controller is the triangular function, and the center of gravity method is employed for defuzzification.

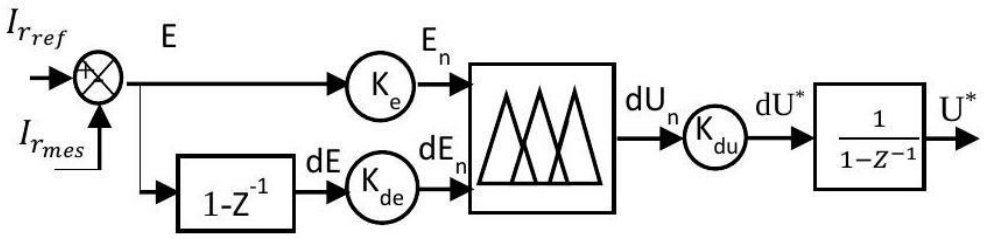

Figure 5-6 The proposed fuzzy current controller

The linguistic terms used for input-output membership functions are labeled as follows:

(negative big) NB, (negative medium) NM, (negative small) NS, (zero) Z, (positive small) PS, (positive medium) PM and (positive big) PB. Table 3 presents the fuzzy inference rules, there are 49 rules that form the knowledge repository of the FLC which are used to decide the appropriate control action. A sample rule of the FLC can be written as: **if** (e_i is P) **AND** (de_i is Z) **then** ($U_{\mathrm{r-ref}}$ is P).

In order to enhance the performance of the FLC, an empirical analysis is adopted to define the scaling factors and an appropriate distribution of universes of discourse that is identical for both inputs and output. Figure 5-7 illustrates the membership functions for both the input and output variables.

*Table*3 *Fuzzy inference rules.*

e	*de*						
	PB	PM	PS	Z	NS	NM	NB
PB	PB	PB	PB	PB	PM	PS	Z
PM	PB	PB	PB	PM	PS	Z	NS
PS	PB	PB	PM	PS	Z	NS	NM
Z	PB	PM	PM	Z	NM	NM	NB
NS	PM	PS	Z	NS	NM	NB	NB
NM	PS	Z	NS	NM	NB	NB	NB
NB	Z	NS	NM	NB	NB	NB	NB

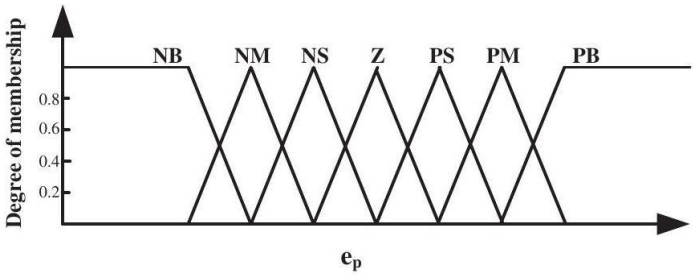

Figure 5-7 Membership functions

5.2 Introduction to Fractional Order Fuzzy PID Controller

5.2.1 Fractional Order Calculus

Fractional calculus is an advanced mathematical field that extends the concepts of differentiation and integration to non-integer (fractional) orders. The fundamental operator in this field is denoted as $a\ {}_aD_b^{\alpha}$, where a and b are the lower and upper bounds of the operation, and $\alpha\alpha$ represents the order of differentiation or integration, which can be any real number ($\alpha \in R$) [71], [72]. In this framework, ${}_aD_b^{\alpha}$ serves as a versatile operator that can represent both fractional derivatives and fractional integrals, providing a unified approach to a variety of complex mathematical problems. This notation effectively bridges the gap between integer-order calculus and the broader spectrum of operations allowed by fractional orders. The formal definition of ${}_aD_b^{\alpha}$ In this framework $b\alpha$ encompasses the following:

$$aD_b^{\alpha} = \begin{cases} \frac{d^{\alpha}}{dt^{\alpha}} & R(\alpha) > 0 \\ 1 & R(\alpha) = 0 \\ \int_a^b (dt)^{-\alpha} & R(\alpha) < 0 \end{cases} \qquad (5\text{-}2)$$

There are several mathematical definitions for fractional order integration and differentiation. These definitions do not always lead to identical results, but they are equivalent for a wide range of functions. Among these definitions, we can cite the three most common ones [73]:

1. Riemann-Liouville definition
2. Grundwald-Letnikov (G-L) definition
3. Caputo definition

However, we will limit ourselves to the most common definition, which is that of Riemann-Liouville, it is utilized in this thesis to implement the proposed control method as defined in the following equation for a function *f*(*t*):

$$aD_b^a f(t) = \frac{1}{\Gamma(m-a)} \frac{d^m}{dt^m} \int_a^b \frac{f(\tau)}{(t-\tau)^{a+1-m}} d\tau \quad (5\text{-}3)$$

where *m* is the integer part of *a*, *f*(*t*) is the applied function, and Γ is Euler's gamma function of *x*.

$$\Gamma(x) = \int_0^\infty e^{-t} t^{x-1} dt \quad (5\text{-}4)$$

where *a* is the order of integration, Γ(*a*) is the gamma function, and *f*(*x*) is the function to be integrated.

5.2.2 Fractional Order-based PID Regulator

PID controllers have been a cornerstone in industrial process control applications for several decades . Their enduring popularity stems from their straightforward design and reliable performance. PID controllers excel in delivering low percentage overshoot and short settling times, particularly in managing slow process plants .

The fractional PID controller represents an evolution of the classical PID controller. This advanced version incorporates the principles of fractional calculus, which allows for the tuning of both integral and derivative actions to fractional orders. This added flexibility enables fractional PID controllers to achieve even more precise control, enhancing performance in complex and variable process environments.

Fractional order controllers exhibit reduced sensitivity to parameter variations in both the controlled system and the controller itself. This robustness makes them particularly effective in maintaining consistent performance despite changes in system dynamics. Additionally, fractional order controllers can achieve the property of iso-damping with ease. Iso-damping ensures that the system's damping ratio remains constant across a range of frequencies, leading to improved stability and performance in dynamic environments [73].

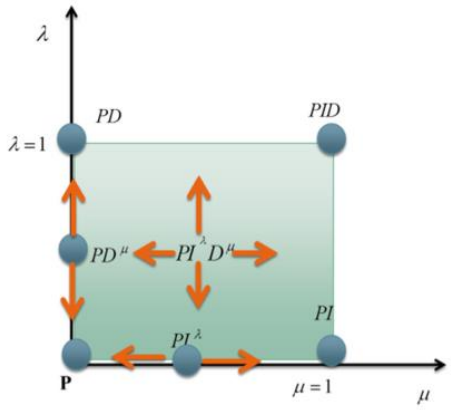

Figure 5-8 Fractional PID controller converge

The generalized transfer function of a fractional PID controller is expressed as:

$$C(s) = \frac{U(s)}{E(s)} = K_P + \frac{K_I}{s^{\lambda}} + K_D S^{\mu}, (\lambda, \mu \geq 0) \qquad (5\text{-}5)$$

were,

- $C(s)$ $The\ controller\ output$
- $U(s)$ $The\ control\ signal$
- $E(s)$ $The\ error\ signal$
- K_P $The\ proportional\ gain$
- K_I $The\ integration\ gain$
- K_D $The\ derivative\ gain$
- $\lambda\ the\ order\ of\ the\ differentiator$ is,
- $\mu\ the\ order\ of\ differentiator$

Classical PID controllers are special cases of the fractional PID controller, where the parameters λ and μ are both equal to one (refer to Figure 5-8). This means that, in the PID plane, instead of being limited to four fixed points, one can move continuously across the entire plane. Typically, the fractional order parameters range from 0 to 2. In this context,

$$\begin{cases} If\ \lambda = 1\ and\ \mu = 1, then\ it\ is\ PID\ controller \\ If\ \lambda = 0\ and\ \mu = 1, then\ it\ is\ PD\ controller \\ If\ \lambda = 1\ and\ \mu = 0, then\ it\ PI\ controller \\ If\ \lambda = 0\ and\ \mu = 0, then\ it\ is\ P\ controller \end{cases}$$

In a fractional-order proportional integral derivative (FOPID) controller, the integral (I) and derivative (D) operations are typically of fractional order. This means that, in addition to configuring the proportional, integral, and derivative constants (K_P, K_I, K_D), it is also necessary to set two additional parameters: the order of fractional integration (λ) and the order of fractional differentiation (μ). Optimizing these parameters K_P, K_I, K_D, λ and μ to meet specific user requirements for a given process involves a complex parameter optimization in a five-dimensional hyperspace.

Figure 5-9 illustrates the general structure of a closed-loop system incorporating a fractional PID controller. Unlike conventional PID controllers, fractional controllers feature two additional parameters, allowing for the fulfillment of two more specifications and thus enhancing the overall system performance. The $PI^{\lambda}D^{\mu}$controller is anticipated to further improve system performance. A primary challenge in the design of such controllers is tuning. Researchers have explored various tuning methods, including the modified Ziegler-Nichols method, particle swarm optimization, etc. [75],[76],[77].

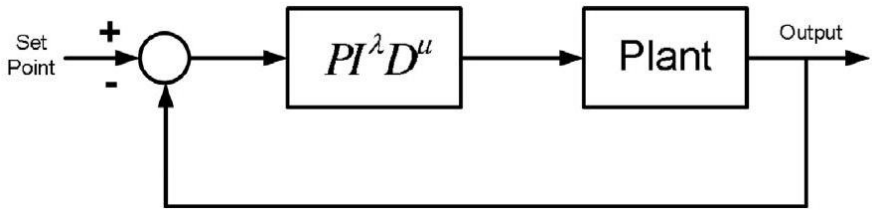

Figure 5-9 block diagram of fractional PID controller.

5.2.3 Structure of Fractional Order Fuzzy PID Controller

Recent studies have illuminated the potential benefits of merging FLC with fractional-order operators for integration and differentiation. This integration augments the system's degrees of freedom and introduces additional flexibility in crafting classical FLC-based PID regulators. The symbiosis between FLC and fractional-order operators leverages their individual strengths: FLC provides a robust mechanism for managing nonlinearities and uncertainties on a conceptual level, while fractional-order operators confer precise control over system dynamics, enabling more accurate modeling and control.

The amalgamation of FLC with fractional-order operators empowers the control system with heightened adaptability and resilience in uncertain environments. Fuzzy

logic excels in scenarios characterized by large uncertainties or ambiguous information, while fractional-order control adeptly captures subtle dynamics and optimizes control actions to attain desired performance levels. This synergy allows for a more nuanced and responsive control strategy that can navigate complex and dynamic systems effectively. [77].

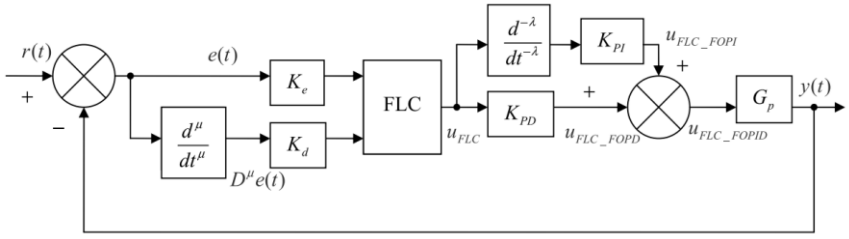

Figure 5-10 Structure of the fractional order fuzzy PID controller [75]

The fuzzy PID controller utilized in this study is a hybrid of fuzzy PI and fuzzy PD controllers, with K_e and K_d serving as input scaling factors (SFs), and and α (or K_{PD}) and β (or K_{PI}) as output SFs. In contrast to the original fuzzy PID controller, which employed error and its derivative as inputs, in this adaptation, the input includes the fractional order rate of the error (μ). Moreover, instead of a conventional integral term, a fractional order (λ) is applied at the output of the Fuzzy Logic Controller (FLC) to represent a fractional order summation (integration) of FLC outputs. This alteration enables a more nuanced control mechanism. The optimization process involves determining the values of these orders $\{\lambda, \mu\}$ and parameters $\{K_e, K_d, \alpha, \beta\}$ through a genetic algorithm. This method allows for fine-tuning the controller's performance for specific applications [78].

The control law of the scheme (Figure 5-11) is given as[75]:

$$u_{FLC\_FOPID}(t) = u_{FLC\_FOPI}(t) + u_{FLC\_FOPD}(t) \quad (5\text{-}6)$$

To facilitate performance comparison, a FOPID controller is included. This FOPID controller is configured in a non-interacting or parallel structure, characterized by its transfer function.

$$C^{FOPID}(s) = K_p + \frac{K_i}{s^{\lambda}} + K_d s^{\mu} \quad (5\text{-}7)$$

Other controller structures, such as the conventional integer order Fuzzy Logic Controller (FLC) and PID controller, can be derived by setting the values of $\{\lambda, \mu\} = 1$ in Figure 5-10 and Equation (5.6) respectively. There exist other Fractional Order (FO) fuzzy structures analogous to their integer order counterparts. Next, we will discuss the most prominent ones.

5.2.3.1 Fractional Order Fuzzy P+ID Controller

Figure 5-12 illustrates the structural layout, showcasing the incorporation of derivative action on the process output. This configuration ensures a smooth derivative response, mitigating the risk of a derivative kick when encountering sudden step changes in the set-point.

In process control contexts, abrupt shifts in error rate prompt significant adjustments in derivative action to counteract them effectively. By introducing fractional derivative action with parameters K_{d2} and μ_2 governing the feedback loop, and fractional integral action with parameters K_i and λ dictating the forward path, the system regulates the rate of change in the process variable and the evolution of the error signal with enhanced precision. This nuanced approach significantly enhances closed-loop performance, particularly in managing derivative kicks triggered by sudden set-point adjustments [79].

Moreover, this FLC structure maintains the fundamental simplicity of the conventional PID controller.

It supplements this simplicity with an additional fuzzy module for proportional action, offering ease of implementation in practical hardware Setups[75].

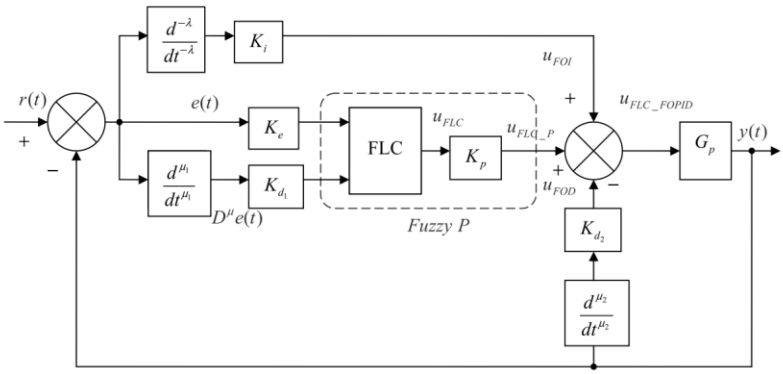

Figure 5-12 Schematic diagram of FO fuzzy P+ID controller [75]

The control law in this case is a combination of fuzzy P and conventional FO integral-derivative controller is given by:

$$u_{FLC\_FOPID}(t) = u_{F_{LC-P}}(t) + u_{FOI}(t) - u_{FOD}(t) \quad (5\text{-}8)$$

5.2.3.2 Fractional Order Fuzzy PI+D Controller

Figure 5-13 depicts the schematic of a Fuzzy Logic-based PI+D controller. In this configuration, the derivative action within the feedback path not only ensures smooth control response to sudden set-point changes but also provides nuanced compensation by integrating a first-order differentiator with parameter μ_2, offering enhanced flexibility [80].

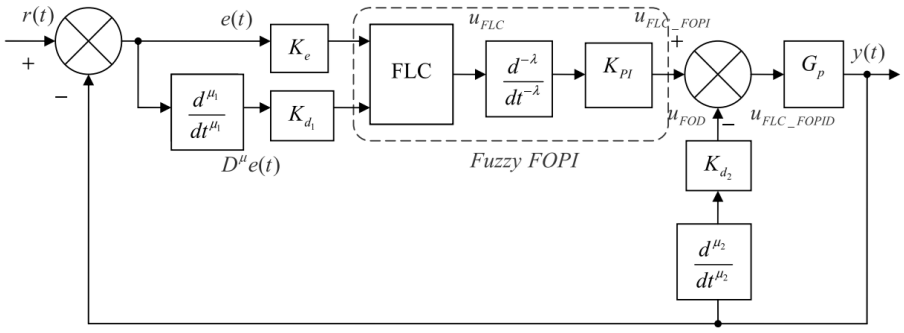

Figure 5-13 Schematic diagram of FO fuzzy PI+D controller [75]

The control law of such a controller is given as

$$u_{FLC\_FOPID}(t) = u_{FLC\_FOPI}(t) - u_{FOD}(t) \quad (5\text{-}9)$$

5.2.3.3 Fractional Order Fuzzy PD+I Controller

The schematic Figure 5-14 depicts a structure that combines FO fuzzy PD and FOPI controllers in parallel. Unlike previous approaches, where a single input FLC was utilized, this structure employs a rule base with two inputs, thus excluding integral action. This fuzzy PD+I configuration is an expansion of the parallel or noninteracting PID controller structure in the FO domain, wherein proportional and derivative actions are interconnected and fuzzified. In the proposed framework, this particular regulatory structure has been identified as the most effective solution among FO-Fuzzy configurations in prior applications [81].

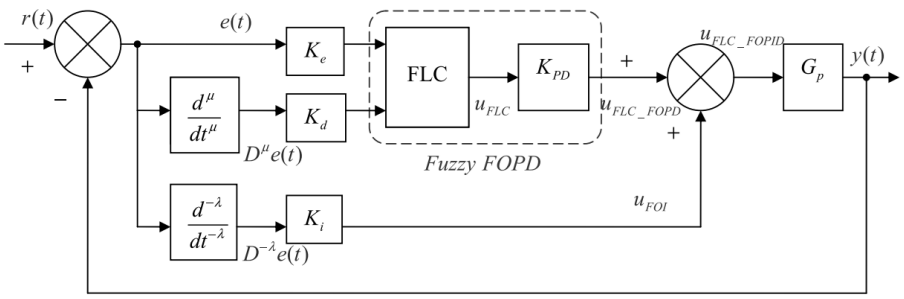

Figure 5-14 Schematic diagram of FO fuzzy PD+I controller

5.3 Fractional Order Fuzzy PD+I Controller for rotor currents controller

In Figure 5-15, the regulator structure of the Fractional Order Fuzzy PD+I Controller applied to the control of rotor currents is shown [96], where the transfer function of the DFIG is given by:

$$G(s) = \frac{1}{\sigma L_r s + R_r} \qquad (5\text{-}10)$$

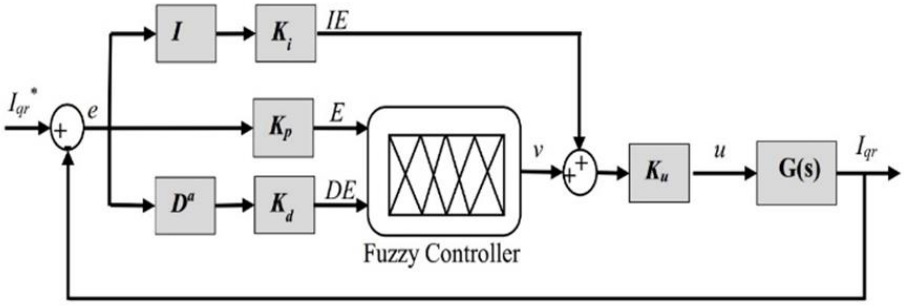

Figure 5-15 FO fuzzy PD+I controller for rotor current controller

The control law of the suggested FO Fuzzy PD+I regulator in time domain is given by:

$$U_{FOFuzzyPD+I}(t) = \begin{matrix} U_{FOFuzzyPD}(t).K_u + U_{FOI}(t).K_u \\ K_u.\left[f(K_p e, K_d D^a e) + K_i I e\right] \end{matrix} \qquad (5\text{-}11)$$

In this innovative variant of the Fractional Order (FO) Fuzzy PD+I regulator, the optimization variables crucial for calibration include the order (α) and scaling coefficients (K_i, K_p, K_d, K_u) . These variables are fine-tuned through the utilization of optimization algorithms. The proposed FO Fuzzy PD+I regulator incorporates a sophisticated two-dimensional linear rule base, detailed in Table 4, which encompasses parameters such as

error, fractional rate of error, and Fuzzy output [96]. This meticulously designed rule base is engineered to harness regular triangular membership functions, as depicted in Figure 5-16, and employs Mamdani type inferencing. This approach reflects a nuanced and comprehensive strategy for system control and regulation, emphasizing precision and adaptability in handling complex control tasks[96].

Table4 The fuzzy rule base

E/DE	NL	NM	NS	ZR	PS	PM	PL
NL	NL	NL	NL	NL	NM	NS	ZR
NM	NL	NL	NL	NM	NS	ZR	PS
NS	NL	NL	NM	NS	ZR	PS	PM
ZR	NL	NM	NS	ZR	PS	PM	PL
PS	NM	NS	ZR	PS	PM	PL	PL
PM	NS	ZR	PS	PM	PL	PL	PL
PL	ZR	PS	PM	PL	PL	PL	PL

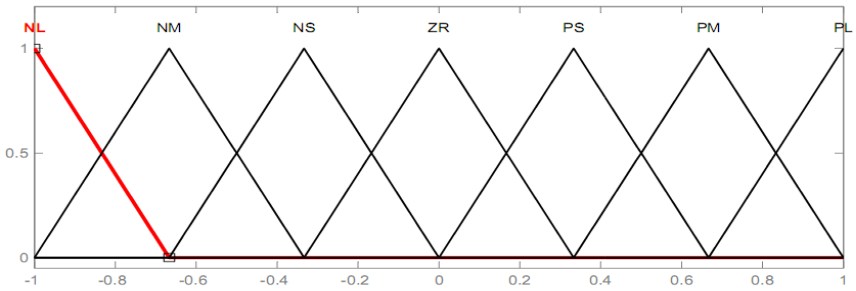

Figure 5-16 Membership functions for inputs and output

The fuzzy IF-THEN rules of FO Fuzzy PD+I regulator are written as follows:

$$\boldsymbol{R}^{(l)}: IF\ e\ \boldsymbol{is}\ A_1^l\ \boldsymbol{and}\ \dot{e}\ \boldsymbol{is}\ A_2^l\ \boldsymbol{THEN}\ y\ \boldsymbol{is}\ B_1^l$$

In this context, $A_1^l\ ,(i\ =\ 1,2)$ and B_1^l denote the linguistic variables corresponding to the inputs and output of the FLC. The parameter *l*, ranging from 1 to m, signifies the count of fuzzy IF-THEN rules. Seven triangular membership functions are applied to each input and output variable, resulting in a total of (7×7) rules, as detailed in Table 1. The linguistic variables are represented by the letters P, N, Z, S, M, and L, signifying Positive, Negative, Zero, Small, Medium, and Large, respectively.

For example, the primary rule derived from Table4 might be formulated as follows:

IF *DE* is equal *to PS* and *E* is equal to *ZR,* **THEN** *v* must be *PS*

IF the derivative of error (DE) is categorized as "Positive Small" (PS) and the error (E) is classified as "Zero" (ZR), THEN the resulting control output (ν) must be "Positive Small" (PS).

This rule outlines the control strategy's response to specific conditions, indicating that when the error derivative is categorized as "Positive Small" and the error itself is labeled as "Zero," the resultant output should also be "Positive Small." The crisp value obtained from the Fuzzy output is determined using the center of gravity (CoG) method during the defuzzification process [96].

In an effort to enhance the overall closed-loop performance of a DFIG-based Wind Turbine System, this study focuses on adjusting the fractional rate of error (α), while keeping the integrity of the rule base and the structure of membership functions unchanged. This targeted adjustment aims to fine-tune the system's response dynamics, ultimately optimizing its operational efficiency and stability.

5.4 Formulating Objective Functions

Performance evaluation of for $PI^{\lambda}D^{\mu}$ controllers encompass a spectrum of metrics, which can be classified into two primary categories. The first category encompasses discernible characteristics that can be directly extracted from the system's step response. These include fundamental parameters such as rise time, settling time, decay ratio, overshoot, and steady-state error [82].

These metrics provide valuable insights into the dynamic behavior and stability of the control system, offering tangible indicators of its performance.

In contrast, the second category comprises integral performance criteria, derived from the integration of the process error over time, hence termed as integral performance indices [83]. These metrics entail a more intricate computational process compared to those in the first category. However, they offer a more comprehensive evaluation of system performance by considering the entirety of error data throughout the response trajectory, rather than focusing solely on individual features.

The realm of PID controller integral performance assessment boasts four widely employed indices: Integral Absolute Error (IAE), Integral Squared Error (ISE), Integral

Time Absolute Error (ITAE), and Integral Time Squared Error (ITSE). All of these indices are further elaborated upon in [82], enriching the understanding of their computational methodologies and implications in benchmarking and optimizing control system performance, thereby facilitating informed decision-making in the realm of controller design and implementation.

Given that the error is integrated, a lower value signifies superior performance. The formulas for the most frequently employed performance indices are as follows:

$$IAE = \int_0^\infty |e(t)|dt \quad (5\text{-}12)$$

$$ISE = \int_0^\infty e(t)^2\, dt \quad (5\text{-}13)$$

$$ITAE = \int_0^\infty t \times |e(t)|dt \quad (5\text{-}14)$$

$$ITSE = \int_0^\infty t \times e(t)^2\, dt \quad (5\text{-}15)$$

Indeed, each integral performance index in control system design offers distinct advantages. For instance, the IAE index integrates the absolute values of measured errors without incorporating additional terms or multipliers. This approach ensures that errors with differing signs do not offset one another [82]. In the calculation of IAE, all errors over time carry equal weight, and the impact is linearly proportional to the magnitude of the error. Consequently, the timing of error occurrences does not influence the IAE index, and doubling the error magnitudes leads to a doubling of the IAE as well. Similarly, the ISE index is indifferent to time in determining performance value. However, since errors are squared, larger errors are accentuated. Consequently, tuning a $PI^\lambda D^\mu$ controller based on ISE tends to yield a smaller overshoot compared to IAE but may result in a longer settling time compared to time-weighted indices such as ITAE and ITSE [84].

The ITAE criterion aims to minimize the product of time and absolute error within a control system. By incorporating time into the error calculation, it emphasizes reducing errors later in the process, effectively diminishing settling time, a benefit not achievable with IAE or ISE approaches. Since ITAE accounts for absolute error, it also minimizes the maximum percentage of overshoot. Conversely, ITSE penalizes error even more than ITAE, leading to faster damping of oscillations. However, in scenarios of sudden set-point changes, ITSE-based controllers may demand larger outputs, posing challenges from an actuator design perspective compared to ITAE-based counterparts.

5.5 Optimization Algorithm Used for the Tuning of Optimal Controllers

In recent decades, Optimization Algorithms have surged in popularity for tackling real-world optimization challenges. This surge is largely due to the growing complexity of these problems, which frequently feature intricate nonlinear constraints, objective functions, and numerous decision variables. Unlike conventional methodologies, which can falter in the face of such intricacies, Optimization Algorithms offer simplicity and straightforward implementation. These algorithms come in various types, variants, and classifications, each crafted to address diverse engineering problems. They can generally be categorized into three main classes: Parameter search methods, Evolutionary algorithms, and Swarm Intelligence algorithms [90].

- **Parameter search methods:** Methods for searching parameters to optimize parameters across multiple dimensions, one can seek the optimal solution within the parameter space by exploring various combinations and evaluating their effectiveness. The prevalent approaches for hyperparameter optimization include Grid Search, Random Search, and Manual search [85]. While these techniques offer broad applicability to optimization challenges, they rely on trial-and-error, demanding substantial computational resources.

- **Evolutionary algorithms** are versatile optimization techniques inspired by natural evolution. They maintain a population of potential solutions to a problem, with each individual evaluated for fitness. The next generation is created based on the performance of the previous generation's solutions. Examples include genetic algorithms (GA) [86], bacterial foraging optimization (BFO), and biogeography-based optimization (BBO).

- **Swarm Intelligence** draws inspiration from collective behavior observed in nature. For instance, it leverages the dynamics of bee swarms [87], elephant herds [88], and other natural phenomena. Unlike evolutionary algorithms, swarm intelligence methods do not create new populations from existing ones. Instead, they guide the swarm towards optimal solutions by adjusting existing solutions. The process resembles evolutionary algorithms in that it evaluates the fitness of swarm solutions and iteratively refines them until certain termination conditions

are fulfilled. An example of a recent swarm intelligence method is Social spider optimizer (sso), which will be discussed in more depth .

Each class of algorithms has its own unique characteristics and strengths, making them suitable for different types of optimization problems.

5.5.1 Parameter optimization summary

The effectiveness of the optimization methods discussed earlier relies heavily on the unique attributes of the problem being addressed. For instance, in simpler optimization scenarios with unimodal fitness functions, greedy algorithms excel. They swiftly converge to the singular global optimum, showcasing high efficiency. However, the scenario alters when dealing with more complex, multi-modal functions. In such cases, where the fitness function's gradient is either unknown or fails to provide adequate direction toward the optimum, traditional gradient-based methods struggle. Instead, randomized or stochastic optimization techniques become the preferred option. These methods operate without the need for gradient calculations, making them better suited for navigating the complex and uncertain terrain of multi-modal functions [89].

Figure 5-17 serves as a visual representation of this dynamic. It underscores the notion that the appropriateness of a particular optimization method hinges on the nuanced interplay between the problem's properties and the strengths of the method itself. By understanding these relationships, practitioners can make more informed decisions when selecting the most suitable optimization approach for a given task [90].

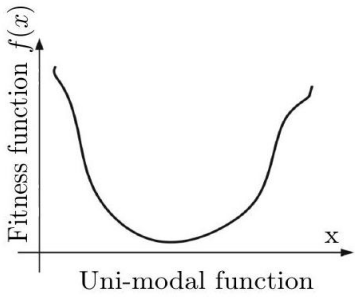

Figure 5-17 Examples of uni-modal and multi-modal functions

5.6 Social spider optimizer (SSO) for FO FUZZY PD+I regulator

The Social Spider Optimizer (SSO) presents a novel swarm optimization technique introduced by Cuevas et al. [42]. Drawing inspiration from the cooperative

behavior observed in social-spider colonies, this intelligent algorithm was meticulously crafted. Through extensive experimental evaluation across various system classes including higher-order plants, non-minimum systems, and dynamic fractional systems, the SSO method was compared against other evolutionary approaches such as GA, HS, PSO, and GSA. The results of these experiments consistently demonstrated the superior performance of the proposed SSO method in terms of solution accuracy and convergence.

Presently, numerous publications are dedicated to exploring modifications, enhancements, or applications of SSO for tackling diverse and complex optimization problems [91–95]. At the core of the SSO algorithm lies a sophisticated framework featuring two essential search agents: the social spiders and the communal web. These spiders are intricately categorized into distinct genders, establishing a structured hierarchy within the algorithm. Within the SSO methodology, the arrangement of each solution within the expansive search space mirrors the spatial organization of spiders within the communal web. Moreover, each spider is assigned a weighted significance, meticulously determined by the fitness value of the corresponding solution, as assessed by the discerning social spider.

The initialization phase of the SSO algorithm begins with the creation of a population, denoted as S, consisting of a collection of N spider locations representing diverse solutions. This diverse assembly encompasses both female (fi) and male (mi) spiders, thus encompassing the entire breadth of the search space.

Considering that female spiders typically make up a larger proportion than males in real spider societies (approximately 70-90%), we decided to randomly allocate the number of female spiders, denoted as *Nf*, to constitute approximately 85% of the total population, N [91]. Therefore, the flows equations are employed to calculate Nf and Nm:

$$N_f = floor\left[N.\left(0.9 - 0.25.rand(0.1)\right)\right] \quad (5\text{-}16)$$

In this context, "rand" denotes a randomly generated value ranging from 0 to 1, while "floor(.)" function converts a real number to the nearest integer value consequently, *N* elements compose the entire population .

In this context, the term "rand" represents a randomly generated value ranging from 0 to 1, while the "floor(.)" function converts a real number to the nearest integer value. As

a result, the entire population comprises N elements $S = \{s1, s2 \dots, sN\}$, which is then divided into the sub-groups male spiders $M = \{m1, m2, \dots, mNm\}$ and female spider$F = \{f1, f2, \dots, fNf\}$, such that:

$$S = \{s1 = f1, s2 = f2, \dots, sNf = fNf, sNf + 1 = m1, sNf + 2 = m2, sNf + 2 = m2, \dots, sN = mNm\}.$$

The female spider location fi is randomly initialized between the lower initial value p_j^{low} and the upper initial value p_j^{high} by using the following expression:

$$f_{i,j}^0 = p_j^{low} + \left(p_j^{high} - p_j^{low}\right).rand(0.1) \quad (5\text{-}17)$$

While the male spider location mi is randomly initialized as follows:

$$m_{k,j}^0 = p_j^{low} + rand(0.1).\left(p_j^{high} - p_j^{low}\right)$$
$$j = 1,2,..,n\ , i = 1,2,..,N_f, k = 1,2,\dots,N_m \quad (5\text{-}18)$$

Where "0" signifies the initial population, while "*j*", "*i*", and "*k*" denote individual indexes. The function rand(0, 1) generates a random value within the range of 0 to 1. " fi, jis " represents the j^{th} variable of the i^{th} female spider location. In the proposed SSO method, the weight of each spider (ω_i) reflects the quality of the corresponding solution within the population (S). ω_i is determined by the following equation:

$$\omega_i = \frac{J(s_i) - worst_s}{best_s - worst_s} \quad (5\text{-}19)$$

In this context, " $J(s_i)$ " represents the objective function or fitness value obtained by evaluating the spider location " s_i ".

Equation (5-19) is used to get the worst and best values (*worsts* and *bests*) by considering the following constrained optimization problem into account:

$$best_s = \min_{k\in\{1,\dots,N\}} J(s_k)\ and\ worst_s = \max_{k\in\{1,\dots,N\}} \quad (5\text{-}20)$$

Members of the colony interact through the communal web, exchanging information via small vibrations crucial for organizing all spiders collectively within the population. The transmission of these vibrations is influenced by both the weight and distance of the spider. The vibrations perceived by individual member i from member j are determined by flow equation :

$$V_i b_{i,j} = \omega_j . e^{-d_{i,j}^2} \quad (5\text{-}21)$$

where the $d_{i,j}$ is the Euclidean distance between the member i and j, such that $d_{i,j} = \|s_i - s_j\|$. There are three types of vibrations in the SSO approach [91]:

1.Vibrations $V_i bc_i$; It is feasible to depict the information (vibration) exchanged between individual $i(s_i)$ and member $c(s_c)$, which is the nearest member to individual i and possesses the greatest weight, as follows:

$$V_i bc_i = \omega_c . e^{-d_{i,c}^2} \quad (5\text{-}22)$$

2.Vibrations $V_i bb_i$; The information exchanged between the individual $i(s_i)$ and the best member $b(s_b)$ of the total population S may be described as:

$$V_i bb_i = \omega_b . e^{-d_{i,b}^2} \quad (5\text{-}23)$$

3.Vibrations $V_i bf_i$; The transmitted exchanged between the individual $i(s_i)$ and the nearest female individual $f(s_f)$ may be described as:

$$V_i bf_i = \omega_f . e^{-d_{i,f}^2} \quad (5\text{-}24)$$

At each iteration k, the female members update their position as follows:

$$f_i^{k+1} = \begin{cases} f_i^k + \rho . V_i bc_i . \left(s_c - f_i^k\right) + \tau . V_i bb_i . \left(s_b - f_i^k\right) \\ \quad +\delta . (rand - 0.5) with probability PF \\ f_i^k - \rho . V_i bc_i . \left(s_c - f_i^k\right) - \tau . V_i bb_i . \left(s_b - f_i^k\right) \\ \quad +\delta . (rand - 0.5) with probability 1 - PF \end{cases} \quad (5\text{-}25)$$

Where ρ, τ and δ are random numbers in [0, 1], whereas PF represents the probability threshold. Within the colony, male spiders are categorized into dominant (D) or nondominant (ND) members, and they are organized in descending order based on their weight values. The male member whose weight w_{Nf+m} falls in the middle is identified as the median male member. At each iteration k, the male members undergo positional adjustments according to the following protocol:

$$m_i^{k+1} = \begin{cases} m_i^k + \rho . V_i bf_i . \left(s_f - m_i^k\right) + \delta . (rand - 0.5); if \omega_{N_{f+i}} > \omega_{N_{f+m}} \\ m_i^k + \rho . \left(\frac{\sum_{h=1}^{N_m} m_h^k . \omega_{N_{f+h}}}{\sum_{h=1}^{N_m} \omega_{N_{f+h}}} - m_i^k \right); if \omega_{N_{f+i}} \leq \omega_{N_{f+m}} \end{cases} \quad (5\text{-}26)$$

where the members symbolize the nearest female member to the male member i.

After updating all female and male members, the final step involves the mating process. Here, the last operator facilitates collaboration between dominant male members and female members within a specific radius known as the mating radius, calculated by:

$$r = \frac{\sum_{j=1}^{n}\left(P_j^{high} - P_j^{low}\right)}{2.n} \qquad (5\text{-}27)$$

where n is the dimension of the problem, P_j^{high} and P_j^{low} are the upper and lower limits for a given dimension, respectively. It is obvious that the spider with the higher weight has the most influence on the new product. The SSO method determines the influence probability P_{si} of each member as the follows:

$$Ps_i = \frac{\omega_i}{\sum_{j \in T^k} \omega_j} \qquad (5\text{-}28)$$

where T^k stands for the group of individuals participating in the mating process and $j \in T^k$. To summarize the previous equations of the SSO approach, the following flowchart and Figure 5-17 illustrate the computational steps required to execute the SSO algorithm [91].

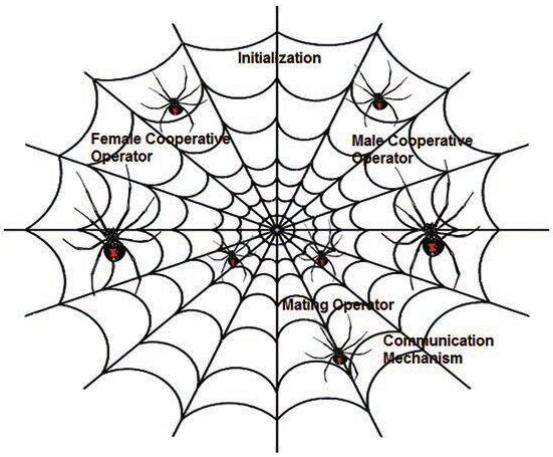

Figure 5-18 SSO algorithm process

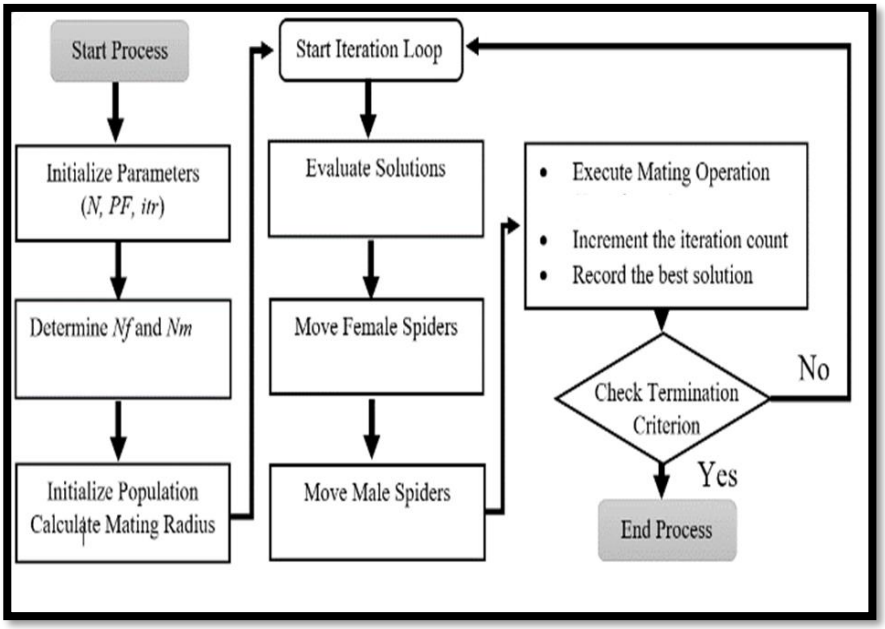

Figure 5-19 Flowchart of the considered SSO algorithm

5.7 Formulation of the Objective Functions for SSO algorithm

The FO Fuzzy PD+I regulator, comprising five parameters, serves as the SSO population within the DFIG-based WTS. The primary objective is twofold: first, to minimize current deviations (ΔI_{dr}, ΔI_{qr}), and second, to mitigate power fluctuations (ΔI_{dr}, ΔI_{qr}) amidst system uncertainties. This optimization task targets the parameters of the FO Fuzzy PD+I current regulator.

The performance evaluation metric utilized in this study is the ITAE. It quantifies the effectiveness of the FO Fuzzy PD+I current regulator and is expressed as:

$$\begin{aligned} ITEA &= \int_0^{T_{sim}} t|e(t)|dt \\ e(t) &= I^* - I_{real} \end{aligned} \qquad (5\text{-}29)$$

In Equation 5-29, *e(t)* symbolizes the closed-loop error, depicting the variance between the desired rotor current and the actual rotor current. T_{sim} denotes the simulation time. Thus, the formulation of the problem is outlined as follows:

$$\begin{aligned} &minimize \quad J(\alpha, K_p, K_d, K_i, K_u) = ITEA \\ &Subject\ to \quad \begin{cases} \alpha_{min} \le \alpha \le \alpha_{max} \\ K_{pmin} \le K_p \le K_{pmax} \\ K_{dmin} \le K_d \le K_{dmax} \\ K_{imin} \le K_i \le K_{imax} \\ K_{umin} \le K_u \le K_{umax} \end{cases} \end{aligned} \qquad (5\text{-}30)$$

where, max $and\ min$ are the limit values of each parameter. In the considered design method, $K_{pmin} = K_{dmin} = K_{imin} = K_{umin} = 0$ and $K_{pmax} = K_{dmax} = K_{imax} = K_{umax} = 20$. The values of $\alpha_{min} = 0\ and\ \alpha_{max} = 1$.

The choice of these limits was guided by prior knowledge and understanding of the model, driven by two key factors. Firstly, these limits guarantee that the optimized parameters remain within practical and viable ranges, preventing the discovery of solutions that are impractical or unrealistic. Secondly, they aid in restricting the search space for optimization algorithms, thereby promoting faster convergence and improving computational efficiency.

5.8 Simulation tests and results

After conducting simulation experiments, we evaluated the effectiveness and resilience of the proposed Fractional Order (FO) Fuzzy Proportional-Derivative with Integral (PD+I) controller. This section provides an in-depth comparison between the aforementioned FO Fuzzy PD+I controller, a fuzzy regulator, and a standard Proportional-Integral (PI) controller. These assessments were carried out via numerical simulations in the Matlab/Simulink™ environment, focusing on a grid-connected DFIG-based wind turbine system.

The evaluation of controller performance was divided into three scenarios. Initially, we analyzed the regulator's response to variations in active power, followed by an examination of its efficacy amidst fluctuating wind velocities. Lastly, sensitivity analysis was conducted to gauge the robustness of the proposed controller in the face of uncertainties regarding DFIG parameters. It is noteworthy that the DFIG under scrutiny in this study has a rated capacity of 2 MW (Table 5).

The optimized gain values for both the proposed FO Fuzzy PD+I controller and the traditional PI control scheme were obtained using the Social Spider Optimization (SSO) algorithm, as detailed in Table 6.

Table 5 Obtained optimum regulator parameters using SSO algorithm

Regulator coefficients	K_p	K_d	K_i	K_u	α
PI	0.57	0	4.59	-	-
FO Fuzzy PD+I	0.55	0.20	10.65	10.68	0.25

Table 6 Parameters of 2 MW DFIG [7].

Parameter	Symbol	Value
Stator Frequency (Hz)	f	60
Synchronous Speed (rev/min)	n	1500
Nominal Stator Three-Phase Active Power (MW)	P_s	2e6
Line-to-Line Nominal Stator Voltage (V)	V_s	690
Each Phase Nominal Stator Current (Amp)	I_s	1760
Nominal Torque at Generator/Motor Modes (N.m)	T_{em}	12732
Stator Connection		Star
Pole Pair	p	2
Line-to-Line Nominal Rotor Voltage (V)	V_r	2070
Rotor Connection		Star
Stator/Rotor Turns Ratio	u	0.34
Stator Resistance (mΩ)	R_s	2.6e-3
Stator Leakage Inductance (μH)	L_{si}	87e-6
Magnetizing Inductance (mH)	L_m	2.5e-3
Rotor Resistance (mΩ)	R_{res}	26.1e-3
Rotor Leakage Inductance (μH)	R_{ind}	783e-6
Rotor Resistance Referred to Stator (mΩ)	R_r	2.9e-3
Rotor Leakage Inductance Referred to Stator (μH)	L_{sr}	87e-6
Stator Inductance (mH)	L_s	$L_m + L_{si}$
Rotor Inductance (mH)	Lr	$L_m + L_{sr}$

5.8.1 Scenario 1:

In the initial scenario, aimed at scrutinizing the performance of the two optimized regulators alongside the Fuzzy regulator, reference tracking was conducted by imposing stator active power steps onto DFIG. Concurrently, stator reactive power was kept at zero to maintain unity power factor (PF) at the grid interface. The control system utilized the same optimal gains as determined in the previous section, excluding the MPPT controller and the Wind Turbine System (WTS), while DFIG parameters were set to their rated values.

In this scenario, the stator active power variations included in the DFIG were as follows: -1 MW at time instant $t \leq 3s$ and -1.3 MW at time instant $3s \leq t \leq 6s$. The outcomes derived from this scenario are depicted in Figure 5-20. Figure 5-19 illustrates a notable improvement in the stability of stator active power with the optimized FO Fuzzy PD+I regulator compared to both the optimized PI and Fuzzy regulators when the DFIG experiences variations in stator active power. Moreover, under such conditions, the DFIG's active power precisely follows its reference and achieves faster settling times with the FO Fuzzy PD+I regulator than with the PI and Fuzzy regulator.

Table 7 succinctly summarizes the dynamic effects observed in the Doubly-Fed Induction Generator (DFIG) system concerning changes in stator active power. Performance metrics including rising time (RT), maximum overshoot (MO), steady-state error (SSE), settling time (ST), and Integral of Time-weighted Absolute Error (ITAE) are utilized to characterize these outcomes. Remarkably, the results demonstrate that both the Fuzzy controller and the optimized Fractional Order (FO) Fuzzy Proportional-Derivative with Integral (PD+I) controller achieve the lowest values across all mentioned metrics.

Comparatively, employing the optimized FO Fuzzy PD+I regulator significantly enhances stator active power responses, as evidenced by improved RT, MO, SSE, and ST parameters when contrasted with the optimized Proportional-Integral (PI) controller and the Fuzzy regulator.

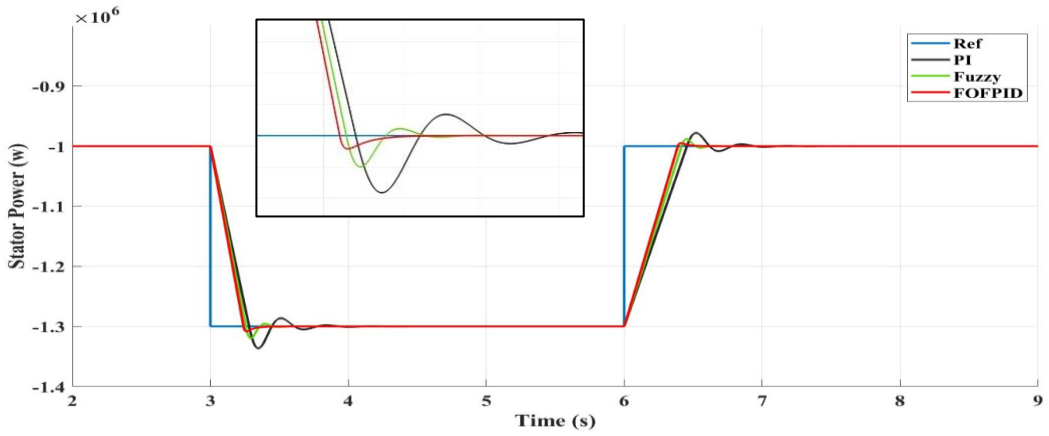

Figure 5-20 DFIG stator active power

Table 7 Performance of optimized PI and FO Fuzzy PD+I regulators

Regulator type	*RT* (s)	*MO* (%)	*SSE* (%)	*ST* (s)
PI	1.1	2.5	1.2	2.3
FO Fuzzy PD+I	0.9	1	0	1.22
Fuzzy	1.0	1.5	0.2	1.83

5.8.2 Scenario 2:

In this scenario, the DFIG system operates smoothly under nominal parameter values, devoid of external disturbances or parameter fluctuations. The Wind Turbine System (WTS), coupled with Maximum Power Point Tracking (MPPT) technology, generates the reference signal for the DFIG's active power. Figure 5-21 illustrates a sudden change in

wind velocity, rising from 8 meters per second to 10 meters per second, then descending back to 8 meters per second. This wind velocity profile distinctly delineates the sub-synchronous and upper-synchronous operational modes.

we present the responses of critical variables, such as rotor speed in Figure 5-22 (radians per second), stator active power in Figure 5-23 (watts), rotor currents in Figure 5-24 (amperes), and stator currents in Figure 5-25 (amperes). These responses are influenced by the utilization of the optimized Fractional Order (FO) Fuzzy Proportional-Derivative with Integral (PD+I) controller, the optimized Proportional-Integral (PI) controller, and the Fuzzy controller, respectively. The optimal rotor speeds required to achieve the desired DFIG active power levels are 1250 and 1550 revolutions per minute (rpm), correspondingly.

When employing the optimized FO Fuzzy PD+I controller, the measured results exhibit remarkable precision in tracking the reference signals for the DFIG's active power, closely followed by the Fuzzy controller. Moreover, the optimized FO Fuzzy PD+I regulator effectively minimizes ripple content compared to the outcomes obtained with the optimized PI controller and Fuzzy regulator.

Similarly, provides the Total Harmonic Distortion (THD) analyses of stator current for the three control cases: the suggested control (Figure 5-26), conventional PI control (Figure 5-27), and Fuzzy control (Figure 5-28), respectively. From these results, it's evident that the THD analyses of stator current for the optimized FO Fuzzy PD+I regulator are 0.59%, lower than the 0.83% for the Fuzzy regulator. Thus, the suggested FO Fuzzy PD+I regulator can offer better current quality than Fuzzy and traditional PI methods. The THD of stator current decreased with an improvement ratio of about 28.96% with the optimized FO Fuzzy PD+I regulator.

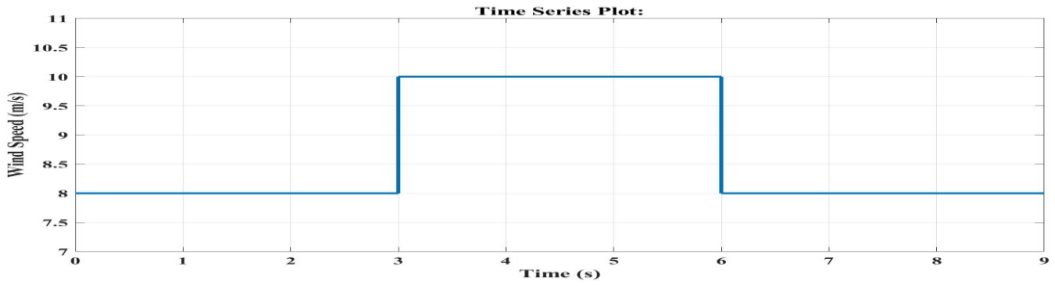

Figure 5-21 Wind speed

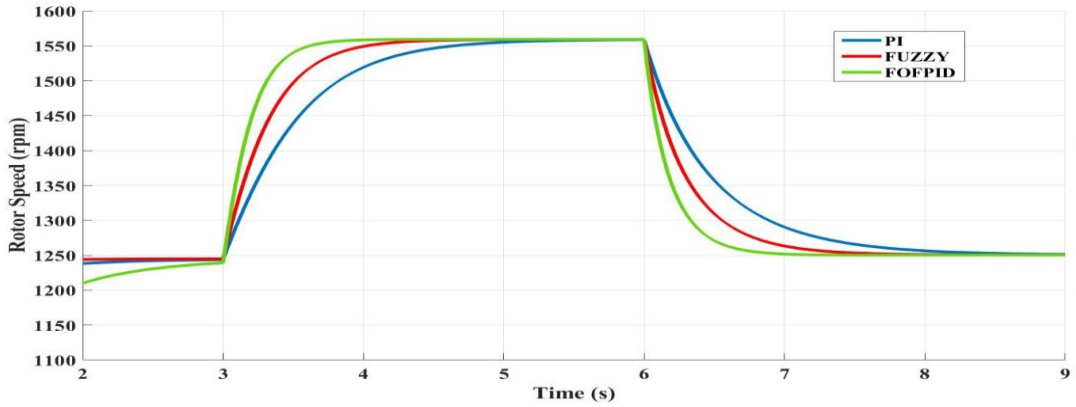

Figure 5-22 Rotor speed

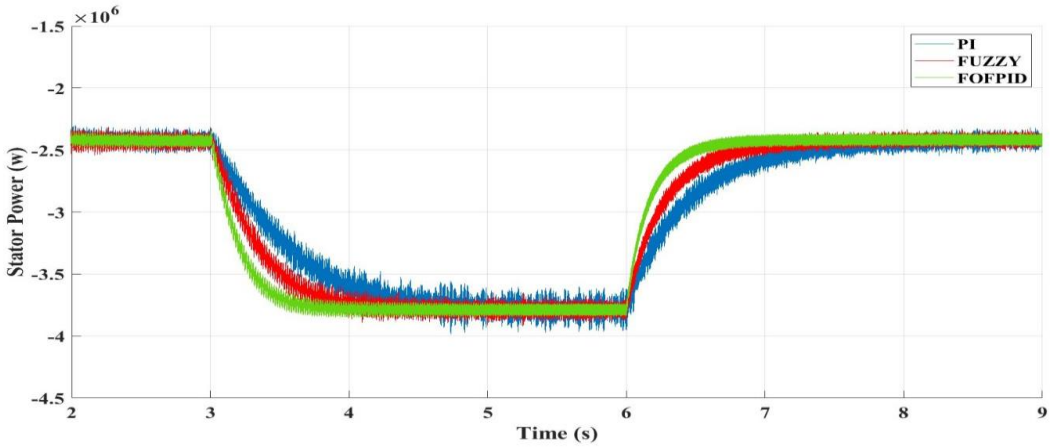

Figure 5-23 Stator active power

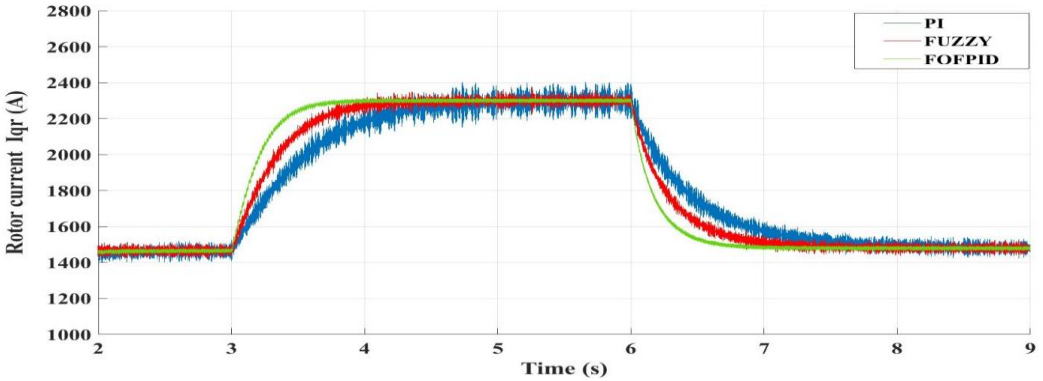

Figure 5-24 Rotor currents Iqr

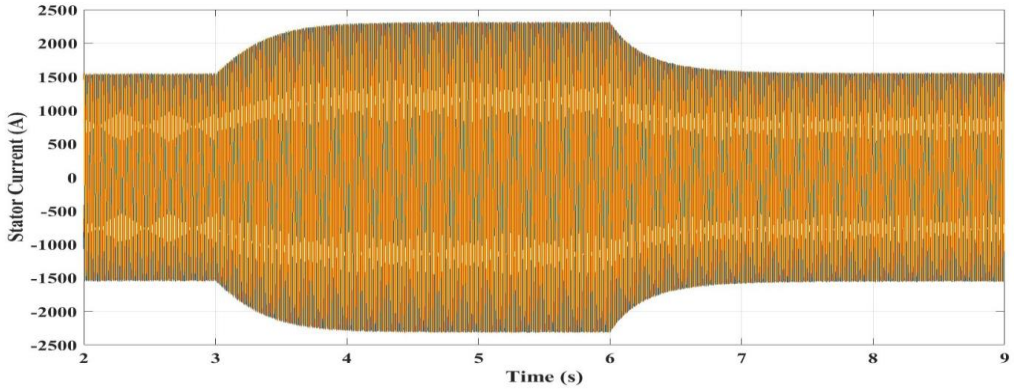

Figure 5-25 Stator current

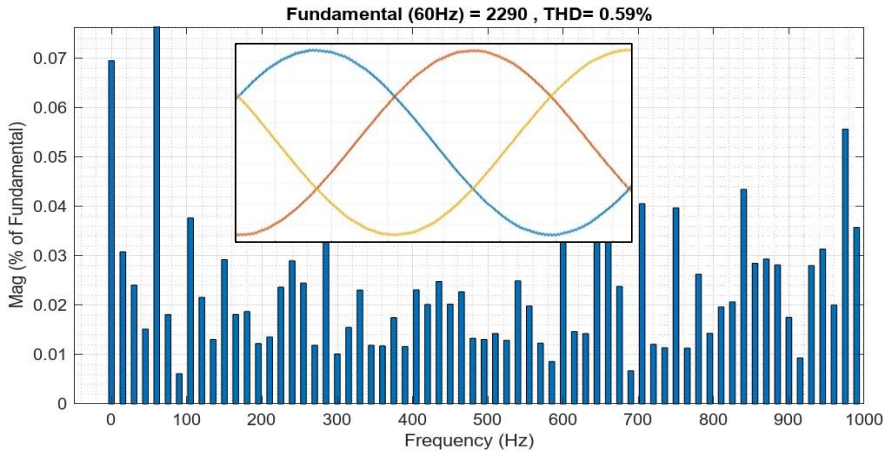

Figure 5-26 THD analyses for suggested regulator

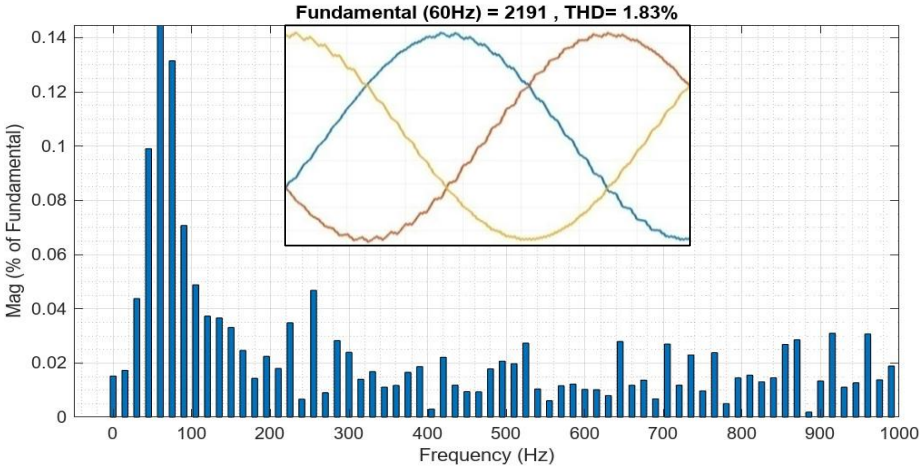

Figure 5-27 THD analyses for PI regulator

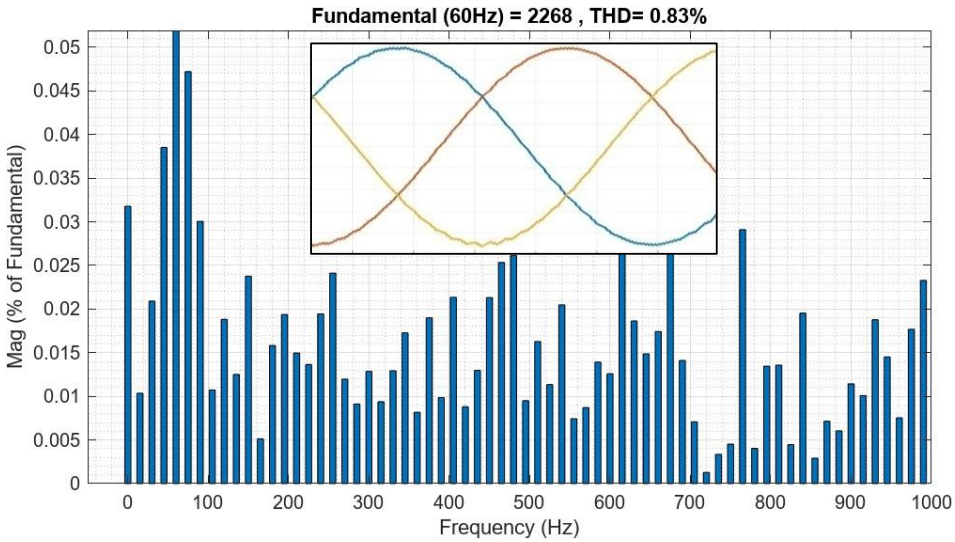

Figure 5-28 THD analyses for FUZZY regulator

5.8.3 Scenario 3

Scenario 3 introduces the system to unpredictable wind velocity conditions, as depicted in the wind velocity profile illustrated in Figure 5-30. Performance characteristics of mechanical rotor speed are shown in Figure 5-31, stator active power in Figure 5-32 Figure 5-31, active rotor current (Iqr) in Figure 5-33 and three-phase rotor currents in Figure 5-34. These metrics are assessed under three distinct scenarios, each employing a different control strategy: optimized Proportional-Integral (PI), optimized Fractional Order (FO) Fuzzy Proportional-Derivative with Integral (PD+I), and Fuzzy regulator.

Figure 5-31 assesses the performance of rotational speed tracking. Notably, the optimized PI regulator exhibits slower response and significant tracking inaccuracies. In contrast, the optimized FO Fuzzy PD+I regulator demonstrates nearly flawless behavior in tracking the desired rotational speed.

Figure 5-32 illustrates the stator active power tracking performance. A comparison among the optimized FO Fuzzy PD+I regulator, optimized PI regulator, and Fuzzy regulator indicates that the optimized FO Fuzzy PD+I regulator effectively achieves the stator active power tracking objectives.

Figure 5-33 and Figure 5-29 examines the control of active rotor current. The results indicate that the responses of the Fuzzy and optimized PI regulators oscillate, deviating

from the desired active rotor current. This underscores the superior performance and resilience of the proposed optimized FO Fuzzy PD+I regulator in handling unpredictable wind velocity scenarios.

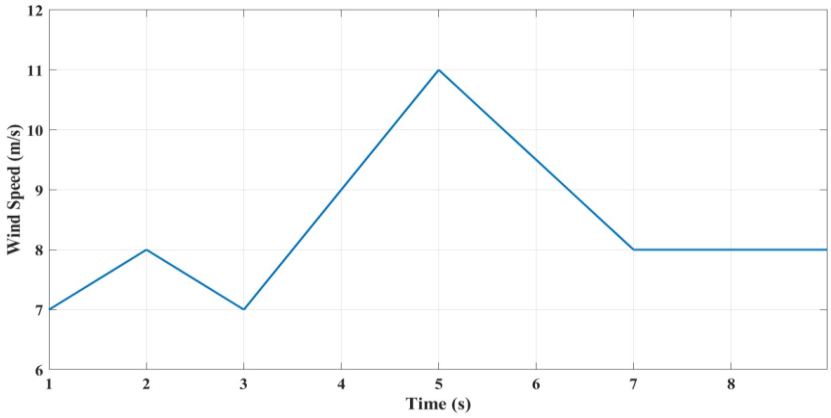

Figure 5-30 Wind speed

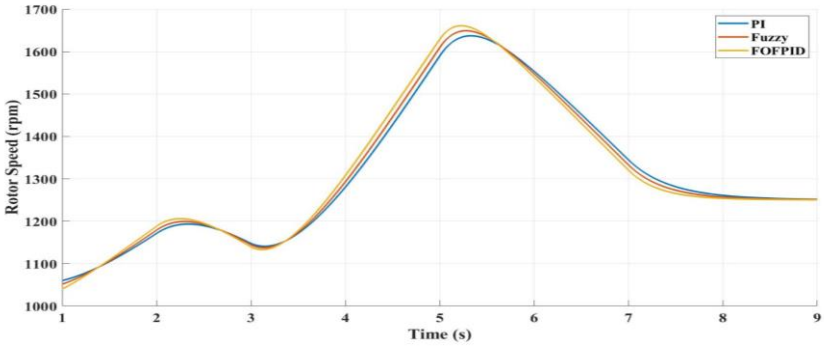

Figure 5-31 rotor speed

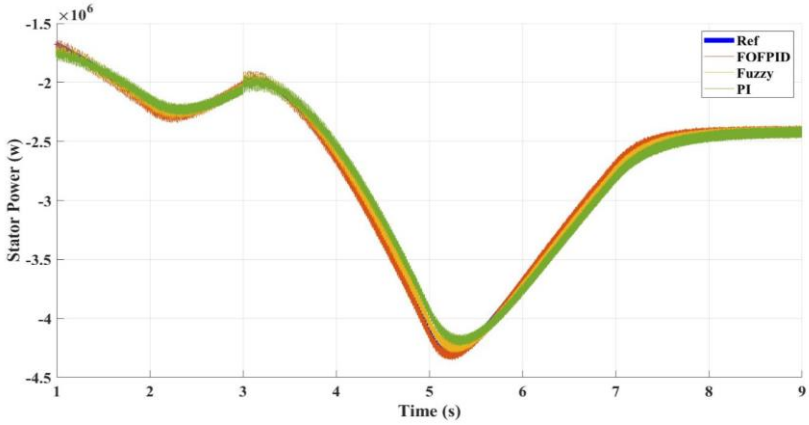

Figure 5-32 Stator active power

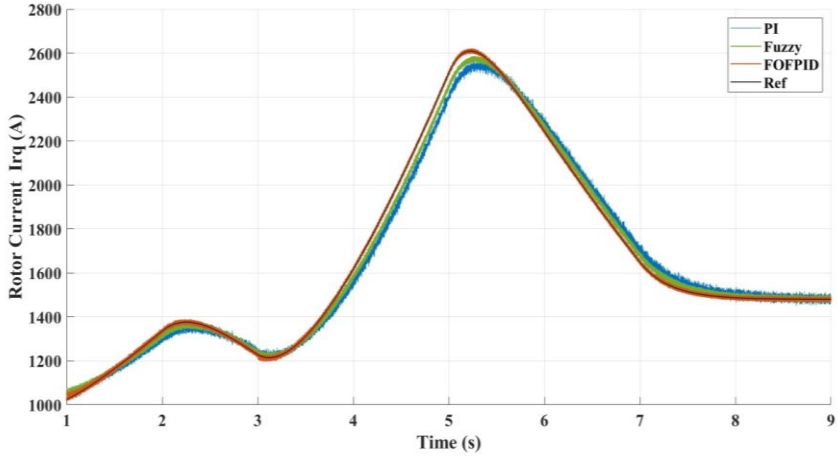

Figure 5-33 rotor currents Iqr

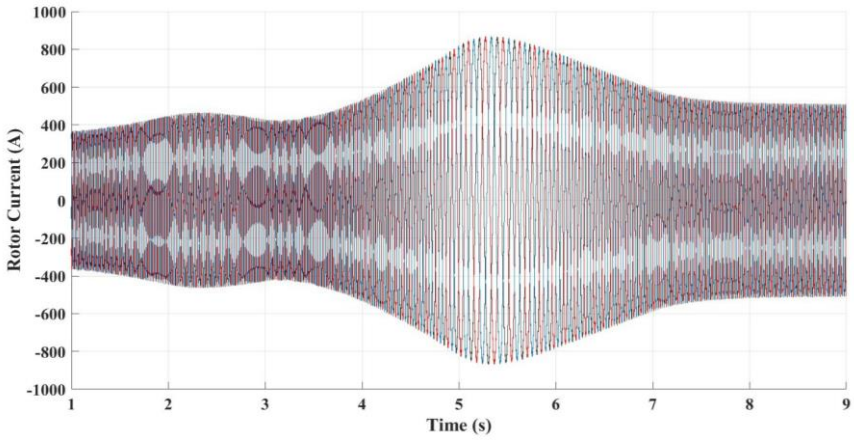

Figure 5-34 rotor current

5.8.4 Scenario 4

In this scenario deliberate modifications are made to the parameters of the DFIG system to assess the robustness of the optimized FO Fuzzy PD+I regulator and to compare its performance with that of the optimized PI regulator and Fuzzy regulator. Specifically, between the time interval of 3 to 6 seconds, the stator resistance of the DFIG is increased by 150% of its nominal value, while the system operates at a constant wind velocity of 8 m/s.

Figure 5-35 illustrates that the proposed regulator exhibits greater robustness compared to the optimized PI regulator and Fuzzy regulator, as evidenced by the

significant reduction in stator active power ripples with the optimized FO Fuzzy PD+I regulator. The optimized FO Fuzzy PD+I regulator effectively mitigates active power ripples to a much higher extent than the optimized PI regulator and Fuzzy regulator, achieving reductions of 99.80%, 92.15%, and 95.68%, respectively.

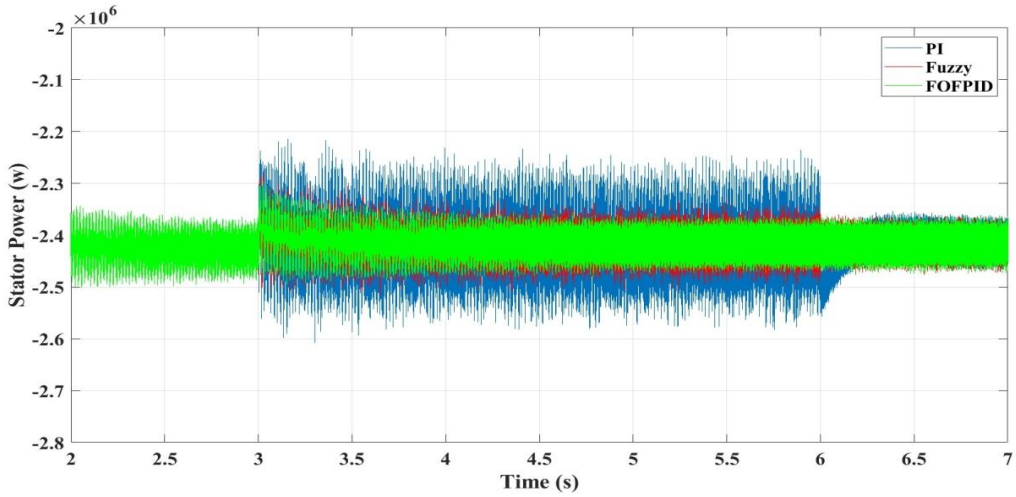

Figure 5-35 Stator active power

Furthermore, next Figures illustrates the total harmonic distortion (THD) of the current using the optimized FO Fuzzy PD+I regulator (Figure 5-36), the optimized PI regulator (Figure 5-37), and the Fuzzy regulator (Figure 5-38) when the DFIG parameters are altered. The optimized FO Fuzzy PD+I regulator achieves a THD of 1.23%, outperforming the Fuzzy regulator's THD of 1.38%. In contrast, the optimized PI regulator yields a THD of 4.72%. These results underscore the effectiveness of the optimized FO Fuzzy PD+I regulator in improving current THD, with a notable enhancement percentage of 26.05%.

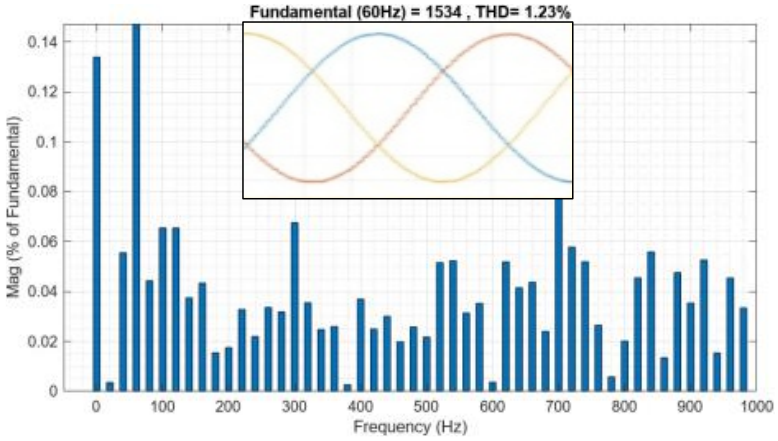

Figure 5-36 THD of the current using the FO Fuzzy PD+I regulator

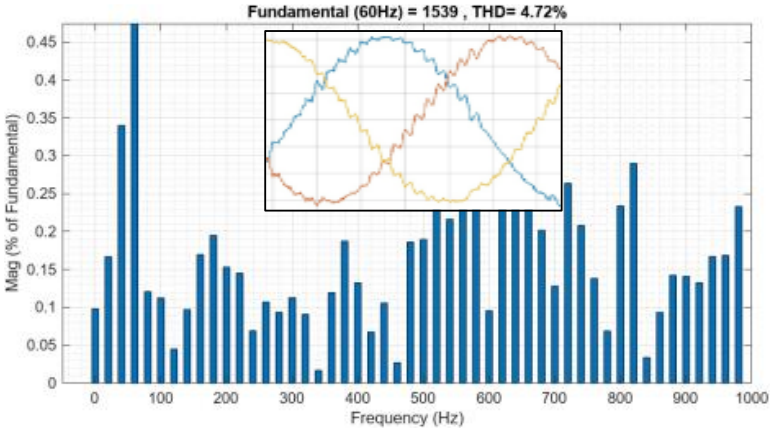

Figure 5-37 THD of the current using the PI regulator

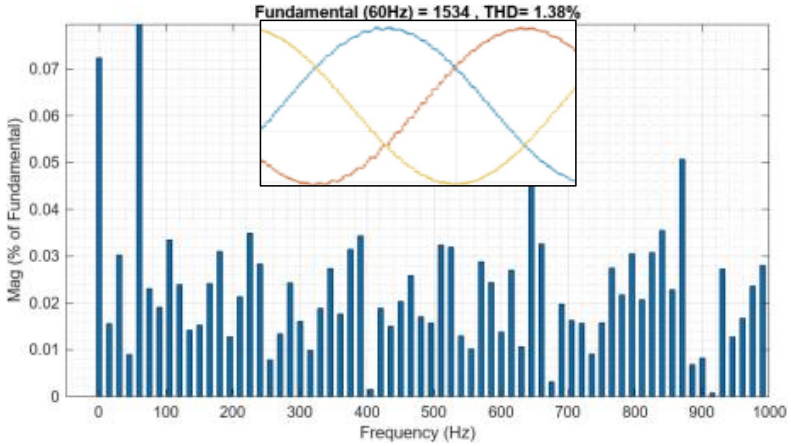

Figure 5-38 THD of the current using the Fuzzy regulator

5.9 Conclusions

To enhance the responsiveness of linked DFIGs within Wind Turbine Systems (WTSs), this chapiter introduces a novel approach for designing and tuning a fuzzy proportional-derivative with integral (PD+I) regulator. Employing the Social Spider Optimisation (SSO) method, a cutting-edge metaheuristic optimization tool, the optimal controller gains for the proposed Fractional Order (FO) Fuzzy PD+I regulator are determined. Furthermore, the resilience of the optimized FO Fuzzy PD+I regulator is evaluated under various sources of uncertainty, including significant changes in stator resistance, disturbances in stator active power, and fluctuations in wind velocity.

Simulation results across diverse scenarios consistently demonstrate the superior performance of the optimized FO Fuzzy PD+I regulator over both the optimized Proportional-Integral (PI) regulator and the Fuzzy regulator. Specifically, it exhibits enhanced stator current responses and effectively mitigates power variances. Moreover, application of the optimized FO Fuzzy PD+I regulator leads to a reduction in total harmonic distortion (THD) in the stator current, thereby enhancing the overall grid power quality. Importantly, the proposed FO Fuzzy PD+I regulator exhibits promise for application in nonlinear systems, indicating a crucial avenue for future research.

6. General Conclusion

Today, a significant portion of installed variable-speed wind turbines are equipped with doubly fed induction generators (DFIGs), enhancing the utilization of wind resources across various wind conditions. The Maximum Power Point Tracking (MPPT) control strategy is widely adopted to manage these wind systems, aiming to extract maximum wind power by optimizing the power coefficient.

After determining the optimal power coefficient, we applied vector control with stator flux orientation to the DFIG, modeled in steady-state conditions. We regulated the DC bus current by adjusting the values of active and reactive stator powers via Pulse Width Modulation (PWM) control, while overseeing DC current control to maintain a stable bus voltage on one hand, and to inject reactive power and compensate for network imbalances on the other hand. Simulation results validate the effectiveness of this approach in controlling the two cascaded converters.

Starting from the machine equations, we derived transfer functions linking currents and controlled variables, and determined Proportional-Integral (PI) controller parameters to strike a balance between responsiveness and stability.

Secondly, considering their advantages, we replaced the PI regulators with the FO Fuzzy PD+I regulator. This approach signifies a substantial advancement in DFIG control compared to current methods. Simulation results across various scenarios consistently showcase the superior performance of the optimized FO Fuzzy PD+I regulator over both the optimized Proportional-Integral (PI) regulator and the Fuzzy regulator.

Transitioning from simulation to practical implementation involves conducting trials in a laboratory or on a small-scale DFIG-based wind turbine system to validate the regulator's real-world applicability and performance.

We recommend collaborating with partners in the wind energy sector to facilitate field tests on larger-scale wind turbine systems. This collaboration enables assessment under diverse operating conditions and identification of unique challenges in realistic deployments.

Exploration of advanced optimization strategies, such as reinforcement learning, evolutionary algorithms, or hybrid optimization techniques, is advised to dynamically adjust the regulator's gains in response to evolving operating conditions.

7. References

1. Ackermann, T. (Ed.). (2012). Wind power in power systems. John Wiley & Sons.
2. Global Wind Energy Council (GWEC). (2023). Global Wind Report 2023.
3. Hansen, A. D., & Michalke, G. (2007). Modelling and control of variable-speed wind turbines. Wind Energy, 10(5), 451-471.
4. Peña, R., Clare, J. C., & Asher, G. M. (1996). Doubly fed induction generator using back-to-back PWM converters and its application to variable-speed wind-energy generation. IEE Proceedings - Electric Power Applications, 143(3), 231-241.
5. Muller, S., Deicke, M., & De Doncker, R. W. (2002). Doubly fed induction generator systems for wind turbines. IEEE Industry applications magazine, 8(3), 26-33.
6. Li, H., Chen, Z., & Pedersen, J. K. (2007). Optimal power control strategy of maximizing wind energy tracking and conversion for VSCF doubly fed induction generator system. In 2006 CES/IEEE 5th International Power Electronics and Motion Control Conference (Vol. 3, pp. 1779–1784). IEEE.
7. Abad, G., López, J., Rodríguez, M. A., Marroyo, L., & Iwanski, G. (2011). Doubly fed induction machine: Modeling and control for wind energy generation. Wiley.
8. Munteanu, I., Bratcu, A. I., Cutululis, N. A., & Ceanga, E. (2008). Optimal control of wind energy systems: Towards a global approach. Springer.
9. Bianchi, F. D., De Battista, H., & Mantz, R. J. (2006). Wind turbine control systems: Principles, modelling and gain scheduling design. Springer.
10. Heier, S. (2014). Grid integration of wind energy: onshore and offshore conversion systems. John Wiley & Sons..
11. Grobler, J. J., & Van Wyk, J. D. (1992). Decoupled control of the active and reactive power in a doubly fed induction generator. IEEE Transactions on Power Electronics, 7(3), 512-519.

12. R. Datta, and V.T. Ranganathan, "Direct power control of grid-connected wound rotor induction machine without rotor position sensors," IEEE Transactions on Power Electronics, vol. 16, no. 3, pp.390–399, May 2001.
13. Abad, G. (Ed.). (2017). Power electronics and electric drives for traction applications (p. 630). New York, NY, USA: Wiley.
14. Mohan, N., Undeland, T. M., & Robbins, W. P. (2003). Power electronics: Converters, applications, and design. Wiley.
15. Kabziński, J. (Ed.). (2016). Advanced control of electrical drives and power electronic converters (Vol. 75). Springer.
16. Abu-Rub, H., Malinowski, M., & Al-Haddad, K. (Eds.). (2014). Power electronics for renewable energy systems, transportation, and industrial applications. John Wiley & Sons.
17. World Health Organization (WHO). (2018). Air pollution and child health: Prescribing clean air.
18. Gomez, L. A. G., Grilo, A. P., Salles, M. B. C., & Sguarezi Filho, A. J. (2020). Combined control of DFIG-based wind turbine and battery energy storage system for frequency response in microgrids. Energies, 13(4), 894.
19. Manwell, J. F., McGowan, J. G., & Rogers, A. L. (2010). Wind energy explained: Theory, design and application (2nd ed., pp. 189–191). John Wiley & Sons.
20. Gaillard, A. (2010). Système éolien basé sur une MADA: Contribution à l'étude de la qualité de l'énergie électrique et de la continuité de service (Doctoral dissertation). Université Henri Poincaré - Nancy 1.
21. Chhipa, A. A., Chakrabarti, P., Bolshev, V., Chakrabarti, T., Samarin, G., & et al. (2022). Modeling and control strategy of wind energy conversion system with grid-connected doubly-fed induction generator. Energies, 15(18), 6694.
22. Berhail, A. (2020). Commande d'une éolienne à base de GSAP connectée au réseau électrique par convertisseur multiniveaux (Master's thesis). Université du Québec à Trois-Rivières.

23. Liserre, M., Cárdenas, R., Molinas, M., & Rodríguez, J. (2011). Overview of multi-MW wind turbines and wind parks. IEEE Transactions on Industrial Electronics, 58(4), 1081–1095.

24. Radia, R. (2009). Étude d'une chaîne de conversion d'énergie éolienne (Master's thesis). Université de Constantine, Algérie.

25. Aldwaihi, H. A. (2013). Commande non linéaire fondée sur la platitude d'un système de production éolien (Doctoral dissertation). Université de Bretagne occidentale - Brest.

26. Cardenas, R., Pena, R., Alepuz, S., & Asher, G. (2013). Overview of control systems for the operation of DFIGs in wind energy applications. IEEE Transactions on Industrial Electronics, 60(7), 2776–2798.

27. Stiebler, M. (2008). Wind energy systems for electric power generation. Springer.

28. Vas, P. (1990). Vector control of AC machines. Clarendon Press.

29. Santisteban, J. A., & Stephan, R. M. (2001). Vector control methods for induction machines: An overview. IEEE Transactions on Education, 44(2), 170–175.

30. Xu, L., & Cartwright, P. (2006). Direct active and reactive power control of DFIG for wind energy generation. IEEE Transactions on Energy Conversion, 21(3), 750–758.

31. Pettersson, A., Harnefors, L., & Thiringer, T. (2004, June). Comparison between stator-flux and grid-flux-oriented rotor current control of doubly-fed induction generators. In Proceedings of the 35th Power Electronics Specialist Conference (Vol. 1, pp. 482–486). IEEE.

32. Arnalte, S., Burgos, J. C., & Rodríguez-Amenedo, J. L. (2002). Direct torque control of a doubly-fed induction generator for variable speed wind turbines. Electric Power Components and Systems, 30(2), 199–216.

33. Gokhale, K. P. (1999). Controller for a wound rotor induction machine (U.S. Patent No. 5,905,382). U.S. Patent and Trademark Office.

34. Bose, B. K. (2002). Modern power electronics and AC drives (pp. 535–557). Prentice Hall PTR.

35. Bose, B. K. (1994). Expert system, fuzzy logic, and neural network applications in power electronics and motion control. Proceedings of the IEEE, 82(8), 1303–1323.

36. Simoes, M. G., Bose, B. K., & Spiegel, R. J. (1997). Design and performance evaluation of a fuzzy logic-based variable-speed wind generation system. IEEE Transactions on Industry Applications, 33(4), 956–965.

37. Wang, J., & Hyun, S. H. (2011). ANN based pitch angle controller for variable speed variable pitch wind turbine generation system. In 2011 6th International Forum on Strategic Technology (IFOST) (Vol. 1, pp. 443–447).

38. Akagi, H., & Sato, H. (2002). Control and performance of a doubly-fed induction machine intended for a flywheel energy storage system. IEEE Transactions on Power Electronics, 17(1), 109–116.

39. Takahashi, I., & Noguchi, T. (1986). A new quick-response and high-efficiency control strategy of an induction motor. IEEE Transactions on Industry Applications, 22(5), 820–827.

40. Depenbrock, M. (1988). Direct self-control (DSC) of inverter-fed induction motors. IEEE Transactions on Power Electronics, 3(4), 420–429.

41. Malinowski, M., Kazmierkowski, M. P., Hansen, S., Blaabjerg, F., & Marques, G. D. (2001). Virtual-flux-based direct power control of three-phase PWM rectifiers. IEEE Transactions on Industry Applications, 37(4), 1019–1027.

42. Malinowski, M., Jasinski, M., & Kazmierkowski, M. P. (2004). Simple direct power control of three-phase PWM rectifier using space-vector modulation (DPC-SVM). IEEE Transactions on Industrial Electronics, 51(2), 447–454.

43. Kazemi, M. V., Yazdankhah, A. S., & Kojabadi, H. M. (2010). Direct power control of DFIG based on discrete space vector modulation. Renewable Energy, 35(5), 1033–1042.

44. Zhi, D., Xu, L., & Williams, B. W. (2010). Model-based predictive direct power control of doubly fed induction generators. IEEE Transactions on Power Electronics, 25(2), 341–351.

45. Mutschler, P., & Hoffmann, R. (2002, June). Comparison of wind turbines regarding their energy generation. In Proceedings of the 33rd Annual IEEE Power Electronics Specialists Conference (Vol. 1, pp. 6–11). IEEE.

46. Pichan, M., Rastegar, H., & Monfared, M. (2013). Two fuzzy-based direct power control strategies for doubly-fed induction generators in wind energy conversion systems. International Journal of Energy, 51, 154–162.

47. Sam, M. (2016). Direct power control of a doubly fed induction generator in wind power systems (Master's thesis). University of Akron.

48. Ragheb, M., & Ragheb, A. M. (2011). Wind turbines theory—The Betz equation and optimal rotor tip speed ratio. In M. Carrasco & J. H. Nouri (Eds.), Fundamental and advanced topics in wind power (pp. 19–38). InTech.

49. Zaragoza, J., Pou, J., Arias, A., Spiteri, C., Robles, E., & Ceballos, S. (2011). Study and experimental verification of control tuning strategies in a variable speed wind energy conversion system. Renewable Energy, 36(5), 1421–1430.

50. Datta, R., & Ranganathan, V. T. (2003). A method of tracking the peak power points for a variable speed wind energy conversion system. IEEE Transactions on Energy Conversion, 18(2), 163–168.

51. Rajendran, S., & Jena, D. (2014). Control of variable speed variable pitch wind turbine at above and below rated wind speed. Journal of Wind Energy, 2014, 1–14.

52. Arnaltes, S., Rodríguez-Amenedo, J. L., & Montilla-DJesus, M. E. (2018). Control of variable speed wind turbines with doubly fed asynchronous generators for standalone applications. Energies, 11(1), 97.

53. Neammanee, B., Sirisumrannukul, S., & Chatratana, S. (2010). Control strategies for variable-speed fixed-pitch wind turbines. In G. M. Mujtaba & M. R. Mohammadi (Eds.), Wind power (pp. 209–232). InTech.

54. Chen, J., Wang, C., & Song, Y. (2014, December). Power control strategy for variable speed fixed-pitch wind turbines. In Proceedings of the 2014 13th

International Conference on Control, Automation, Robotics & Vision (ICARCV) (pp. 559–564). IEEE.

55. Kumar, D., & Chatterjee, K. (2016). A review of conventional and advanced MPPT algorithms for wind energy systems. Renewable and Sustainable Energy Reviews, 55, 957–970.

56. Nasiri, M., Milimonfared, J., & Fathi, S. H. (2014). Modeling, analysis, and comparison of TSR and OTC methods for MPPT and power smoothing in permanent magnet synchronous generator-based wind turbines. Energy Conversion and Management, 86, 892–900.

57. Thongam, J. S., Bouchard, P., Beguenane, R., Okou, A. F., & Merabet, A. (2011, November). Control of variable speed wind energy conversion system using a wind speed sensorless optimum speed MPPT control method. In Proceedings of the 2011 37th Annual Conference of the IEEE Industrial Electronics Society (IECON) (pp. 855–860). IEEE.

58. Sompracha, C. (2019). Optimal control of wind energy conversion systems with doubly-fed induction generators (Doctoral dissertation). University of Birmingham.

59. Hopfensperger, B., Atkinson, D. J., & Lakin, R. A. (2000). Stator-flux-oriented control of a doubly-fed induction machine with and without position encoder. IEE Proceedings - Electric Power Applications, 147(4), 241–250.

60. Lei, L. (2014). Doubly-fed induction generator wind turbine modelling, control, and reliability (Doctoral dissertation). The University of Manchester.

61. Phillips, C. L., & Harbor, R. D. (2000). Feedback control systems (4th ed.). Prentice Hall.

62. Bourdoulis, M. K., & Alexandridis, A. T. (2013). Rotor-side cascaded PI controller design and gain tuning for DFIG wind turbines. In Proceedings of the 4th International Conference on Power Engineering, Energy and Electrical Drives (pp. 733–738).

63. Zadeh, L. A. (1965). Fuzzy sets. Information and Control, 8(3), 338–353.

64. Zadeh, L. A. (1983). The role of fuzzy logic in the management of uncertainty in expert systems. Fuzzy Sets and Systems, 11, 197–198.

65. Martaj, N., & Mokhtari, M. (2010). Contrôle par logique floue. In MATLAB R2009, SIMULINK et STATEFLOW pour Ingénieurs, Chercheurs et Etudiants (pp. 747–805). Springer.

66. Chen, G.-P., Malik, O., Hope, G., Qin, Y.-H., & Xu, G.-Y. (1993). An adaptive stabilizer based on the self-optimizing pole shifting control strategy. IEEE Transactions on Energy Conversion, 8(4), 639–645.

67. El-Metwally, K. A., & Malik, O. P. (1995). Fuzzy logic power system stabiliser. IEE Proceedings - Generation, Transmission and Distribution, 142(3), 277–281.

68. Belmokhtar, K. (2015). Contribution à l'intégration d'un parc éolien à un réseau électrique autonome, avec stockage d'énergie sous forme d'hydrogène (Doctoral dissertation). Université du Québec à Trois-Rivières.

69. Baghli, L. (1999). Contribution à la commande de la machine asynchrone, utilisation de la logique floue, des réseaux de neurones et des algorithmes génétiques (Doctoral dissertation). Université Henri Poincaré-Nancy I.

70. Chaoui, H. (2013). Commande adaptive de systèmes à dynamique complexe basée sur l'intelligence artificielle. Library and Archives Canada.

71. Hamouda, N., Babes, B., Hamouda, C., Kahla, S., Ellinger, T., & Alami, H. (2020). Optimal tuning of fractional order proportional-integral-derivative controller for wire feeder system using ant colony optimization. Journal Européen des Systèmes Automatisés, 53, 157–166.

72. Afghoul, H., Chikouche, D., Krim, F., Babes, B., & Beddar, A. (2016). Implementation of fractional-order integral-plus-proportional controller to enhance the power quality of an electrical grid. Electric Power Components and Systems, 44(11), 1018–1028.

73. Monje, C., Chen, Y., Vinagre, B., Xue, D., & Feliu, V. (2010). Fractional-order systems and controls. Springer-Verlag London.

74. Paducel, I., Safirescu, C. O., & Dulf, E.-H. (2022). Fractional order controller design for wind turbines. Applied Sciences, 12(16), 8400.

75. Pan, I., & Das, S. (2013). Intelligent fractional order systems and control. Springer.

76. Pan, I., & Das, S. (2016). Fractional order fuzzy control of hybrid power system with renewable generation using chaotic PSO. ISA Transactions, 62, 19–29.

77. Kumar, V., Rana, K. P. S., Kumar, J., Mishra, P., & Nair, S. S. (2016). A robust fractional order fuzzy P + fuzzy I + fuzzy D controller for nonlinear and uncertain system. International Journal of Automation and Computing, 14(4), 474–488.

78. Pan, I., Das, S., & Gupta, A. (2011). Tuning of an optimal fuzzy PID controller with stochastic algorithms for networked control systems with random time delay. ISA Transactions, 50(1), 28–36.

79. Li, W., Chang, X., Farrell, J., & Wahl, F. M. (2001). Design of an enhanced hybrid fuzzy P+ID controller for a mechanical manipulator. IEEE Transactions on Systems, Man, and Cybernetics, Part B: Cybernetics, 31(6), 938–945.

80. Er, M. J., & Sun, Y. L. (2001). Hybrid fuzzy proportional-integral plus conventional derivative control of linear and nonlinear systems. IEEE Transactions on Industrial Electronics, 48(6), 1109–1117.

81. Malki, H. A., Misir, D., Feigenspan, D., & Chen, G. (1997). Fuzzy PID control of a flexible-joint robot arm with uncertainties from time-varying loads. IEEE Transactions on Control Systems Technology, 5(3), 371–378.

82. Åström, K., & Hägglund, T. (1995). PID controllers: Theory, design, and tuning (Vol. 2). Instrument Society of America.

83. Argo, B., & Mulyadi, S. (2015). Optimization of PID controller parameters on flow rate control system using multiple effect evaporator particle swarm optimization. International Journal on Advanced Science, Engineering and Information Technology, 5(2), 62–69.

84. Zhuang, M., & Atherton, D. P. (1991). Tuning PID controllers with integral performance criteria. In Proceedings of the International Conference on Control (Vol. 1, pp. 481–486).

85. Bergstra, J., & Bengio, Y. (2012). Random search for hyper-parameter optimization. Journal of Machine Learning Research, 13, 281–305.

86. Kramer, O. (2017). Genetic algorithm essentials (Vol. 679). Springer International Publishing.

87. Karaboga, D. (2005). An idea based on honey bee swarm for numerical optimization (Technical Report - TR06). Erciyes University.

88. Wang, G., Deb, S., & Coelho, L. d. S. (2015). Elephant herding optimization. In 2015 3rd International Symposium on Computational and Business Intelligence (ISCBI) (pp. 1–5).

89. Kiranyaz, S., Gabbouj, M., & Ince, T. (2014). Multidimensional particle swarm optimization for machine learning and pattern recognition. Springer.

90. Heinänen, E. E. (2018). A method for automatic tuning of PID controller following Luus-Jaakola optimization (Master's thesis).

91. Cuevas, E., Luque, A., Zaldívar, D., & Pérez-Cisneros, M. (2017). Evolutionary calibration of fractional fuzzy controllers. Applied Intelligence, 47(1), 291–303.

92. Ouadfel, S., & Taleb-Ahmed, A. (2016). Social spiders optimization and flower pollination algorithm for multilevel image thresholding: A performance study. Expert Systems with Applications, 55, 566–584.

93. Laddha, A., Hazra, A., & Basu, M. (2015). Optimal operation of distributed renewable energy resources based micro-grid by using social spider optimization. In Proceedings of the IEEE Power, Communication and Information Technology Conference (PCITC) (pp. 756–761).

94. Hejrati, Z., Fattahi, S., & Faraji, I. (2014). Optimal congestion management using the social spider optimization algorithm. In Proceedings of the 29th International Power System Conference.

95. Vijay, D., & Priya, V. (2017). Anti-islanding protection of distributed generation based on social spider optimization technique. International Journal of Advanced Engineering Research and Science, 4(1), 32–40.

96. Dembri, R., Rahmani, L., Babes, B., Azizi, I. (2024). Enhanced control of doubly fed induction generator based wind turbine system using fractional-order fuzzy PD+I regulator. Journal Européen des Systèmes Automatisés, Vol. 57, No. 1, pp. 211-223.

ملخص

تستهدف هذه الأطروحة تحسين التحكم في مولدات التحريض مزدوجة التغذية (DFIG) المستخدمة في توربينات الرياح ذات السرعة المتغيرة، والتي تعتبر أساسية لزيادة استخراج الطاقة في ظروف الرياح المتغيرة. تقترح الأطروحة منظمًا فوضويًا PD+I من الدرجة الكسرية (FO Fuzzy PD+I) يتم تحسينه باستخدام خوارزمية المُحسِّن العنكبوت الاجتماعيSSO ، مما يمثل تقدمًا كبيرًا مقارنةً بالمنظمات التقليدية من نوع .PI يجمع هذا المنظم بين المنطق الضبابي والتحكم من الدرجة الكسرية، مما يحسن من قوة الأداء والموثوقية في التحكم في تيار الـDFIG ، مع إدارة فعالة للاختلافات في المعلمات والتغيرات في سرعة الرياح.من خلال المحاكاة عبر سيناريوهات تشغيلية متنوعة، يتفوق المنظم المقترح باستمرار على المنظم التقليدي PI من حيث مقاييس الأداء الأساسية مثل الخطأ المطلق الزمني التكاملي (ITAE)، والارتفاع الأقصى، ووقت الاستقرار، والتشويه التوافقي الكلي .(THD) تشكل هذه البحث مساهمة مهمة في مجال التحكم في الـDFIG ، حيث تقدم حلاً أكثر فعالية لتشغيل توربينات الرياح، مما يحسن جودة الطاقة وقدرات التكامل مع الشبكة.

.الكلمات المفتاحية: مولد حثي ذو تغذية مزدوجة ؛ نظام توربينات الرياح ؛ منظم ضبابي تكاملي تفاضلي جزئي من الدرجة الكسرية. التحكم المباشر بالمتجهات ؛ تقنية محسن العنكبوت الاجتماعي . محول ثنائي الاتجاه.

Résumé

Cette thèse vise à améliorer le contrôle des générateurs à double alimentation (DFIG) utilisés dans les éoliennes à vitesse variable, essentiels pour maximiser l'extraction d'énergie dans des conditions de vent variées. Elle propose un régulateur flou PD+I à ordre fractionnaire (FO Fuzzy PD+I), optimisé avec l'algorithme Social Spider Optimizer, représentant une avancée significative par rapport aux régulateurs PI traditionnels. Le régulateur FO Fuzzy PD+I combine la logique floue avec le contrôle à ordre fractionnaire, améliorant la robustesse et la performance du contrôle du courant DFIG tout en gérant efficacement les incertitudes des paramètres et des variations de vitesse du vent. À travers des simulations dans divers scénarios opérationnels, le régulateur proposé surpasse systématiquement le régulateur PI traditionnel en termes de métriques de performance clés telles que l'erreur absolue du temps intégral (ITAE), le pic de dépassement, le temps de stabilisation et la distorsion harmonique totale (THD). Cette recherche constitue une contribution significative au contrôle des DFIG, offrant une solution plus efficace pour le fonctionnement des éoliennes et améliorant la qualité de l'énergie ainsi que les capacités d'intégration au réseau.

Mots Clés : générateur asynchrone à double alimentation ; système d'éolienne ; régulateur flou fractionnaire PD+I ; contrôle vectoriel direct ; technique d'optimisation sociale de l'araignée (SSO) ; convertisseur bidirectionnel.

.

Abstract

This thesis aims to enhance the control of Doubly Fed Induction Generators (DFIG) used in variable-speed wind turbines, which are vital for maximizing energy extraction in varying wind conditions. It introduces a fractional-order fuzzy PD+I (FO Fuzzy PD+I) regulator, optimized with the social spider optimizer algorithm, representing a significant advancement over traditional PI regulators. The FO Fuzzy PD+I regulator combines fuzzy logic with fractional-order control, improving robustness and performance in controlling DFIG current while effectively managing uncertainties in parameters and wind speed variations. Through simulations across various operational scenarios, the proposed regulator consistently outperforms the traditional PI regulator in key performance metrics such as integral time absolute error (ITAE), peak overshoot, settling time, and total harmonic distortion (THD). This research makes a significant contribution to DFIG control, providing a more effective solution for wind turbine operation and enhancing power quality and grid integration capabilities.

. **Key words**: doubly-fed induction generator (DFIG); wind turbine system (WTS); fractional-order fuzzy PD+I (FO Fuzzy PD+I) regulator; direct vector control (DVC); social spider optimization (SSO) technique. bidirectional converter.